UCLouvain

AGRO LOUVAIN

Faculty of Bioscience Engineering

Characterisation of the radiative response of crops covered with tephra

Authors: de Potter d'Indoye Ombeline & van Wassenhove Sébastien

Supervisors: Pierre Delmelle & Noa Ligot

Readers: François Jonard & Xavier Draye

Academic year 2022-2023

Master thesis presented to obtain the diploma of bioengineer: technologies and environmental sciences

Acknowledgments

We would like to take this opportunity to express our sincere gratitude and appreciation to the following people for their invaluable support, advice, and contributions throughout the completion of this master's thesis:

First, we are deeply grateful to our supervisor, Pierre Delmelle, for his unwavering support and for giving us the opportunity to participate in a unique experiment. His expertise, advice and encouragement were crucial to the direction and success of this research. We are truly grateful for his mentorship and the knowledge he passed on to us.

We would also like to express our deep gratitude to our co-supervisor, Noa Ligot, who supported us throughout this project. Her constant availability, advice and valuable feedback played a crucial role in the completion of this thesis. It would not have been possible without her unwavering support and dedication.

We are indebted to Yanfei Li, who accompanied us on every weekend to perform the drone flights. Her willingness to give up her free time and her enthusiasm to help us were truly remarkable. We are grateful for her contributions and support throughout the experience.

Special thanks go to Hugues Falys and the staff of the Marbaix farm for managing the agronomic aspects of the experiment. We would like to express our gratitude to Sébastien François and Axel Willems for their help in building reliable systems for the experiment. Their knowledge and expertise contributed significantly to the overall success of this research. Thank you to Professor Kristof Van Oost for generously allowing us to use his drone for the experiment. His trust was instrumental in facilitating the data collection process.

Finally, we would like to thank Professor Xavier Draye and François Jonard for agreeing to be members of the jury for this thesis.

In conclusion, we are deeply grateful to all these people for their unfailing support, advice, and contributions. Their expertise, encouragement and dedication played an essential role in the completion of this thesis.

Table of contents

List of figures

List of tables

1 Introduction

Around 800 million people live within 100 km of an active volcano (Loughlin et al., 2015). A such proximity exposes local populations and human activities to hazards of the volcano. Volcanic soils present specific physical and chemical characteristics, making them particularly suitable for agriculture (Dahlgren et al., 2004). In active volcanic regions, local populations rely mainly on agronomical revenues for their subsidence (Wilson et al., 2011). However, agriculture is one of economic sectors most impacted by volcanic eruptions (FAO, 2021). The most frequent hazard corresponds to tephra, which can be transported and dispersed over several thousands of kilometres (Bonadonna et al., 2005). The effects of such deposits on vegetation are modulated by various volcanic and non-volcanic factors. A few studies have revealed that crops are sensitive to specific volcanic factors, including grain size, mass load, surface composition, etc. (Craig et al., 2021; Ligot et al., 2022), but also to non-volcanic factors such as plant traits, phenological stage, environmental settings, etc. (Craig et al., 2016; Cutler et al., 2021; Del Bello et al., 2021).

The vulnerability of crops to tephra is a key element in assessing the volcanic risk to agriculture. It is usually represented as fragility functions, which are modelling tools that quantitatively link crop yield losses to the intensity of tephra mass load (Craig et al., 2021). However, these data are very scarce and obtaining field measurements is an arduous task, given the dangerous environment that prevails after a volcanic eruption (James et al., 2020). As an alternative, remote sensing may allow collection of impact data on vegetation in volcanic regions affected by tephra (Battude et al., 2016; Dong et al., 2003). The advantage of using remote sensing instead of other methods is that it provides cost effective, rapid and regular data across time and space from dangerous places (James et al., 2020).

The characterization of tephra-affected vegetation using remote sensing after a volcanic eruption has never been performed. The use of vegetation indices to quantify damage on crops from tephra could provide valuable information on crop vulnerability and contribute to the construction of fragility functions. In turn, this would improve risk analysis.

The objective of this study is to characterize the spectral response of tephra deposit on crops. To do so, the study first focuses on the spectral properties of three tephra samples in the visible, near infrared and short-wave infrared spectrum. Then, the spectral response of wheat covered with tephra is determined using a multispectral camera attached to a drone.

2 State of the art

2.1 Volcanoes and agriculture

2.1.1 Colocation of volcanoes and agriculture

Over the last 10,000 years, approximately 1,550 volcanoes have erupted in the world (Cottrell, 2015). Volcanic activity is mostly caused by the movement of tectonic plates, they either move apart, creating earth's crust and rift volcanoes such as in Iceland or East-Africa. Otherwise, the plates collide, causing the oceanic plate, the denser one, to move under the continental plate, less dense, resulting in the formation of subduction zone such as the Lesser Antilles in the Caribbean and the South Sandwich Islands in the Southern Atlantic (Loughlin et al., 2015). Thus, most volcanoes are located on the borders of tectonic plates (Figure 1) (Cottrell, 2015; Luhr, 1992). Some volcanoes also erupt from hot spots, which are weak zones in the lithosphere where magma is continuously produced and can punched directly through the crust. Good examples include the Yellowstone Caldera and the Hawaiian volcanoes in the USA.

The erupted material is generally basalt, andesite, dacite and rhyolite, depending on the origin of the magma and its evolution while stored within the crust. Volcanic eruptions can be grouped into two broad classes: effusive or explosive eruption. Effusive eruptions usually occur at volcanoes powered by basaltic magmas generated in divergent plate areas. The effusiveness relates to the low viscosity and gas content of such magmas, which have a low silica content (≤57 weight %). Explosive eruptions occur mainly along subduction zones, where an oceanic plate plunges under a continental plate. The silica content of magmas generated by this process is typically higher compared to basaltic magmas. As a result, silica-rich magmas are also more viscous and contain a larger proportion of dissolved gases (Decker & Decker, 2023). Depending on the eruption type, the damage caused to ecosystems, human infrastructures, and human activities varies.

The link between the distribution of volcanoes and humans is undeniable because their explosive behaviour creates fertile lands on which populations can settle (Cottrell, 2015). Volcanic activity also produces other positive impacts on society, such as generating geothermal energy, accumulating carbon in the soil and providing nutrients to plants (Cottrell, 2015; Fiantis et al., 2019). However, volcanoes also trigger various hazards that can severely impact to surrounding ecosystems and populations. For example, on 18 May 1980, Mount St. Helens entered in eruption, causing 57 human deaths as well as destroying properties and infrastructures (Cook et al., 1981). From 1500 AD to 2017, approximately 260,000 people perished during volcano hazards (Brown et al., 2017). Entire cities have been destroyed in the past due to several deleterious effects of volcanic activity: global cooling of Earth’s climate, devastating mass flows (pyroclastic flows, debris flows and avalanches), and heavy ash deposition across large distances of up to several hundreds of kilometres (Schmincke, 2004).

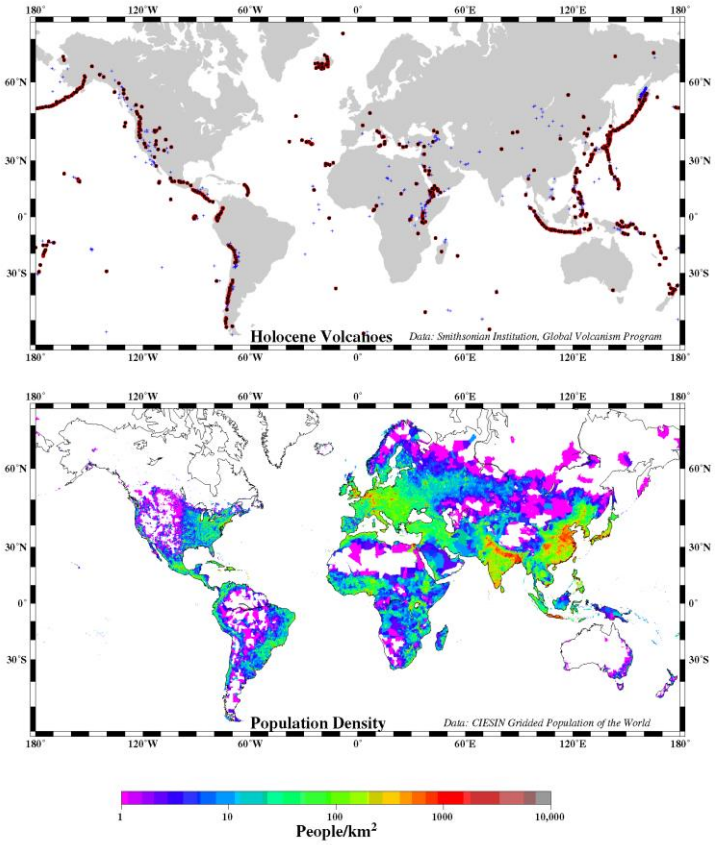

Figure 1: The global distribution of Holocene volcanoes and human population. Historically active volcanoes are shown as circles and Holocene volcanoes without historical eruptions are shown as crosses. Population density, derived from 127,105 census estimates, is shown on a logarithmic scale. Source: Small & Naumann, 2001.

Even though volcanic eruptions are one of the most dangerous natural phenomena, more than 800 million people live within 100 kilometres of an active volcano (Loughlin et al., 2015), and this number keeps increasing along with global population growth (Small & Naumann, 2001). The increase in the worldwide population induces a significant pressure on the agrarian system (Godfray et al., 2010). During explosive eruptions, volcanic fragments and debris are ejected, resulting in the deposition of volcanic ash that can be incorporated into the soil, eventually acting as a natural fertiliser (Shoji et al., 1993). The physical and chemical characteristics of volcanic soils make them particularly suitable for agriculture, which is often the main source of livelihood in active volcanic regions (Wilson et al., 2011). Even though these soils represent only 1% of the earth's surface, they feed at least 10% of the world's population (Ping, 2000).

2.1.2 Volcanic soils and fertility

Volcanic soils are soils formed on volcanic ejecta (ash, cinder or pumice), most of them are referred as Andosols (Mcdaniel et al., 2012; USDA, 1999). Like any other soils, Andosols are built up through a classical "topdown" mechanism where the parent material is eroded to form soil horizons. In addition to that, Andosols are also shaped via an "upbuilding

pedogenesis", consisting in the deposit of young volcanic material on top of older ones (Mcdaniel et al., 2012; Figure 2).

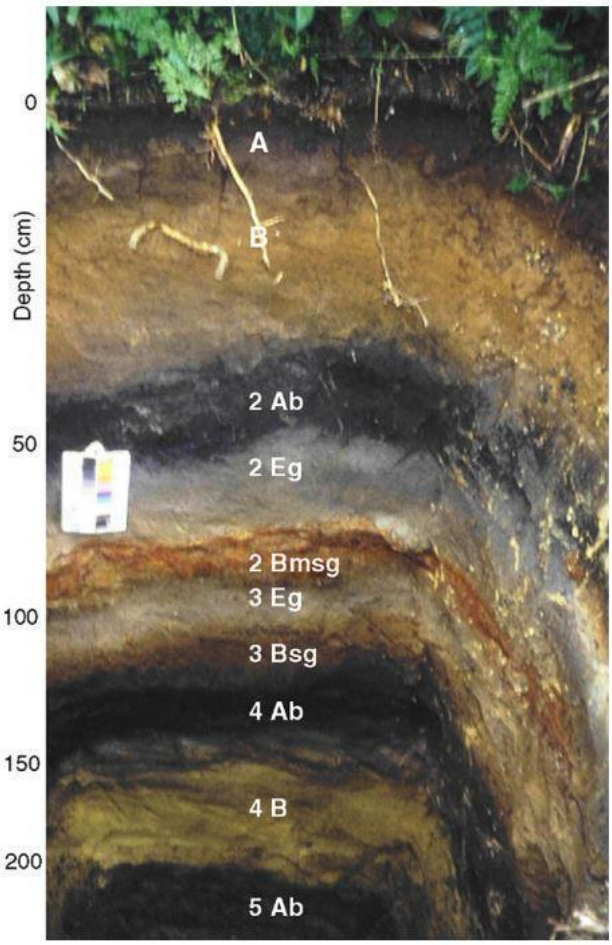

Figure 2: Photo of a soil profile, i.e., composed of various successive soils buried by volcanic deposits, on the slope (2250 m.a s. l.) of Mt. Kilimanjaro, Tanzania, showing a topsoil (A and B) and four buried paleosoils. The parent material (2 Eg) of the first buried soil (2 Ab) is indicated. Source: Zech, 2006.

Volcanic ejecta are normally rapidly weathered to form noncrystalline nanomaterials which are essential to obtain the unique properties of Andosols, referred as andic properties (FAO, 2023; Shoji et al., 1993). These compounds, including allophanes, imogolites, ferrihydrites, and aluminium (Al) and iron (Fe)-humus complexes, lead to a range of unique chemical and physical properties that account for the high fertility of volcanic soils (Mcdaniel et al., 2012). Some of the key andic properties are: good water and phosphorus retention, low bulk density, variable charge, high friability, stable soil aggregates and excellent tilth (Ping, 2000; Dahlgren et al., 2004). Andosols usually sustain a productive agriculture, which makes them attractive and a good place to settle in (Dahlgren et al., 2004).

2.2 Volcanoes present a threat to crops

2.2.1 Tephra

Tephra is defined as solid and fragmented magma material ejected into the air during explosive eruptions. It includes a wide range of chemical compositions, colours, and grain size classes, as discussed below (Manville et al., 2000). Tephra can be divided into different classes according to their size: ash (< 2 millimetres), lapilli or volcanic cinders (2 – 64 millimetres) and volcanic bombs or volcanic blocks (> 64 millimetres).

The formation of tephra has multiple origins. The main process involved in the formation of tephra is the fragmentation of magma (rocks in fusion) during an explosive eruption. This occurs when gas is contained in brittle or ductile melt. Other processes can lead to the formation of tephra, such as the erosion of old rocks in the volcanic conduit when magma rises through the surface, or simply by abrasion of larger fragments in the volcanic eruptive plume (Macedonio et al., 1994; Mcguire, 2003).

The composition of tephra depends primarily on the composition of the magma from which they derive (Ghiorso & Gualda, 2015). Magmas range from mafic to silicic compositions (Heiken, 1972). Basaltic magmas are poor in silica (≤57 weight % SiO_2) but enriched in Al, Fe and magnesium (Mg) compared to intermediate compositions such as those found for andesitic and dacitic (57–77 weight % SiO_2) magmas (Bas et al., 1986). Rhyolitic magmas are the silica-rich endmember with SiO_2 content > 70 weight % (Irvine & Baragar, 1971).

Two types of materials occur in tephra: amorphous and crystalline. Their formation depends on the magma cooling rate. Effusive eruptions are characterised by slow magma extrusion rate, typically leading to crystalline lava flows. Depending on the primarily magma composition, crystals like quartz, feldspars, plagioclases, pyroxenes, olivine, and Fe/titanium (Ti) oxides could be found (Heiken, 1972; Medeiros et al., 2021). In contrast, explosive eruptions have high magma extrusion rate and the numerous magma fragments released into the atmosphere are quenched rapidly. As a result, crystalline minerals have had almost no time to form, and the amorphous glass component tends to dominate the tephra composition. Phreatomagmatic eruption, which is a special type of eruption, result to a higher cooling rate, inducing the formation of smaller pyroclasts that are quickly quenched to create glass-rich deposits (Henderson et al., 2021).

Colour strongly affects the interaction of tephra with electromagnetic radiation. Depending on bulk composition, a tephra from silicic origin, richer in SiO_2 and poorer in Fe will develop a paler colour compared to a tephra from mafic rocks which tends to be darker (Figure 3; Scholze, 1991). Chemical alteration such as the oxidation of Fe oxides can also modify the colour of tephra (Samaniego et al., 2011). In addition, the presence of transition metals such as Fe or Ti on mineral phases and silicate glass leads to an increase of absorptive properties

(Burns, 1993). The reflectance of tephra also depends on its water content (Tian & Philpot, 2015).

Figure 3: Different extrusive volcanic rocks with various silica contents and colours: basalt (black), andesite (dark to light grey), dacite (usually light grey), and rhyolite (pale) rocks. Source: Rhea, 2022.

The grain size distribution present in a given tephra sample is another property affecting spectral and chemical properties. The fragmentation of silicic rock results in the formation of tephra with finer grain size distribution than mafic material (Rose & Durant, 2009). Moreover, energetic magma fragmentation (Zimanowski et al., 2003) and aerial volcanic plume collision (Rose & Durant, 2009) could lead to finer tephra proportions.

Tephra dispersion

When fragmented magma (tephra) associated with hot gases is propelled out of the volcano into the atmosphere, it forms a vertical buoyant eruption column that can rise at altitudes up to several tens of kilometres. After reaching its maximum height, the eruption column is picked up by the wind and dispersed laterally to form a volcanic plume that can travel across long distances. Dispersion of tephra is mostly correlated to wind speed, atmospheric conditions and the height of the eruption column (Carey & Sparks, 1986; Jenkins et al., 2015). During transport, tephra sediment out of the plume and at different rates, depending on particle density, size and shape (Cashman & Sparks, 2013). Thus, larger particles fall rapidly near the source volcano, while finer ones are transported farther away with the wind (Blong, 1984; Bonadonna et al., 1998). As a result, the thickness and grain size characteristics of tephra deposits vary spatially. illustrates spatially distributed field measurements of the deposit thickness, and tephra maximum grain size interpolated to produce isopach and isopleth maps.

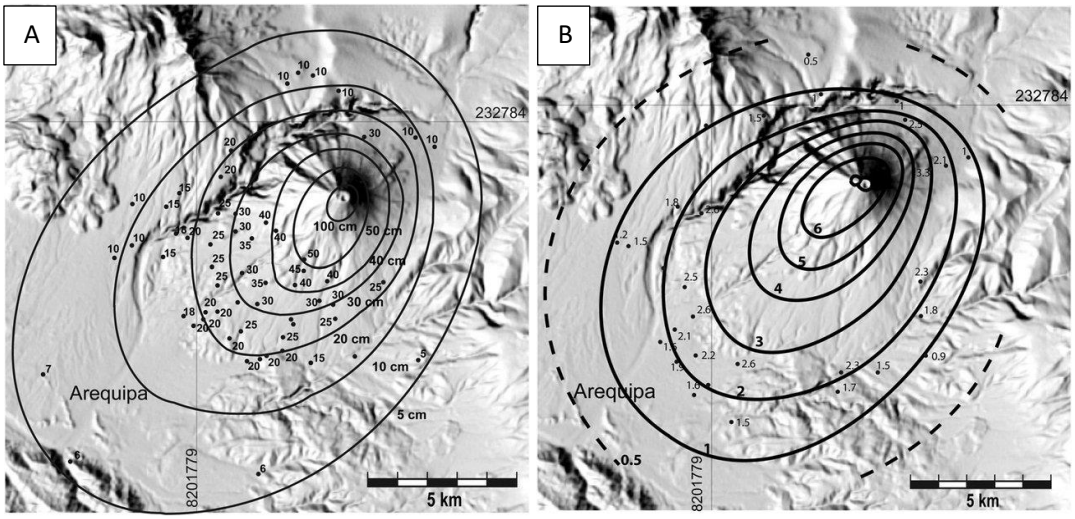

Figure 4: Isopach map showing the measured thicknesses for the tephra deposit (A). Isopleth map showing the maximum diameter (cm) of pumice and lithic fragments from the tephra deposit (B). Source: Cobenas et al., 2012.

Depending on the proximity of crops to the volcano and the distribution (deposit thickness and grain size) of tephra fallout, agriculture will be more or less affected.

2.2.2 Tephra impact on crops

After an eruption, tephra can be deposited into different environmental compartments, causing various impacts (Cronin et al., 2003). The impacts are usually associated with physical, chemical, and biological effects (Ayris & Delmelle, 2012), as described below. As agriculture is one of the main economic sectors in volcanic areas, crops are often exposed to tephra hazards. The impact of tephra on crops is a function of the intensity of the hazard and the vulnerability of the agrarian system (Craig et al., 2016). Several factors influence crop vulnerability to tephra. Four factors were identified by Craig et al. (2016) as having the greatest impact on crop vulnerability:

1. The thickness of the tephra deposit
2. The climate and the amount of precipitation
3. The crop maturity (time of the year during the tephra fall)
4. The infrastructures of the farm (mitigation factor)

Thickness measured of the tephra deposit on the ground is typically the most common parameter used to explain the severity of a tephra fall (Jenkins et al., 2015; Rosi et al., 1993; Wilson et al., 2012). This method is appropriate for relatively crude assessments of tephra vulnerability. However, it tends to neglect other tephra characteristics (grain, size, composition, abrasiveness, etc) that also influence, the level of damage on crops sustained. Recently, the tephra loading on plants has been more used to assess the impact generated by tephra on crops (Jenkins et al., 2015; Macedonio & Costa, 2012). It consists of a mass of tephra per unit area (e.g., kg m^{-2}) which is a common output of numerical tephra fall models. The

conversion between mass load and thickness can be obtained if the bulk density of the tephra deposit is known.

Mechanical, chemical and physiological stresses are three different types of impacts to which vegetation can be exposed. However, they are not independent of each other. For example, physiological impacts could be a consequence after a direct mechanical and chemical stress (Ligot et al., 2022).

Mechanical impact

When tephra lands onto crops it can induce mechanical impacts, the most common ones being smothering, burial, lodging, abrasion, and abscission of leaves and fruits (Figure 5). Most of these impacts result from tephra retention on crops. Tephra retention on foliage depends on several variables, and many of them are plant specific. Roughness of the plant surface leads to a better retention of tephra, making the deposit less susceptible to erosion caused by wind and water (Cook et al., 1981). Conversely, smooth and waxy leaves are more sensitive to wind and water exposure and have a weaker capacity to retain tephra (Smith & Staskawicz, 1977). Thus, the retention of tephra on crops influences the possible mechanical impacts induced. The main parameters controlling the intensity of these mechanical impacts are the thickness of the tephra deposit (Antos & Zobel, 2005) and its grain size distribution, as well as the type of vegetation (Mack, 1981). Mechanical impacts can be lethal to the plant if the deposit of tephra is too important, for example, a deposit of 500 to 1,500 millimetres can heavily kill some shrubs. The larger the plant diameter, the less sensitive the plant is to burial (Neild et al., 1998). However, some plants buried under tephra were able to survive by moving, and transforming their morphological structures, and growing new crowns (Antos & Zobel, 2005). Even if the plant is not killed by burial, the tephra mass load can cause damage to the leaves, or breakage of the branches if they are too brittle (Eggler, 1948). In addition, the combination of wind and tephra usually results in plant abrasion and damage to the leaves (Murata et al., 1966). These conditions then lead to a greater susceptibility of the plant, a greater exposure to pathogens (Cook et al., 1981) and also a greater risk of leaf abscission (Black & Mack, 1984). Mitigation techniques by rain, wind, or human hand are also a source of abrasiveness (Ligot et al., 2022).

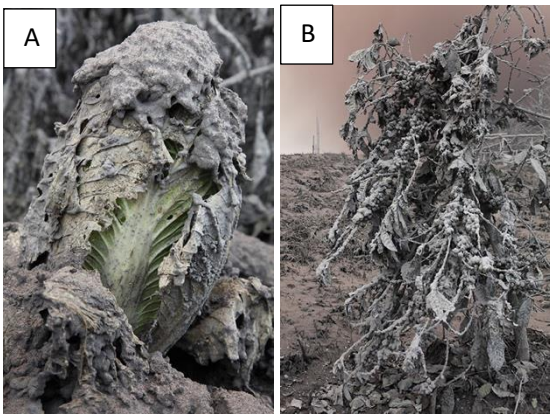

Figure 5: Photos of mechanical impacts of tephra on vegetation: lettuce buried by tephra (A) and coffee plant bent under the weight of tephra (B) after the 2014 eruption of Sinabung, Indonesia. Source: Photo volcanica, 2023.

Chemical impact

Chemical damage is most likely caused by the contact between the deposit of tephra and water (Cook et al., 1981). In this case, the release of halide and sulphate salts from the tephra particles may occur on the leaf surface (Wilson et al., 2007), which will damage the leaf cuticle. These salts will dissolve in the water present on the leaf surface, forming a saline solution that can penetrate the plant through the stomata and cuticles (Fernández & Eichert, 2009). The most recognizable impacts are the appearance of necrosis, dry, yellowish, or curling leaves on the plant (Mack, 1981; Wilson et al., 2007).

The presence of elemental sulphur and pyrite in small amounts in the tephra could cause acidification of the leaf surface. This is due to the formation of sulphuric acid upon oxidation of these minerals when exposed to rain. Leaf acidification may result in greater vulnerability of the leaf to drought and desiccation, which may induce necrosis (Percy & Baker, 1988). An acidic solution at the leaf surface may leach several nutrients, such as calcium, magnesium and potassium, from the leaf due to ion exchange reactions (Adams & Hutchinson, 1987). Moreover, an increase in the wettability of the leaf produce a higher exposure to acidic solutions on surface tissues (Haines et al., 1985). These impacts on foliage depend on the tephra composition and the tephra mass load on the leaf.

Physiological impact

The presence of tephra particles on plant foliage slows down or even stops plant photosynthesis through different mechanisms. Tephra deposited on leaf surfaces create a barrier for light interception (shading effect), thereby affecting photosynthesis (Cook et al., 1981). It was shown that a deposit of 10 g m^{-2} reduces photosynthetic activity on pine needles by 98% (Hinckley et al., 1984). The presence of dark tephra on foliage induces an increase in light absorption, which in turn increases leaf temperature. This process affects photosynthesis due to a higher transpiration rate (Hirano et al., 1995). Very small tephra

particles (< 2 µm) may obstruct stomata and disrupt gas exchanges between the leaf and the atmosphere, and thus the photosynthesis processes (Hinckley et al., 2011; Hirano et al., 1992). As a result of reduced photosynthesis, this may lead to early leaf senescence and fruit drop or speckled aspect (necrosis, chlorosis; Figure 6) on fruits and leaves (Mack, 1981).

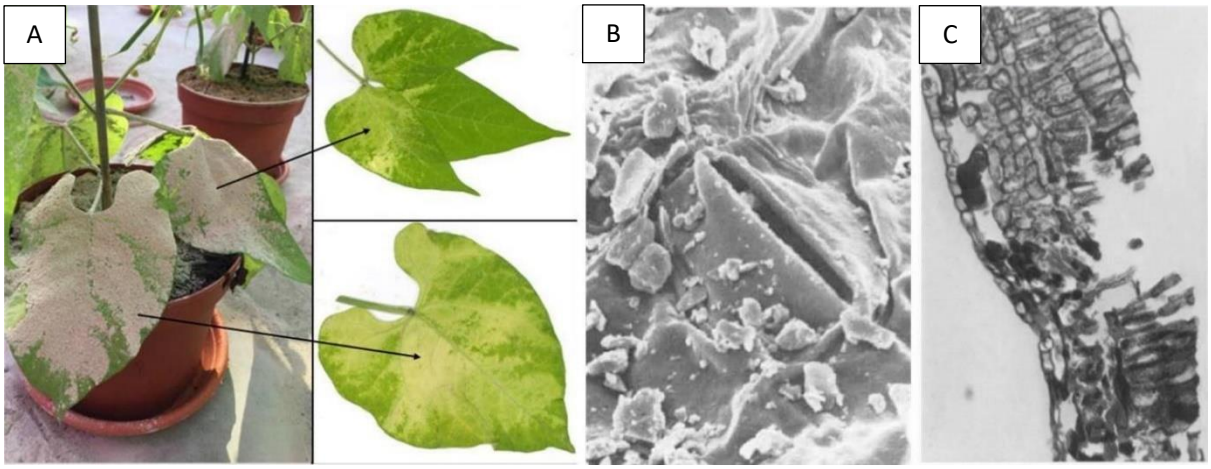

Figure 6: Chili pepper leaves with depigmentation where tephra lay (A). SEM image of tephra inside a stomata on the lower epidermis of an apple leaf after the 1980 eruption of Mt. St. Helens, USA (B) and cross-section (187X) of abscised leaf of Lombardy poplar after tephra abrasion showing removal of the epidermis and damage to the mesophyll (C). Sources: Ligot et al., 2022 (A), Kennedy, 1980 (B), Black & Mack, 1984 (C).

2.2.3 Tephra properties governing impacts

Particle size, mass load, bulk and surface compositions, abrasiveness and colour of tephra are some of the properties that determine the impact of tephra on crops (Neild et al., 1998). The governing properties of tephra, such as its chemical and physical characteristics, are mostly determined by the eruptive style and magma composition. Wind and rain can also influence the retention of the tephra deposit on crops (Jenkins et al., 2015).

Tephra particle size

The distribution of particle size is an important property, fine particles (< 100 µm) are transported further away from the volcano and thus spatially extending the potential impacts of tephra (). Thin particles are formed during more energetic fragmentation because of the high amount of over-pressured bubbles in the magma (Rose & Durant, 2009). Figure 7 shows typical tephra grain size distributions for an explosive eruption, classified with the Krumbein phi scale. It ranges from -4.0 (~16 mm) to 10.5 (~1 µm).

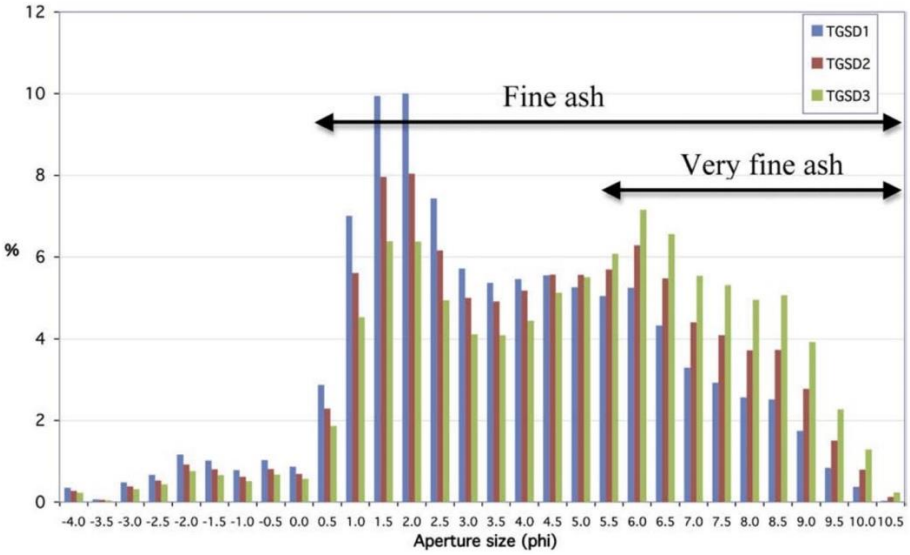

Figure 7: Total grain-size distribution (TGSD), of 4 April 1982 eruption of El Chichón, Mexico. Source: Rose & Durant, 2009.

The size of tephra particles influences their retention on the plant leaves (Miller, 1967). Finer particles tend to cover more efficiently leaf surfaces than coarser particles (Ligot et al., 2022). Fine particles may also be more chemically reactive because of their large specific surface area (Lowell et al., 2004). More generally, for the same tephra mass load, the severity of impact on photosynthesis is greater with smaller particles. It induces a larger shading ratio, a reduction of light interception and stomatal conductance, and an increase in leaf temperature (Hirano et al., 1992).

Mass load

The tephra mass load corresponds to the thickness of the deposit for a defined density. It is an important parameter, often used to describe tephra impacts on crops. In a recent work assessing exposure to tephra (Jenkins et al., 2022), three different thresholds of tephra mass load were studied: 1 kg m^{-2}, 5 kg m^{-2}, and 100 kg m^{-2}, corresponding to deposit thicknesses of ~ 1 mm, ~ 5 mm and ~ 100 mm, respectively (i.e. considering a bulk deposit density of 1 g cm^{-3}; Eychenne et al., 2012). Damage increases with tephra mass load (Miller, 1967). However, significant reduction in crop yield loss is already observed at tephra mass loads as low as 0.5 kg tephra m^{-2} (Ligot et al., 2022). As mentioned in section 2.2.1, thinner deposits are formed further away from the volcano and are mostly composed of fine tephra particles. While thicker deposits are accumulated near the volcano and are composed of a wider range of grain size (Figure 4).

Chemical composition of tephra and their impact on vegetation

The chemical composition, and more specifically, the surface composition of tephra is the major component influencing its reactivity with the environment. The main soluble elements are calcium (Ca), chlorine (Cl), sodium (Na) and sulphur (S) with occasional significant

concentrations of Al, fluorine (F) and Mg (Ayris & Delmelle, 2012). The presence of these soluble elements is mostly due to the adsorption of volcanic salt aerosols on tephra surface (Delmelle et al., 2007). The surface composition of tephra is the main driver behind chemical damage.

Shape and abrasiveness of tephra

The shape and abrasiveness of tephra depend on the fragmentation mechanism during the eruption which is influenced by factors like the properties of the magma (viscosity, temperature, and composition), and the conditions during the ascension and eruption of the magma (Liu et al., 2015). Tephra shapes are commonly irregular and angular (Figure 8), but spherical shapes are sometimes observed. The sharpness of tephra not only affects its abrasiveness but also its optical properties and residence time in the atmosphere (Riley et al., 2003).

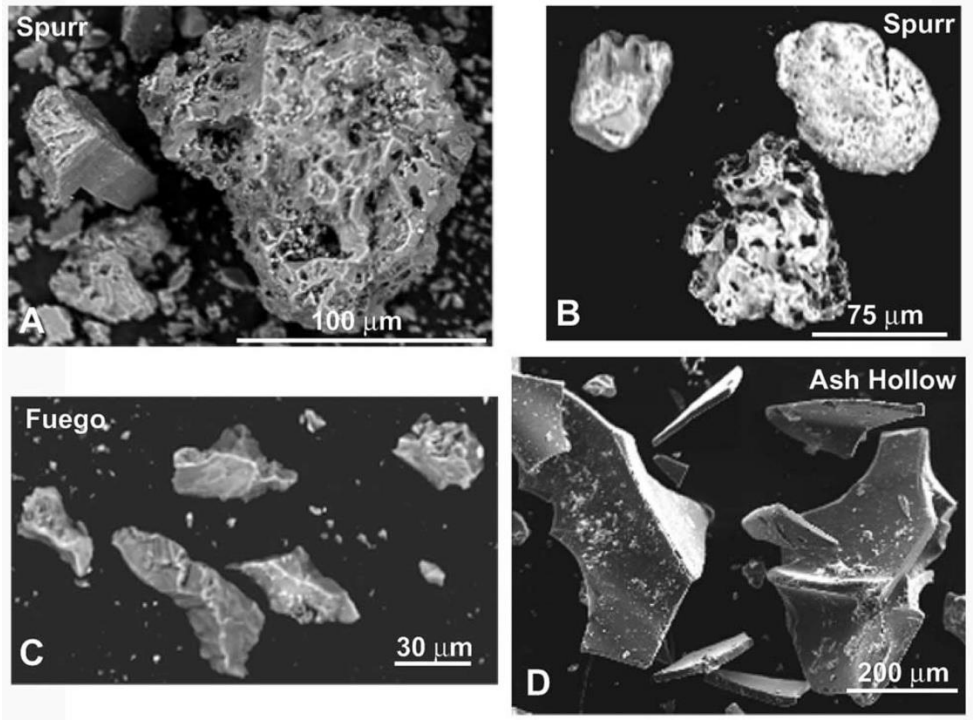

Figure 8: Examples of irregularly shaped ash particles. Equant mineral grain at left and a small pumice clast at right from the August 1992 Spurr eruption in Alaska, USA (A). Pumice clasts from the August 1992 Spurr eruption (B). Angular glass bubble wall shards from the 14 October 1974 Fuego eruption (C). Bubble wallshards from the Ash Hollow Member ash in Nebraska (Miocene) (D). Source: Riley et al., 2003.

Colour of tephra

The colour of tephra is mostly driven by its bulk composition (section 2.2.1), but also by its grain size. Basaltic tephra (low-Si and High-Fe content) is dark coloured (brown to black). Whereas tephra with high Si and low Fe content reflects and transmits more visible light,

resulting in a paler colour (Scholze, 1991). Hirano et al. (1992) indicate that a deposit of dark tephra increases leaf temperature more than a light-coloured tephra. It also has a greater effect on leaf photosynthesis, and potentially plant growth, due to a stronger shading effect.

2.3 Quantifying tephra risk for agriculture

A risk is a combination of hazard, exposure, and vulnerability. A hazard is defined as a natural phenomenon which could have a negative impact in space and time (e.g., an eruption). Exposure is the presence of any element in the hazard zone. Vulnerability is a condition that makes an element more sensitive to the hazard (Fournier d'Albe, 1979).

Nowadays, risk assessment is key to evaluate probabilistically or deterministically the consequences of a hazard. Different approaches to assess risks and impacts have been developed over the past decades in order to reduce damage and develop mitigation measures (Craig et al., 2016). To assess the risk of tephra on crops, it is necessary to describe the three components creating the risk (tephra hazard, crop exposure, and crop vulnerability). This is illustrated in Figure 9.

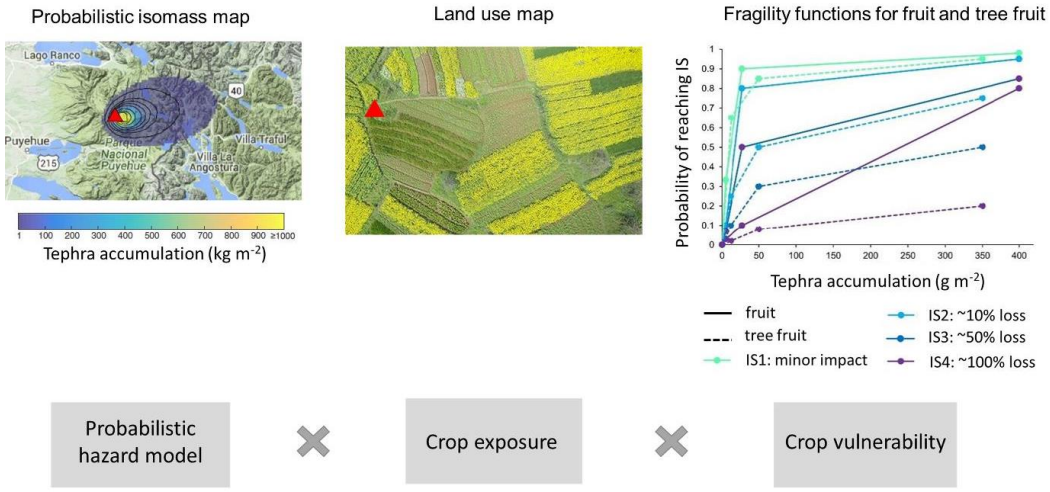

Figure 9: Tephra fall risk assessment framework for crops, with impact states (equivalent to damage states) abbreviated as IS. The probabilistic map and the fragility functions are presented in Biass et al. (2016) and Craig et al. (2021), respectively.

Volcanic hazards are usually described by probabilistic hazard models (Biass & Bonadonna, 2013; Jenkins et al., 2012). Significant progress in the modelling of tephra dispersion and tephra fallout distribution have been made in the past two decades. Usually, tephra fall simulations are implemented using a diffusion-advection model, such as the numerical model TEPHRA (Bonadonna et al., 2005), but other approaches exist. Crop exposure can be inferred using land use maps to assess the types, distribution and extent of various crop fields occurring in the area that may be affected by tephra fallout. Finally, the description of crop vulnerability can vary from a simple qualitative assessment to the construction of crop

fragility functions. These fragility functions are usually considered as a useful tool to provide quantitative information about crop vulnerability, as they show a relationship between hazard (tephra mass load) and impact (probability of reaching an impact state (IS)) in a continuous way (Figure 9).

However, data on crop vulnerability are quite scarce because data collection right after an eruption is often difficult (Jenkins et al., 2014). In addition, post-event impact assessment is still a young study field, making data on crop vulnerability to tephra often incomplete. In the absence of empirical data, a more qualitative method can be used. Impacts are then categorized on a damage state scale, while considering the relationship between the intensity of the hazard and the damage induced. Obviously, the vulnerability of crops depends on many other factors, the categories created in the qualitative assessment are only indicators. Even if these studies are carried out by experts, many assumptions are required, which leads to significant uncertainties (Jenkins et al., 2014).

2.4 Remote sensing to collect crop vulnerability data

Crop vulnerability is often associated with the yield loss caused by a tephra deposit. Different process-based models exist to quantify crop yield, such as AFRCWHEAT2 (Porter, 1993), CERES-Maize (Jones et al., 1986), STICS (Brisson et al., 2003), etc. However, these models required knowledge of many agro-environmental parameters that are specific to the study location. Alternatively, remote sensing data allow more reliable monitoring and prediction of crop production (Battude et al., 2016). Satellite-based models of crop production use various vegetation indices to estimate the biomass and crop yield (Dong et al., 2003; Wessels et al., 2006).

Remote sensing is based on the utilisation of specific parts (visible light, infrared, radiowaves) of the electromagnetic (EM) energy reflected or emitted by the Earth's surface (Tempfli et al., 2009). The EM energy is acquired by a sensor (Imam, 2019; Sishodia et al., 2020), that can be placed at different heights above the earth's surface, ranging from just a few centimetres above target or very far away in the atmosphere (Kerle et al., 2004). The sensor is usually mounted on a platform that can be in movement (satellites, planes, drones…) or static (tripods, handheld, towers…). The advantage of using remote sensing instead of other methods is that it provides cost effective, rapid and regular data across time and space from dangerous places (James et al., 2020).

2.4.1 Crop monitoring

The use of multispectral sensors is particularly interesting in agriculture monitoring as they capture specific wavelengths of the visible [0.4 to 0.7 µm] and near infrared and short-wave infrared [0.7 to 2.7 µm] parts of the spectrum, which are commonly used to calculate vegetation indices (Xue & Su, 2017).

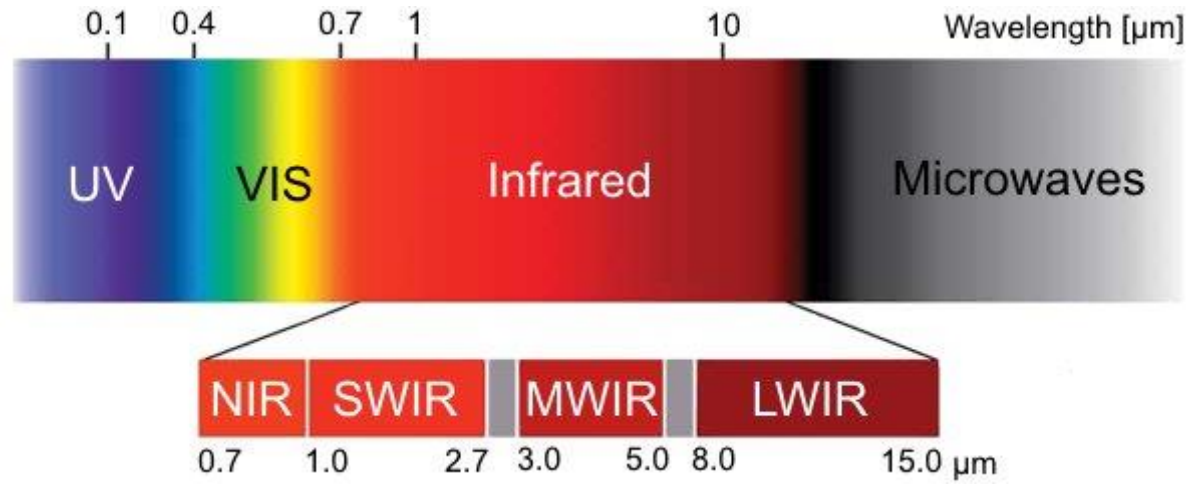

Figure 10: The electromagnetic spectrum, with the ultraviolet (UV), visual (VIS), near-, short-, mid-, and long-wavelength infrared (NIR, SWIR, MWIR, LWIR), and microwave wavelength ranges shown. Source: Hyll, 2016.

These vegetation indices are mathematical expressions that combine measured reflectance in many spectral bands to produce a value that helps assess crop growth, estimate plant photosynthesis, abiotic and biotic stress, plant nutrient contents, etc (Chang et al., 2020; Chlingaryan et al., 2018; Nagasubramanian et al., 2019).

The normalized difference vegetation index (NDVI) is one of the most widely applied indices to monitor land cover and to assess crop health (Kaufmann et al., 2003). It is a convenient index to use as it reduces many forms of multiplicative noise such as differences in solar illumination, cloud shadows, some atmospheric attenuation, some topographic variations which are present in multi-date imagery (Baret & Guyot, 1991). NDVI can be estimated from the measurement of the reflectance of the red and near-infrared spectral bands according to:

$$NDVI = \frac{NIR - RED}{NIR + RED} \quad (1)$$

where NIR and RED are the near-infrared energy (~ 830 nm) and red energy (~ 640 nm) reflected by the plant, respectively (Myneni et al., 1995). NDVI values range from -1 to 1, where values close to one correspond to dense green leaves and negative values indicates absence of vegetation (Pettorelli et al., 2005). The NDVI is attractive because it has a good ability to assess vegetative stress (Huang et al., 2021). For example, it has successfully been used to detect blotch spot disease (Kumar et al., 2016), as well as water stress in crops (Maselli et al., 2020).

Other vegetative indices, including the Simple Ratio (SR), Soil Adjusted Vegetation Index (SAVI) and Transformed Soil Adjusted Vegetation Index (TSAVI), are also commonly used (Ma et al., 2017). But the NDVI is one of the most used, due to its simplicity in usage and capacity to distinguish crucial plant attributes.

2.4.2 Tephra spectral properties

Accurate tephra spectral measurements are necessary to generate reliable interpretation of its mineralogical and chemical properties (Adams, 1974). Many minerals and rocks have unique spectral signatures with narrow absorption bands. Spectrometry can represent these narrow bands and thus map the surface mineralogy of these rocks. The use of spectrometry with remote sensing technologies enables to produce detailed spectral reflectance curves for each pixel in the image acquired by the remote sensor (van der Meer, 1999). In fact, tephra spectral properties are influenced by several parameters like the chemical composition and mineralogical content as mentioned, but also by the grain size distribution and water content. Only few studies report the spectral properties of tephra.

Different grain size classes from the same tephra have different spectral properties in the visible-near infrared (VNIR). As shown in Figure 11, smaller grain size classes have a greater reflectance than coarser particles due to higher albedo (Adams & Filice, 1967). Indeed, smaller particles have a higher specific surface area compared to larger particles because they have a greater surface area relative to their volume. This specific surface area enables them to scatter the light more efficiently. This is why fine particles have a significant impact on the spectral properties of tephra (Mustard & Glotch, 2019; Mustard & Hays, 1997).

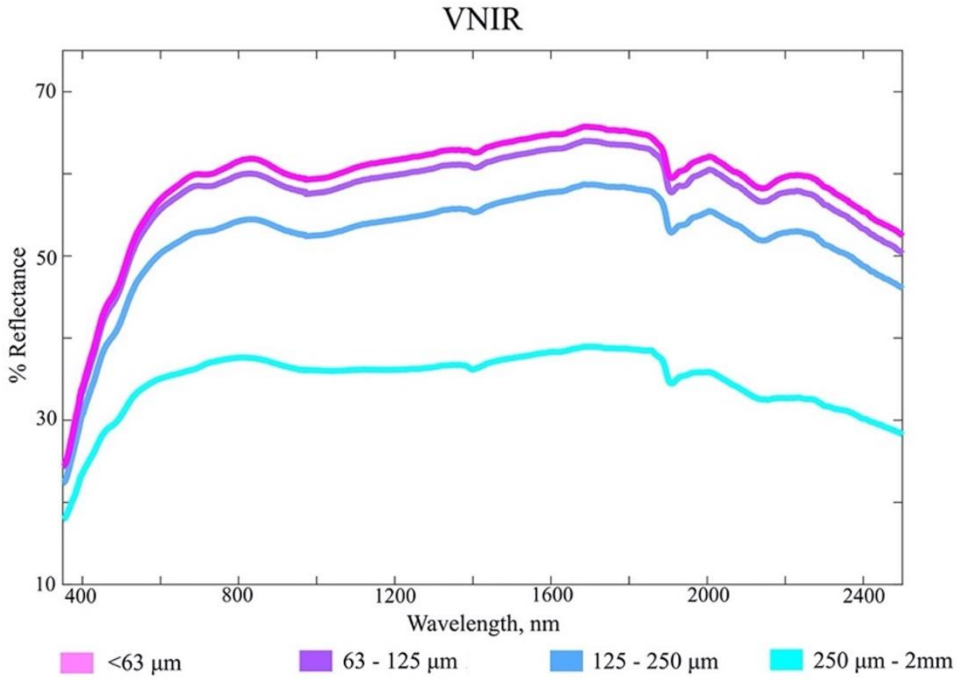

Figure 11: Spectral response of sieved tephra sample from the Pinatubo over spectral range (wavelength) from 350–2,500. Source: Leight et al., 2022.

The bulk composition of tephra has a strong effect on its spectral signature because the proportion of its chemical elements induce specific colours to the tephra. As the concentration in silica (SiO_2) increases, the reflectance also increases in general. A greater content of SiO_2 leads to lighter coloured tephra, which in turn increases the albedo of the

sample (Leight et al., 2022). For example, felsic samples tend to have a larger range of reflectance (37-80% of reflectance for 74.0 weight % SiO_2) compared to basaltic samples (5-20% of reflectance for 48.8 weight % SiO_2; Figure 12).

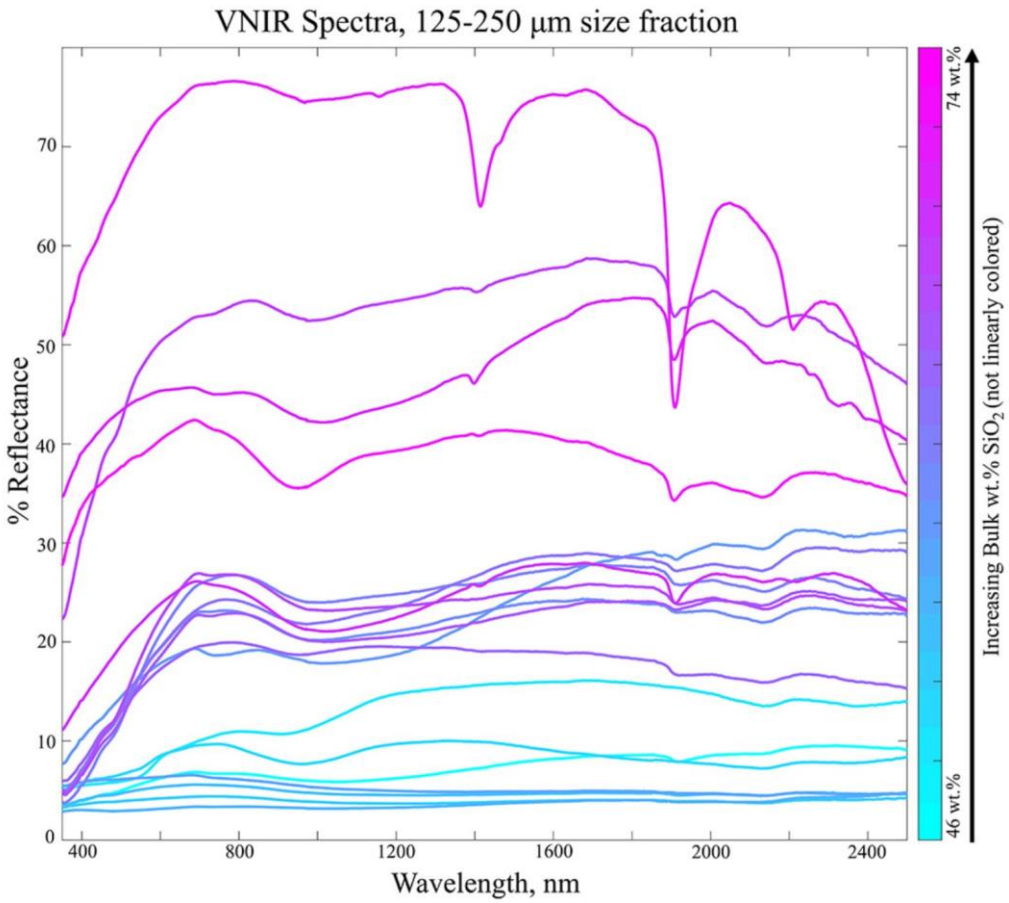

Figure 12: Spectral response of several tephra samples with 125–250 µm size fraction. Spectra are coloured by increasing bulk weight% SiO_2. Coloration is not linearly applied to weight% SiO_2 values. Source: Leight et al., 2022.

However, some components could reduce the reflectance signal of tephra. The albedo of spectra can reduce in the VNIR because of the presence of glass (Adams & Mccord, 1971). The variation of water content in the tephra samples also has an impact in the VNIR (Seidel et al., 2022). An increase in water content leads to a general increase in absorption. In the VNIR, the increase in absorption is also located at specific wavelengths with higher absorbance values. These specific absorptions are due to the characteristics of the water absorption bands at ~1,400 nm, ~1,900 nm, and ~2,200 nm (Crown & Pieters, 1987). However, in the absence of water in the tephra sample, the absorption at 1,900 nm peak is due to the atomic bond of Fe^{3+}, included in a tetrahedral coordination site.

2.4.3 Assessing crop vulnerability from crops spectral response

Crop vulnerability usually refers to yield loss when crop plants are exposed to tephra. Yield loss can be estimated by remote sensing with the help of vegetation indices. Retrieving crop

vulnerability to tephra through remote sensing could be done by measuring the yield difference between crops and crops covered with tephra. It has never been done before. However, few studies have been carried out to monitor dust deposits on vegetation with high accuracy (Kayet et al., 2019; Lin et al., 2021; Ma et al., 2017; Zhu et al., 2020). Most of these studies only assessed the impact of dust deposit on the spectral response of plants (Figure 13). To obtain the yield loss, it would be necessary to use models linking vegetation indices to yield estimation (Dong et al., 2003; Wessels et al., 2006).

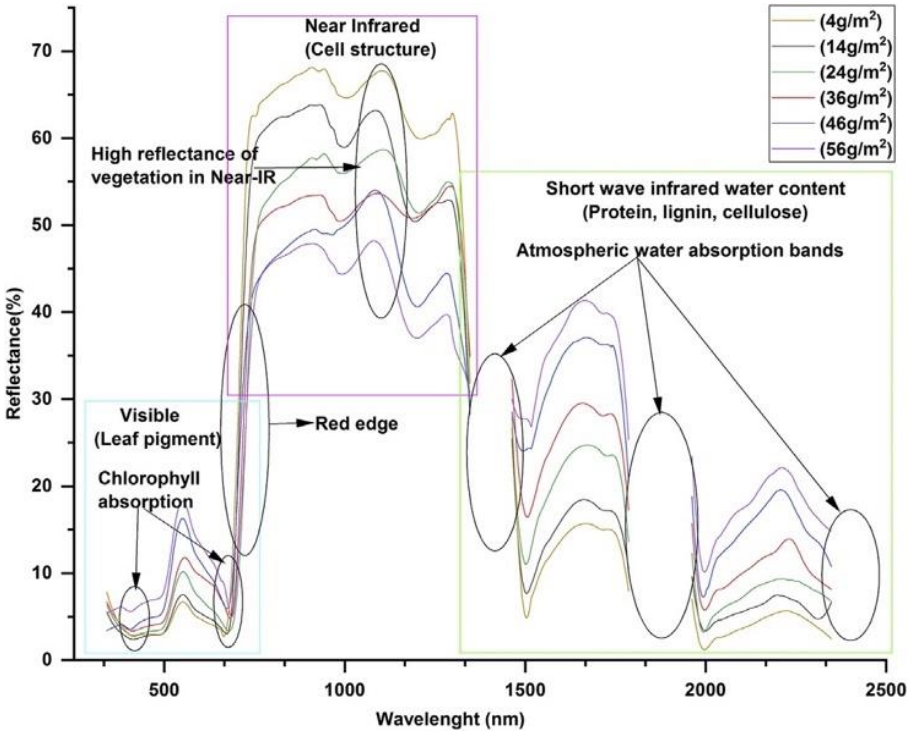

Figure 13: Spectral signature of dust-covered leaf with different dust amounts (g m^{-2}). Source: Kayet et al., 2019.

The NDVI is considered as one of the most useful indices to identify dust deposit on vegetation (Ho, 2009). Kayet et al. (2019) found that a decrease of NDVI is associated to a dust deposit on vegetation, by comparing one year without mining activities and eleven years after mining activity. The decrease of NDVI depends on the dust mass load sampled during field operations. This model enables accurate estimations of dust deposit on vegetation (RMSE = 0.06 g m^{-2} | R = 0.90) for a mass load range of 4 to 84 g m^{-2}. During this study, it was assumed that dust pollution was deliberated the primary stress issue affecting vegetation in the mining area.

3 Objectives of the thesis

The objective of this thesis is to investigate and characterise the spectral radiative response of tephra on crops. To achieve this goal, two experiments were conducted, each contributing to a deeper understanding of the subject.

The first part of the research involved measuring the spectral response of three distinct tephra specimens using a high-precision spectrometer. This step allowed us to obtain accurate reflectance measurements across the entire visible-near infrared spectrum. By analysing the reflectance data, specific information about each tephra specimen were extracted, providing valuable insights into their unique properties. This experiment helped to establish a baseline understanding of how tephra interacts with light and how a deposit of tephra on vegetation might impact the reflectance of leaves.

In the second part of the research, dedicated efforts were made to study the spectral signature of tephra on crops in an on-field experiment. A drone was used to capture the spectral response of wheat plants before and after being covered with various tephra deposits. The collected reflectance data from the drone's observations was then analysed and processed to calculate a vegetation index. This index serves as a quantitative measure of the health and vigour of crops, providing critical insights into the potential disruptions in reflectance caused by tephra deposits. The comparison of the results obtained for the different deposits also enables to retrieve the main factors influencing the spectral response of wheat covered with tephra.

By combining the results obtained from both experiments, a comprehensive understanding of the spectral radiative response of tephra on crops can be established. The purpose of this research is to contribute to the current knowledge regarding the risks associated with tephra deposition on vegetation. As mentioned earlier, there is a scarcity of data regarding the vulnerability of crops to tephra. Therefore, we attempted to utilise remote sensing techniques to collect reflectance data on tephra and reflectance data on tephra deposits on wheat plants. These spectral data can be further used in future research to infer potential yield losses, thereby providing insights into the vulnerability of crops to tephra.

4 Materials and methods

4.1 Spectral response of three specimens of tephra

4.1.1 Samples preparation

Three tephra specimens from Laacher See, Mount Pinatubo, and Eyjafjallajökull volcanoes were studied. The Laacher See tephra is a tephra surrogate produced by grinding a rock quarried near the volcano in Germany. The Laacher See eruption took place 11,000 years ago and produced approximately five km^3 of pyroclasts and lava (Van den Bogaard & Schmincke, 1984) with a phonolitic composition (Table 1). The tephra surrogate was then processed at Centre Terre et Pierre at Tournai in Belgium to obtain a continuous grain size range of 0 to 3,000 µm.

The Mt. Pinatubo tephra correspond to the 12-15 June 1991 Plinian activity of the volcano. This eruption took place in the Philippines and was the second largest eruption of the last century (Newhall & Punongbayan, 1996). About 100 kg of tephra was collected in March 2016 at a site approximately six km northeast of Mt. Pinatubo. The material was retrieved from a 40-50 cm thick ashfall deposit. Bulk elemental analysis of the tephra indicates a dacitic composition (Table 1), similar to that reported earlier for the source magma. This suggests a negligible effect of weathering on tephra bulk chemistry.

The Eyjafjallajökull sample is the tephra produced during the 14-18 April 2010 eruption of Eyjafjallajökull volcano in Iceland. Tephra sampling was conducted three months after the eruption. The tephra has a basaltic trachy-andesite composition (Table 1).

Table 1: Bulk composition of tephra samples from Laacher See, Mount Pinatubo and Eyjafjallajökull volcanoes.

		Laacher See	Pinatubo	Eyjafjallajökull
Composition (weight %)	SiO_2	52.5	62.7	55.6
	Al_2O_3	21.8	17.2	14.1
	K_2O	9.6	1.4	1.8
	Na_2O	7.8	5.1	4.8
	Fe_2O_3	2.9	4.4	10.1
	CaO	1.5	5.6	5.3
	TiO_2	0.3	0.5	1.6
	MgO	0.2	2.8	2.6
	P_2O_5		0.2	0.4
	MnO		0.1	0.2

The aim of the spectrometry experiment was to obtain the distribution of the reflectance in the visible near-infrared (VNIR) for the tephra from Laacher See, Pinatubo and Eyjafjallajökull volcanoes. As the distribution of a tephra deposit around a volcano depends on its grain size (Figure 4), different grain size classes were analysed to define their individual spectral properties. The Wentworth scale distinguish four main categories: mud, silt, sand and gravel (*Wentworth (1922) Grain Size Classification*, n.d.). The sub classes of the sand category were used:

- Phi (ϕ): > 4 (<62.5 µm)
- Phi (ϕ): 3 - 4 (62.5-125 µm)
- Phi (ϕ): 2 - 3 (125-250 µm)
- Phi (ϕ): 1 - 2 (250-500 µm)
- Phi (ϕ): 0 - 1 (500-1,000 µm)
- Phi (ϕ): 0 - (-1) (1,000-2,000 µm)

A sample is the combination of one specimen of tephra with one grain size class (e.g., sample one: Laacher See < 63 µm). Due to a lack of material, the grain size classes ranging from 1,000 to 2,000 µm from Pinatubo and Eyjafjallajökull volcanoes could not be prepared.

In addition to single grain size classes analyses, the spectral properties of an unsieved (0-3,000 µm) subsample of the Laacher See tephra was also performed. This subsample was analysed because it was used for the second part of the thesis which consist of spraying tephra on crops. Laacher-See tephra was chosen because it is the material, among Pinatubo and Eyjafjallajökull, that is available in suitable quantities.

The tephra was dry sieved for 10 minutes using an AS 200 Control Retsh vibrating sieve shaker (Figure A-1). This allowed us to separate six size fractions: <63; 63–125; 125–250; 250–500; 500–1,000 and 1,000–2,000 µm. All grain size classes >63 µm were individually wet sieved to ensure that any small particles would be washed away. Finally, the sieved tephra was dried in an oven at 105°C for 48 hours. A grain size distribution analysis based on dynamic light scattering (NANOTRAC FLEX) with demineralized water was performed to verify that the grain size classes had been properly sieved (Figure A-2 and Figure A-3). The median diameter values of the <63; 63–125; 125–250; 250–500; 500–1,000 and 1,000–2,000 µm size fractions were 12; 179; 174; 401; 774 and 1,465 µm, respectively.

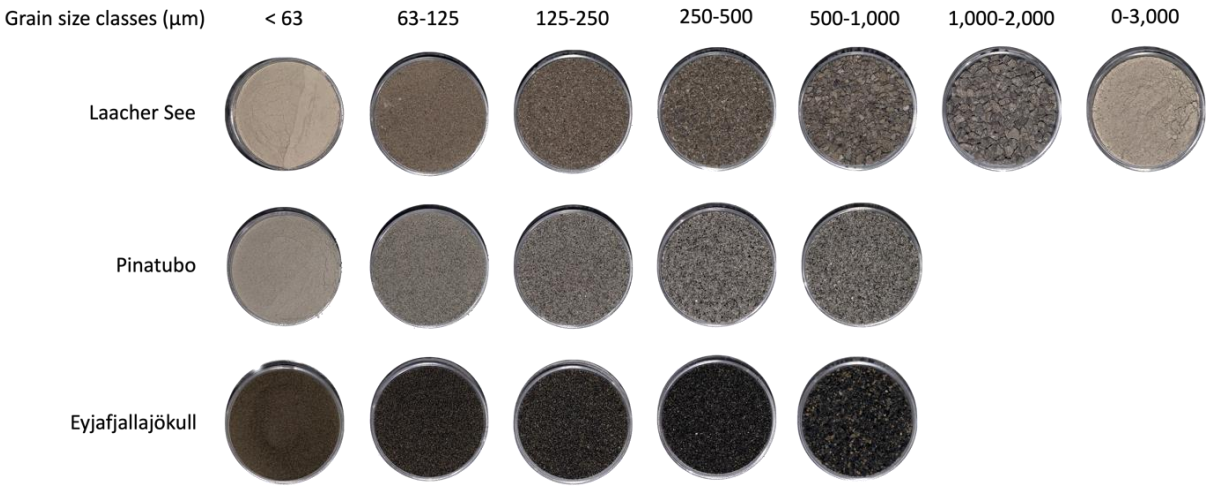

Figure 14: Photos of the Laacher See, Pinatubo and Eyjafjallajökull tephra samples analysed for their spectral properties. The different grain size fractions used for each tephra sample are shown.

Three replicates of each grain size class were weighted in small boxes of 9.57 cm^3 filled to the top. Knowing the volume occupied, it was possible to retrieve the mean bulk density of each grain size class (Table A-2). The humidity content of each sample was calculated by weighting it before and after drying in an oven at 80°C to remove any adsorbed water (Leight et al., 2022) for 48 hours (Table A-2). The measurement was done on three replicates of each grain size class. The humidity content was <1% for all samples, except Eyjafjallajökull <63 µm which have a humidity content of 1.24 %.

4.1.2 Spectrometric measurements

The FieldSpec® 3 Spectroradiometer collects the optical energy (VNIR and SWIR) reflected by, absorbed by or transmitted through a sample (ASD Inc, 2010). The device is capable of measuring the radiance from 350 to 2,500 nm. The VNIR is scanned with one scanning spectrometer (spectral range: 350-1,000 nm | spectral resolution: 3nm). The SWIR is done with two scanning spectrometers (spectral range: 1,000-1,830nm and 1,830-2,500nm | spectral resolution: 8nm each). Therefore, spectral discontinuities should be expected at 1,000 nm and 1,830 nm when operating with raw data. These discontinuities can be addressed by using the parabolic correction utility (ASD Inc, 2010). When the spectrometer registers a spectrometric measurement, it consists of the average of sets of 25 spectrometric measurements.

In order to get random sampling with a robust mean result, nine replicates were randomly collected from the sieved tephra, for each grain size class except for the Pinatubo 500-1,000 µm and Eyjafjallajökull 500-1,000 µm for which only two and eight replicates could be prepared (Figure 15). A total of 145 spectrometer scans were obtained (Figure 15).

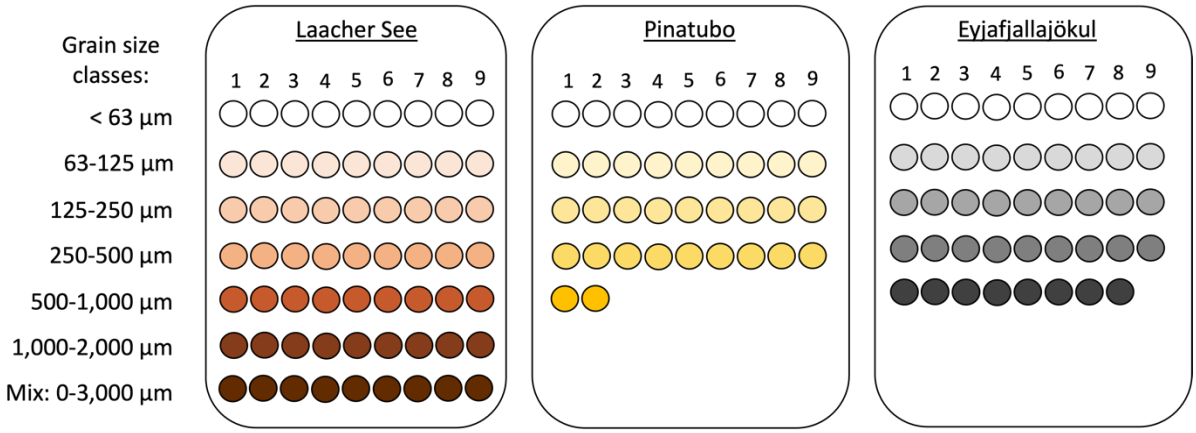

Figure 15: Sample distribution for each specimen of tephra and each grain size classes. Nine replicates were used for each grain size class, except in the cases of the Pinatubo and Eyjafjallajökull tephra, for which only two and eight replicates could be measured for the 500-1,000 µm grain size class.

At the end of the measurements of the set of nine samples of the same grain size class, a white reference was measured with white sand (in appendices in Figure A-1). The calibration of the spectrometer was done at the beginning of the measurement and repeated after two sets of nine samples throughout the whole experiment (Figure 16). The calibration of the spectrometer consists of scanning a panel made of polytetrafluoroethylene (PTFE) as standard measurement. The PTFE is nearly 100% reflective within the wavelength range of 350 nm to 2,500 nm.

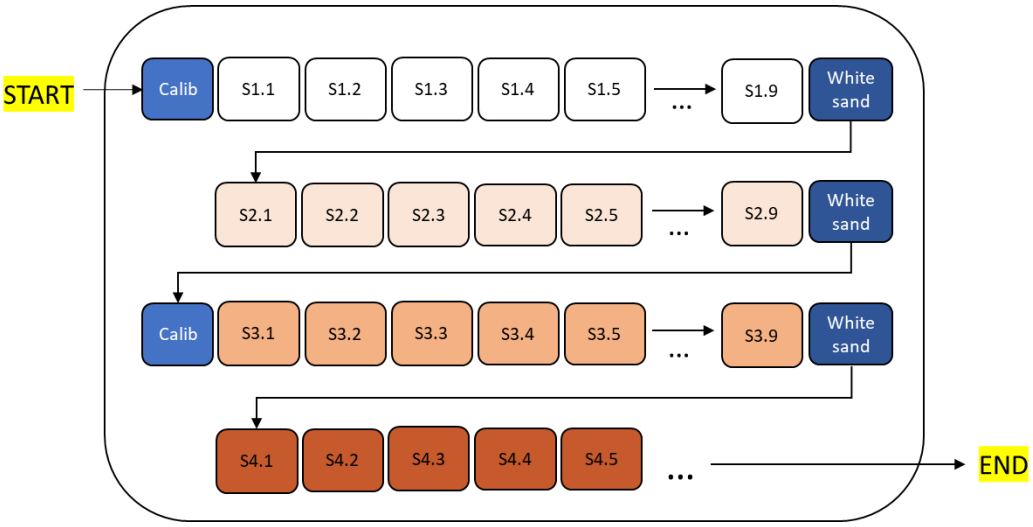

Figure 16: Spectrometer measurements order. Every two sets of samples, a calibration is needed and at the end of each set a white sand acquisition is needed. The process continues until each set of samples is done. Here the samples are annotated with two numbers, the first one corresponds to the grain size class (e.g., 63-125 µm); the second one is the number of the sample. For example: S3.2 is the second sample of the grain size class 125-250 µm.

4.1.3 Data treatment

Each measurement of the reflectance of the tephra samples was visible on RS3 Software Pack from ASD, and then stored in ASD files. Each reflectance spectrum was corrected with a parabolic correction utility at 1,000 and 1,830 nm because of spectral discontinuities due to the spectrometer (section 4.1.2). The software ViewSpec Pro was used to upload the files and export them in excel format. Finally, they were imported on Python to display them as graphs. The graphs show the average reflectance of the nine measurements for each grain size class, as a function of wavelength, with a 95% confidence interval for each curve. The confidence intervals were calculated as:

$$I_C = \left[\bar{x} - t_\alpha \frac{s}{\sqrt{n}} \; ; \; \bar{x} + t_\alpha \frac{s}{\sqrt{n}}\right] \quad (2)$$

with:

- I_C: the confidence interval
- $\bar{x}$: the mean reflectance
- t_α: the confidence coefficient ($t_\alpha = 1.96$ for a confidence interval of 95%)
- s: the standard deviation
- n: the number of samples

4.2 Spectral response of tephra on wheat plants

4.2.1 Site of the experiment

The experiment was conducted at the Alphonse De Marbaix farm (50°40'16.3"N 4°38'04.0"E), an experimental centre belonging to UCLouvain (https://uclouvain.be/fr/decouvrir/centre-de-michamps-et-ferme-de-marbaix.html).

Two plots of 27 x 8 m were dedicated to the experiment (Figure 17). A metal structure to hold tarpaulins is present above the plots but were not used in the experiment.

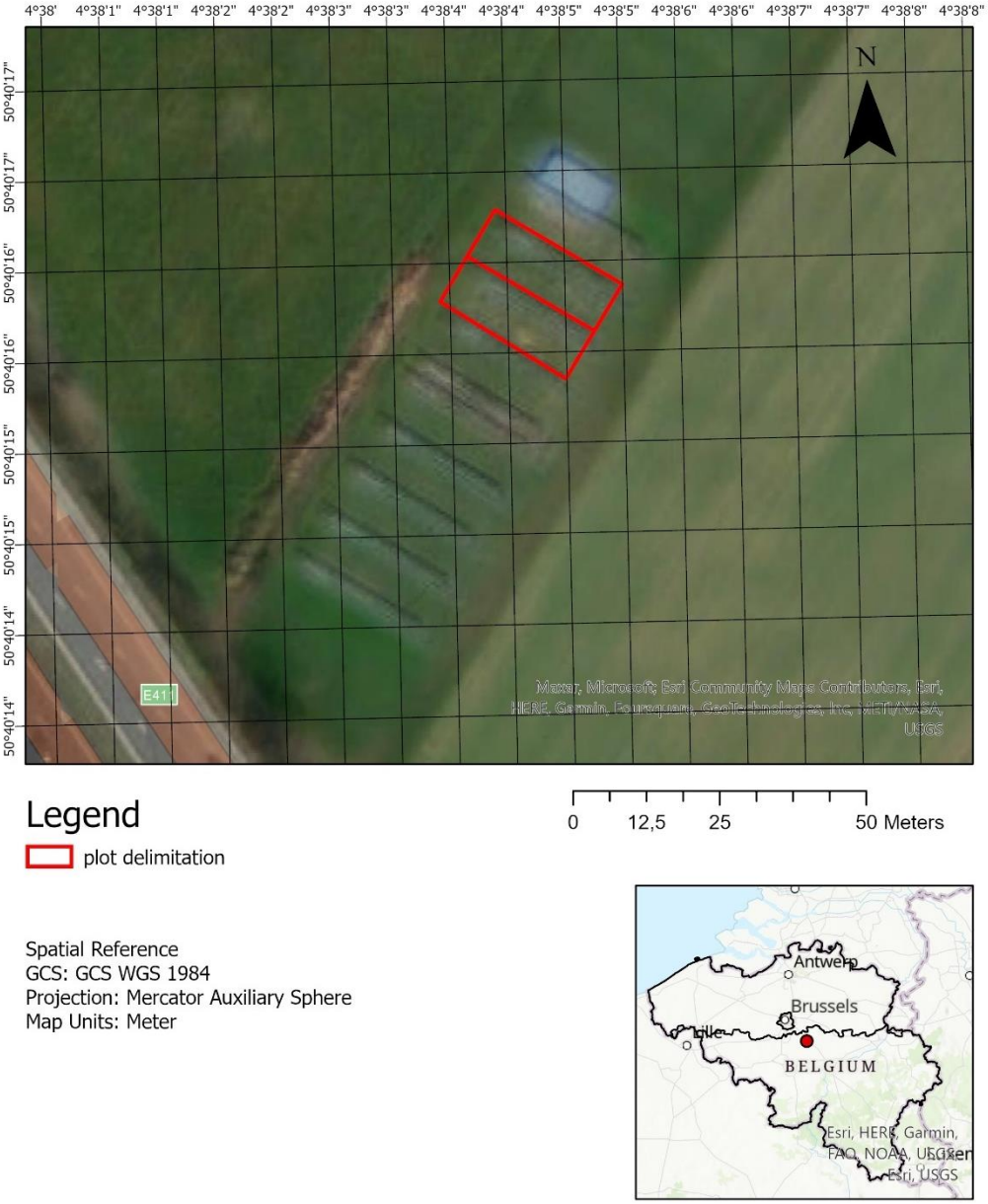

Figure 17: Location map of the study plots (framed in red) for the experiment at the Alphonse De Marbaix farm.

Corroy-le-Grand has a temperate oceanic climate with important rainfall throughout the year (~ 838 mm per year with an average temperature of 10.5°C; Climate-data.org, 2021). This climate is generally characterised by mild, rainy winters and relatively cool, wet summers. The hottest month of the year is July, and the coldest is January. The driest month is April with 57mm of rain and August is the wettest with 83mm of rain (Climate-data.org, 2021). Hourly air temperature, humidity, wind direction and speed, and solar radiation were recorded during the entire duration of the experiment using a weather station (METER Em50 data logger) installed ~ 2m above the ground.

The first plot was used in 2019 to 2022 for growing alfalfa. No fertilizer or phytosanitary inputs were applied to this plot. The second plot was cultivated in May 2020 with corn (*Zea mays* L.) in an open-ended high tunnel to study the impact on production of different tephra mass loads. The soil was ploughed and fertilized before this experiment. A second experiment was carried out on this plot from November 2020 to September 2021. The experiment consisted of spreading different tephra mass loads on winter wheat, at different phenological stages. The plot was ploughed in November before the wheat plantation, and two fertilizer applications occurred in March 2021 with TM orga. Homogeneity tests to assess any plant growth differences were performed during these experiments, they showed a good homogeneity of the plot. From September 2021 to September 2022, no action was taken on the plot, the parcel remained uncultivated.

4.2.2 Plant material and plot management

Wheat (*Triticum* spp.) has a global production that is more important than any other crops, such as rice, maize, and potatoes (FAO, 2002). Winter wheat (*Triticum Aestivum*) was chosen for the experiment because it is one of the most harvested crops in the world (FAO, 2022). The chosen variety is Alessio, which is a bearded variety. Its average height is 111 cm after heading and it is not susceptible to lodging (Dumont & Sinnaeve, 2021). Alessio variety is resistant against many plant diseases, it has a good yield and a good resistance to low temperature (DELIVAGRI, n.d.).

Alessio winter wheat is normally sown in autumn and harvested in August. Its development is divided into four phases. The first one is the tillering, followed by a period of stem extension, a period of heading and finally ripening (Figure 18). In our experiment, two phenological stages are studied as the soil cover evolves and the sensitivity of the plant to tephra deposition evolves. The phenological stages studied are part of the stem extension phase. That is why phenological stages 32nd and 41st of the Zadoks scale classification were chosen. They are referred to as early stem extension stage and late stem extension stage.

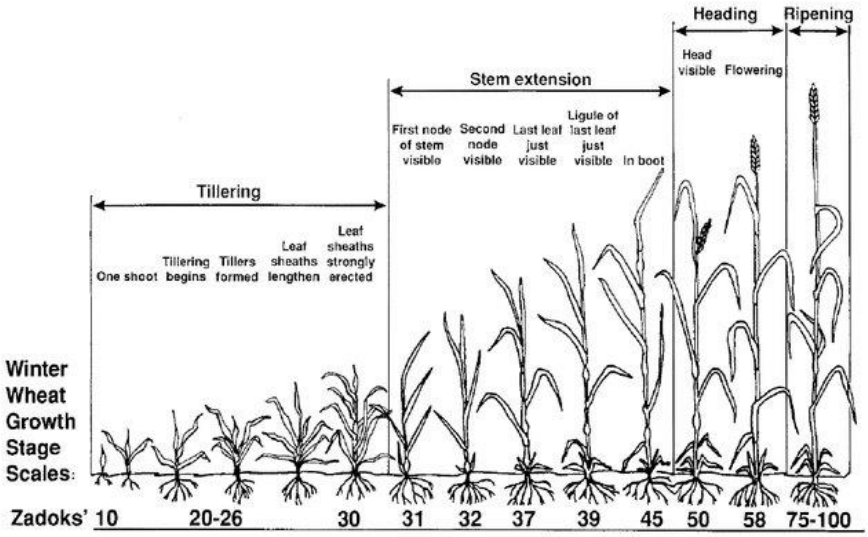

Figure 18: Zadoks' growth stages of winter wheat. Source: Basden et al., 2023. The different stages on the figure are divided with the Zadok's growth scale which is a 0-99 scale, describing in the most precise way, the growth stage of wheat plant. The first digit refers to the main growth stage (germination, seedling, tillering, stem elongation or jointing, booting, heading, flowering or anthesis, milk, dough, ripening). While the second digit describes the secondary stages (Fowler, 2018).

The cultivated plots underwent various operations prior to the experiment itself. After a weeding period, the winter wheat grains were sown at a density of 200 g m^{-2} on the 8th of November. Organic fertilisation and harrowing were performed after sowing on the 21st of February with 200 g m^{-2} of TMS orga bio (Organo TMS 3-2-2).

4.2.3 Tephra application

The choice of the tephra material and the types of treatments applied in the crop experiment are schematised in Figure 19. The Laacher See and Eyjafjallajökull tephra were used as sufficient material was available. The tephra were subjected to sieving, washing, and drying, as described in section 4.1.1.

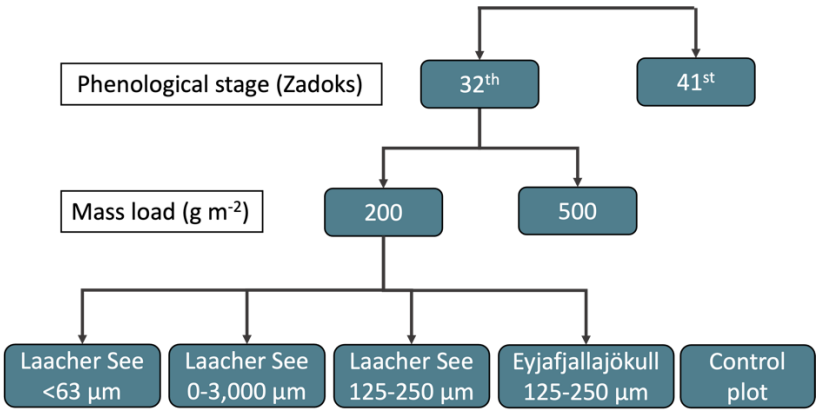

Figure 19: Different treatments used for the experiment.

Two plant phenological stages were studied and for each of them, two tephra mass loads were applied: 200 g m^{-2} and 500 g m^{-2}, corresponding to deposit thicknesses of approximately 0.2 mm and 0.5 mm, respectively (considering an average bulk density of 1.07 ± 0.12, cfr Table A-2 for each bulk density). These mass loads are typically in the range of values observed in distal regions affected by an explosive volcanic eruption. Depending on the magnitude of the eruption, these surface areas of these regions can vary from ~ 900 km^2 to ~ 160,000 km^2 (Bonadonna & Costa, 2012).

Four combinations of composition and grain size classes were applied on wheat plants: (i) Laacher See: 0-63 µm; (ii) Laacher See: 0-3,000 µm; (iii) Laacher See: 125-250 µm and (iv) Eyjafjallajökull: 125-250 µm. For the Laacher See tephra, three grain size classes were chosen to test the influence of grain size on retention by plant leaves (Ligot et al., 2022; Miller, 1967). Different tephra accumulation on foliage will probably influence the spectral response of wheat plants. The Eyjafjallajökull and Laacher See tephra have contrasting colours (Figure 14) and thus, different reflectance properties (Figure 27, see section 5.1). Therefore, we also tested the Eyjafjallajökull tephra (125-250 µm) to allow for comparison with the Laacher See tephra (125-250 µm). Six spatial replications were carried out for each treatment. This was necessary because of the heterogeneity of wheat growth in the field. Six subplots with pristine plants were kept as a control treatment.

In total, 102 subplots were needed for the treatments (Figure 20). To facilitate the experiment, the distribution of treatments for each sub-plot was assigned in the same way between the two plots. Each plot was divided across the width into two sections of three rows each (shown in green and blue in Figure 20). The western section was dedicated to the first early stem extension stage, while the eastern section was used later, when testing the late stem extension stage. No significant variations in wheat growth were observed among the sections. Within each section, eight treatments (combination of composition, grain size and mass load) were randomly distributed in each row. The controls plots are also randomly distributed in order to have one in each row. The random spatial distribution is used to counter heterogeneity in the soil properties, which may affect plant growth. The distribution of the treatments over the subplots is available in appendices in Figure A-5.

The delineation of the plots into subplots for the experimentation was carried out on the 17th and 18th of April using a thermal weeder to burn the wheat in the alleys between the subplots (Figure 20). Each plot is divided into three rows of 17 subplots.

First plot

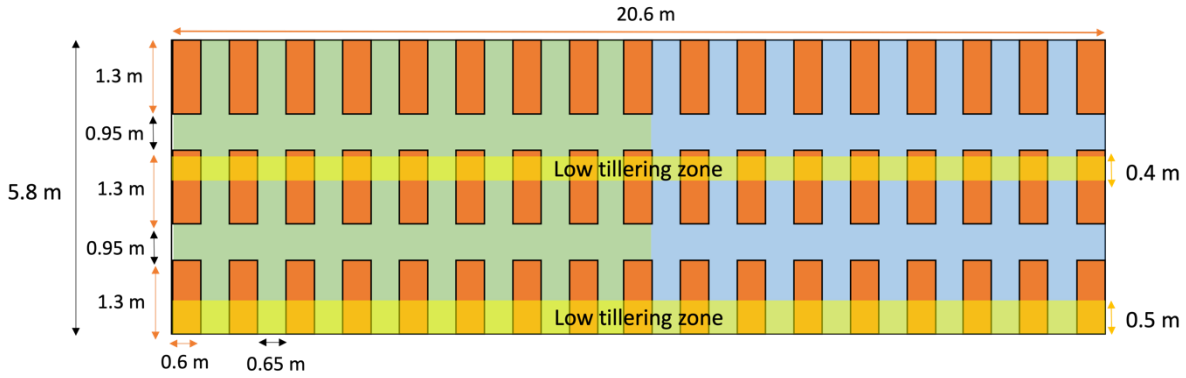

Second plot

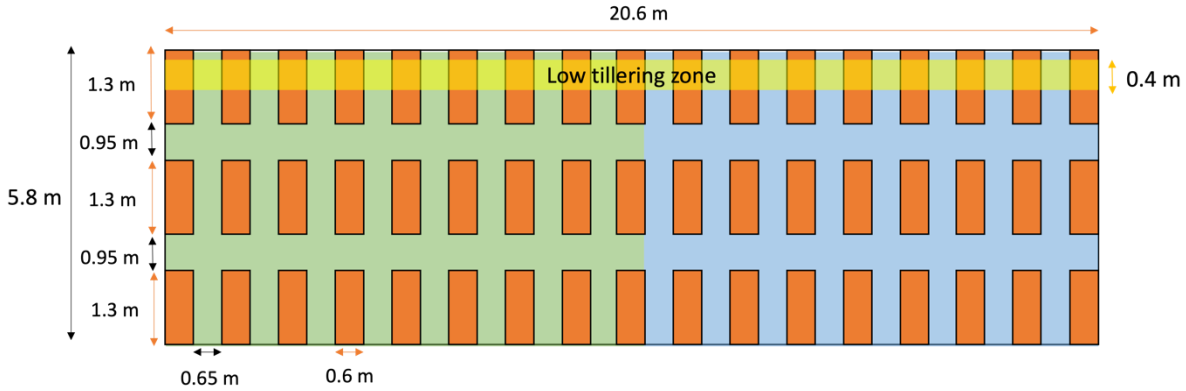

Figure 20: Delineation of the subplots as used for the tephra treatment. The yellow zones correspond to zones damaged by the tractor during fertilization, and which induced low tillering. The green area corresponds to the zone dedicated to the early stem extension stage. The blue area corresponds to the zone dedicated to the late stem extension stage.

Tephra application

The tephra was applied to wheat plants using an in-house built tephra spreader specifically designed for this type of experimentation (Figure 21). It is made of a rolling salt spreader (Western WB-160D) modified to hold a container of tephra (100x40x60 cm) and placed on a 7 m long rail with an adjustable height. The tephra particles emerge from the bottom of the box through 20 small openings when the device is set in motion. The box has an opening width of 75 centimetres, its height (maximum 2.5 m) and length (maximum 7 m) are adjustable. The length was set to 1.3 m, corresponding to the length of subplots, and the height was set to 1.3 m. For the second application to plants at the late stem extension stage, it was necessary to account for same height difference between the spreader and the top of the plants. To avoid contamination on the neighbouring subplots during tephra spreading, disposable tarpaulins were placed on the sides of the spreader. Tests were carried out before the

experimentation to make sure the deposit of tephra was homogeneous on the ground (Table A-3).

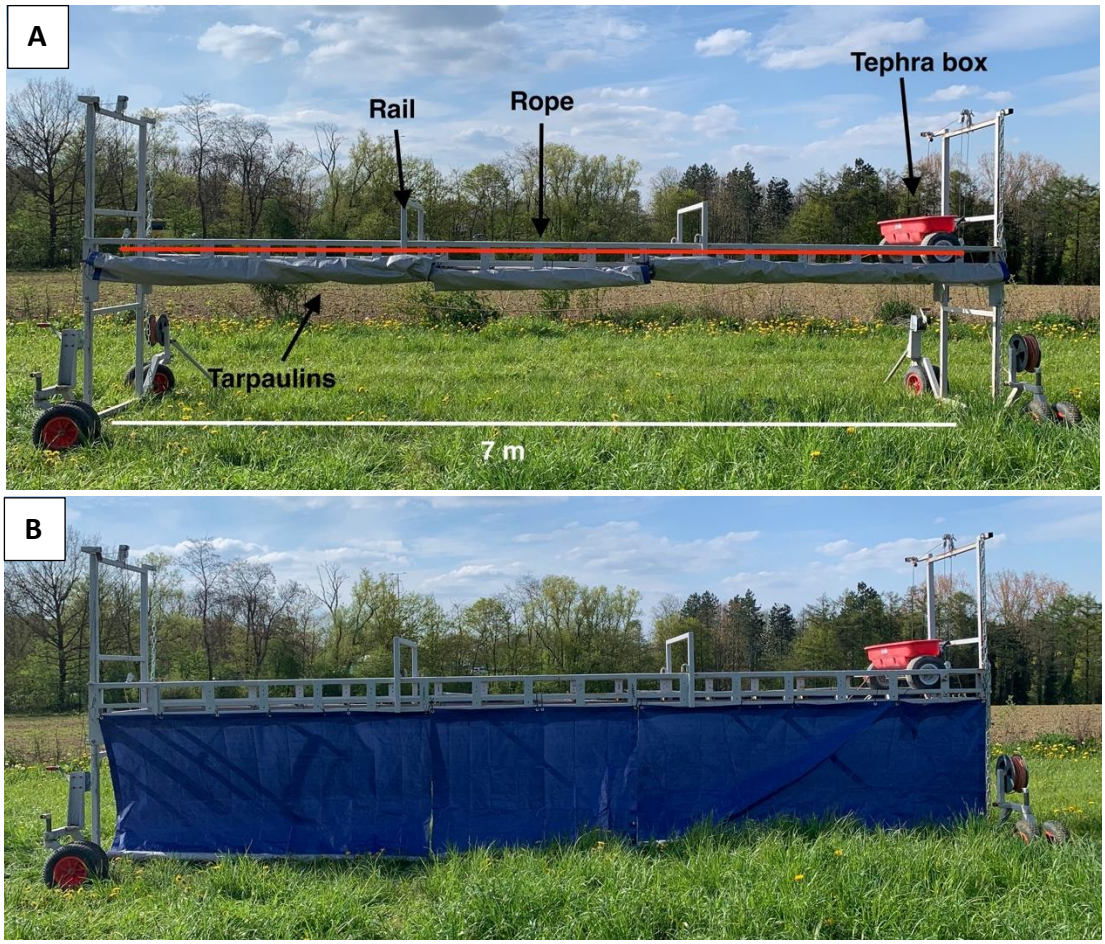

Figure 21: Photos of the in-house tephra spreader used to apply tephra to winter wheat, with the tarpaulins folded (A) and unfolded (B). The tephra spreader consists of a tephra box installed on a 7 m long rail. The spreader is pulled manually with the rope, allowing tephra particles to exit the device through 20 holes located at the bottom of the tephra box.

4.2.4 Image acquisition

The spectral information was collected by a MicaSense RedEdge-M multispectral camera. It is a skilled multispectral camera capable of recording five distinct spectral bands simultaneously (blue, green, red, NIR, red edge) in order to produce precise and numerical data on the vitality and health of crops (MicaSense, 2017). The camera is mounted on a unmanned aerial vehicle (UAV), the DJI "Martice 300 RTK" drone (Figure 22; DJI, 2023).

Figure 22: MicaSense RedEdge-M multispectral camera, with the five imagers recording the different spectral bands (A). Source: MicaSense, 2017. Drone DJI "Martice 300 RTK" with the MicaSense RedEdge-M mounted on it (B).

4.2.5 Experimental plan

Early and late stem extension stages were studied, which means two tephra application were done at different moments of the plant cycle. The first tephra application was done on the 29th of April, when the meteorological conditions allowed us to fly a drone. According to the Zadoks classification, Alessio wheat had reached the early stem extension stage on the first tephra application. The second application was carried out on the 20th of May at the final stage of the stem extension.

The GPS of the drone had to be calibrated with a base station using real-time kinematic positioning. The first step was to take a photo of the calibration panel with the Micasense RedEdge-M camera. Then, two UAV acquisitions were performed with the camera mounted on the drone, before tephra spraying. The flight plan was gridded as shown in Figure 23. The drone flew at 30 meters above the ground to obtain a resolution on the ground of two centimetres. The camera was programmed to take one photo every two seconds with a flight speed of 2.25 m s^{-1}.

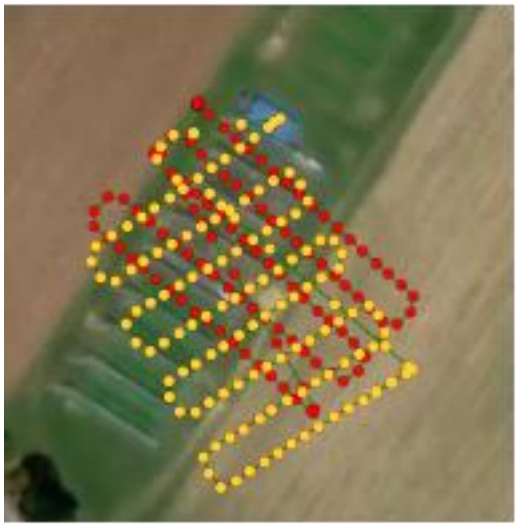

Figure 23: Flight plan of the DJI "Matrice 300 RTK" drone. Each red and yellow point represents an image acquisition by the Micasense camera. The acquisition of these two flight plans constitutes the photo bank for the experiment.

The set of flights took place under an overcast sky or a completely clear sky to avoid sudden light changes. At the end of the second flight, a second photo of the calibration panel was taken (Table 2). The second step was tephra spraying, which was carried out when wind conditions did not exceed 4 m s^{-1} and in the absence of rain. No moisture was recorded on the leaf surface of the plants during tephra spraying session. The tephra was spread on the subplots with the spreader, and the tarpaulins unfolded during the whole experiment. A second set of drone flights was then carried out with the same settings than the first ones. To allow for temporal follow-up, a third flight with the same settings was performed one day and two weeks after the tephra spreading for the early stem extension stage. For the late stem extension stage, a flight was performed one day after the tephra spraying (Table 3).

Table 2: Diary of the flight plans made throughout the experimental season over the plots at Marbaix Farm for the early stem extension stage.

Day	Steps	Hour	Cloudiness Wind speed	Days after the tephra spraying
29/04/2023	Camera calibration	11h00	Cloudy 1.4 m s^{-1}	0
	Flight one	11h00		
	Flight two	11h20		
	Camera calibration	11h40		
29/04/2023	**Tephra spreading**	12h20→16h20	Cloudy 0.6 m s^{-1}	0
29/04/2023	Camera calibration	17h00	Cloudy 1 m s^{-1}	0
	Flight one	17h00		
	Flight two	17h20		
	Camera calibration	17h40		
30/04/2023	Camera calibration	13h00	Partially clouded 1.6 m s^{-1}	1
	Flight one	13h00		
	Flight two	13h20		
	Camera calibration	13h40		
13/05/2023	Camera calibration	12h30	Partially clouded 2.3 m s^{-1}	14
	Flight one	12h30		
	Flight two	12h50		
	Camera calibration	13h10		

Table 3: Diary of the flight plans made throughout the experimental season over the plots at Marbaix Farm for the late stem extension stage.

Day	Steps	Hour	Cloudiness Wind speed	Days after the tephra spraying
20/05/2023	Camera calibration	11h00	Partially clouded 3 m s^{-1}	0
	Flight one	11h00		
	Flight two	11h20		
	Camera calibration	11h40		
20/05/2023	**Tephra spreading**	12h20→16h20	Partially clouded 2.7 m s^{-1}	0
20/05/2023	Camera calibration	17h00	Partially clouded 2.2 m s^{-1}	0
	Flight one	17h00		
	Flight two	17h20		
	Camera calibration	17h40		
21/05/2023	Camera calibration	13h00	Partially clouded 2.7 m s^{-1}	1
	Flight one	13h00		
	Flight two	13h20		
	Camera calibration	13h40		

4.2.6 Image treatment

The images collected during the flights are processed using the Pix4Dmappers software to create an orthomosaic image. This orthomosaic is the result of the compression of the photo bank acquired by the drone. The important overlap between the different photos allowed the generation of a point cloud to create the orthomosaic. Two drone flights with perpendicular directions were done to obtain a high number of overlapping photos which were necessary to acquire a gapless point cloud. After the point cloud process, the points linked to the metal structure above the plots were deleted to obtain a clear image of the studied area. After that, the orthomosaic was generated, as well as NDVI maps of the plots. The NDVI maps were then imported on ArcGIS Pro.

The orthomosaics imported on ArcGis Pro had a spatial offset between them. The ArgGIS autoreferencing tool was used to minimize this spatial shift. A series of shapefiles were manually created to delineate each subplot. Due to the heterogeneity of wheat tillering, the area studied in the subplot was restricted to the area where the NDVI is greater than or equal to 0.4 for the early stem extension stage and 0.7 for the late stem extension stage. It was considered that any pixel value under these thresholds were equivalent to bare soil. The thresholds were chosen to reflect the NDVI reached by a wheat crop at the beginning and end of the stem extension stage (Aranguren et al., 2020; Figure 24).

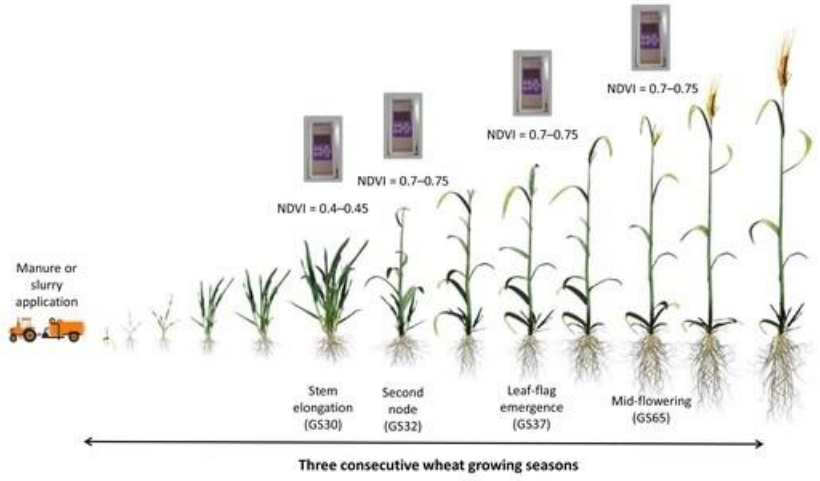

Figure 24: Evolution of NDVI through the different phenological stages of wheat. Source: Aranguren et al., 2020.

The pixels above the thresholds within each subplot are depicted in Figure 25 and Figure 26. They were used to calculate a mean NDVI with the Arcgis tool ZonalStatisticalAsTable for each subplot. All tables generated, containing mean values, were exported to a csv file which was

then processed via python. For the six repetitions of each treatment, a boxplot has been generated to allow for a comparison between the mean NDVI of each treatment.

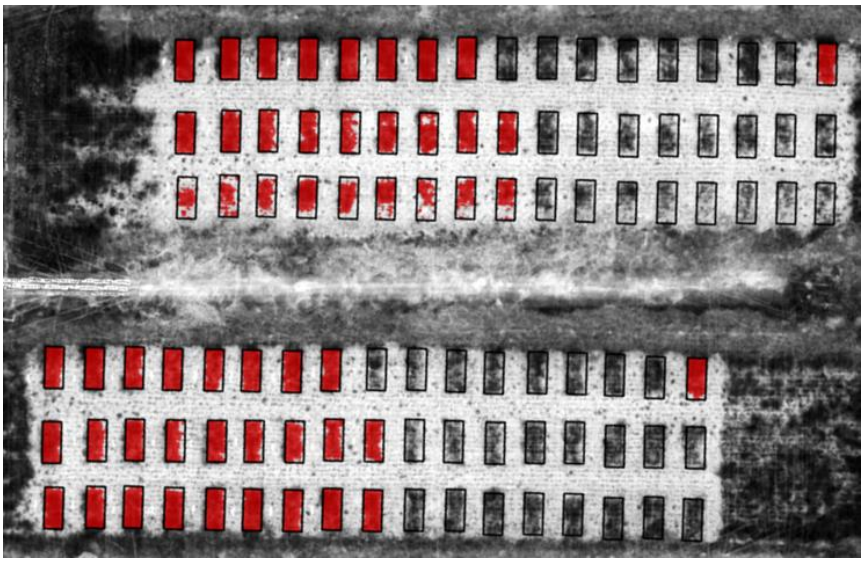

Figure 25: The red areas are the pixels selected within each subplot to calculate the mean NDVI for each treatment for the early stem extension stage. The threshold used is 0.4.

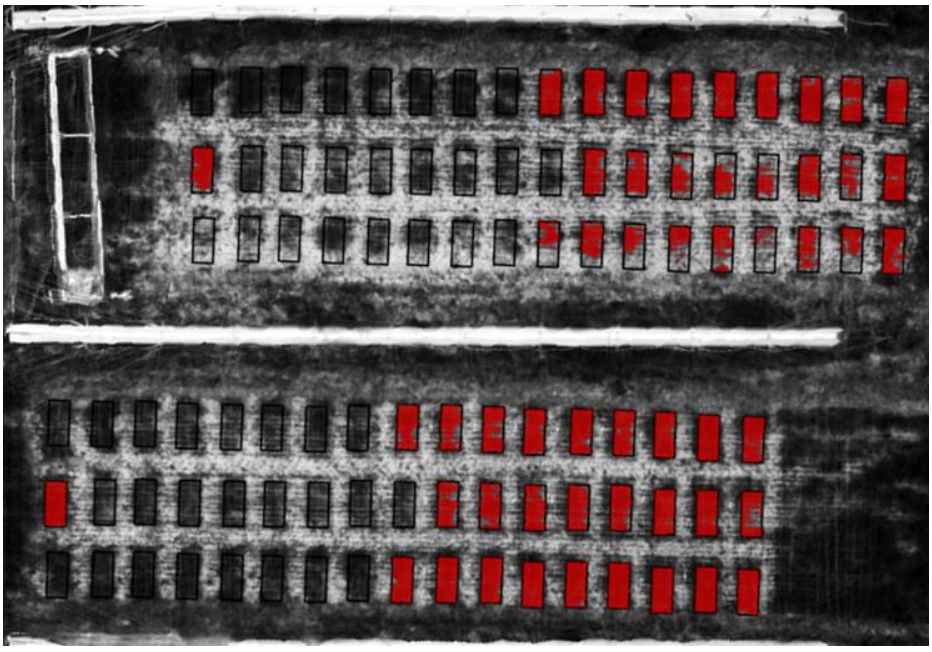

Figure 26: The red areas are the pixels selected within each subplot to calculate the mean NDVI for each treatment for the late stem extension stage. The threshold used is 0.7.

To assess which treatments were significantly different from each other, we used a Tukey's honest significance test, which retrieves a combination of letters for each treatment to evaluate their similarities. Finally, a Dunnett's test was performed to assess the difference of the NDVI over time for the different treatments.

5 Results

5.1 Spectrometric measurements of tephra

The reflectance results obtained for the tephra from Laacher See, Pinatubo and Eyjafjallajökull volcanoes according to their granulometric classes are shown in Figure 27. All the reflectance curves follow the same trend, with a variation in amplitude. The reflectance is the highest for Laacher See samples and ranges approximately between 0.12 and 0.73 (Figure 27 A), followed by Pinatubo, ranging from 0.15 to 0.57 (Figure 27 B). The lowest reflectance is recorded for Eyjafjallajökull samples with values ranging from 0.025 to 0.17 (Figure 27 C). The 95% confidence intervals for all the curves are relatively narrow, indicating that almost no variability is observed between measurements within a grain size class.

For all samples, three dips in reflectance are observed at the same wavelength values for each curve (shown as dotted lines). The largest dip is observed at 1,900 nm, while dips at 1,400 nm and 2,200 are more subdued. Between tephra specimens, these dips are distinctive by their intensity. The strongest dip in reflectance corresponds to Laacher See tephra, with a decrease of ~ 20% in reflectance at 1,900 nm compared to the reflectiveness of nearby wavelengths. For Pinatubo tephra, reflectance decrease at 1,900 nm is ~ 5% and for Eyjafjallajökull tephra, it is barely detectable.

A second observation is that usually, the reflectance seems to increase as the particle size decreases. The reflectance of Laacher See < 63 µm is significantly higher than the other grain size classes with a reflectance gap ranging between 0.2 and 0.4 higher than the other Laacher See grain size samples (Figure 27 A). The reflectance of Laacher See 0-3,000 µm is in between the curves of Laacher See <63 µm and the other grain size classes. For the Pinatubo tephra, the same observation applies, the reflectance increases when particles are smaller (Figure 27; B). Pinatubo < 63 µm and 63-125 µm have a distinctively higher reflectance (~ 0.5 and ~ 0.4 respectively) compared to 125-250, 250-500 and 500-1,000 µm grain sizes (~ 0.3 each). Similar to Laacher See and Pinatubo, Eyjafjallajökull <63 µm grain size class is significantly higher (approximately three times higher) than 63-125, 125-250, 250-500 and 500-1,000 grain size classes (Figure 27 C).

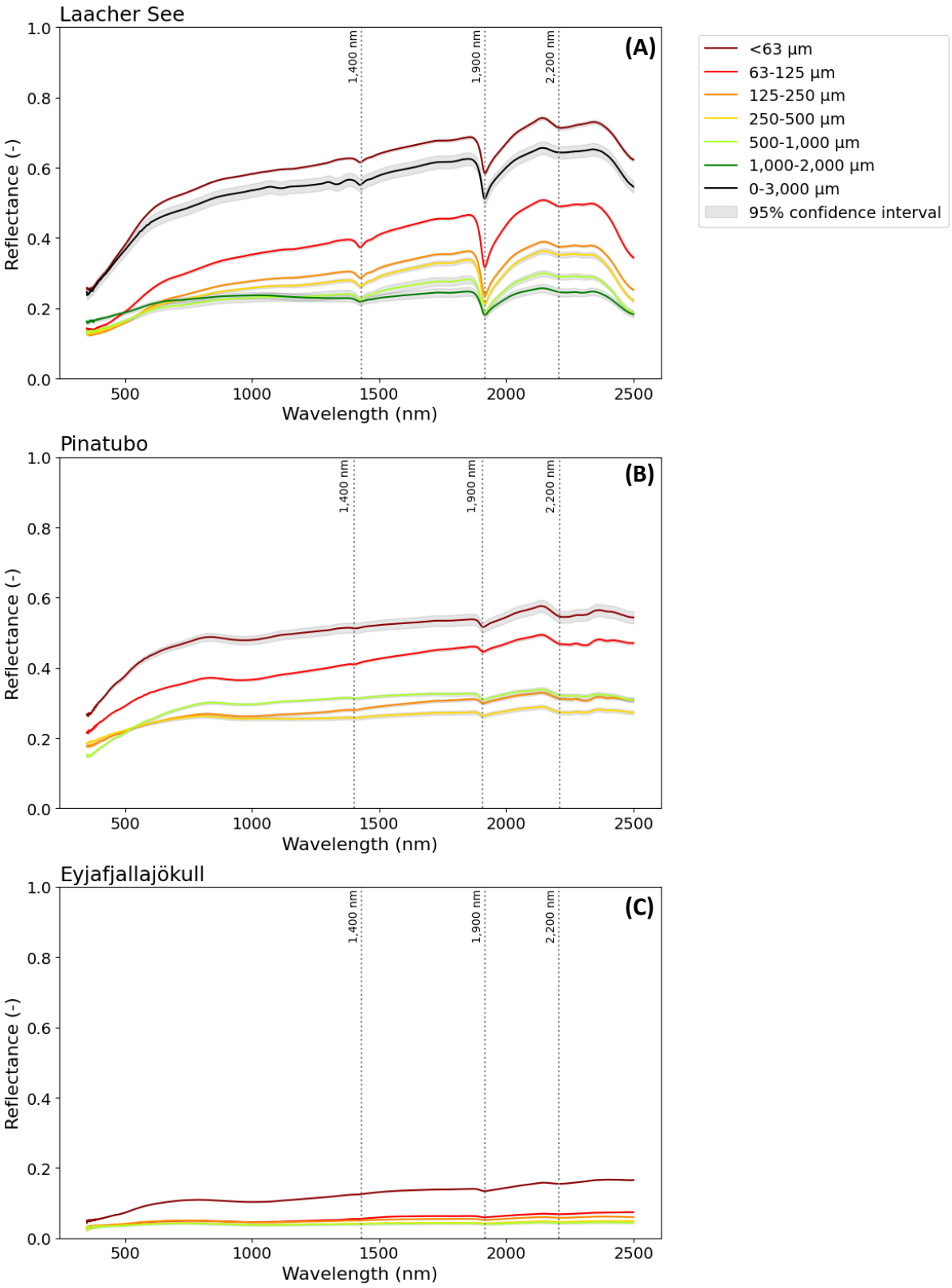

Figure 27: Tephra reflectance as a function of wavelength (VNIR) and for different grain size classes. Laacher See tephra (A) Pinatubo tephra (B) and Eyjafjallajökull tephra (C). Confidence intervals at the 95% level are also shown for each curve.

5.2 Visual assessment of tephra retention on wheat

5.2.1 Initial tephra deposit on leaves

The photos of the different treatments applied on wheat at the early stem extension stage are shown in Figure 28. Based on visual observations, the retention of tephra on leaves differs depending on grain size. Tephra particles < 63 µm formed a light visible deposit on wheat plants, while tephra particles between 125-250 µm were almost not retained by the leaves, most of the particles landed on the ground. It is particularly clear for the dark coloured tephra, Eyjafjallajökull 125-250 µm, whose soil surface had taken on a black tone after tephra spraying (Figure 28). The unsieved Laacher See tephra (0 to 3,000 µm) also displayed a visible deposit on plants. In the field, we observed that the particles retained by the plants were dominated by smaller grain size classes, similar to the < 63 µm deposits, whereas the coarser material was not retained.

Visually, for Laacher See <63 µm and 0-3,000 µm, a mass load of 500 g m^{-2} led to a more important amount of tephra particles being retained on plant leaves compared to the same tephra grain size with a mass load of 200 g m^{-2} (Figure 28). This was not observed for the grain size of 125-250 µm, as very little deposits were visible on the leaves.

Figure 29 presents the photos of the different treatments applied to wheat at the late stem extension stage. The same observations were made as for the early stem extension stage. However, it was visible that the inclination of the leaves was more vertical, and that the retention was less important than for the early stage (Figure 29). Also, the increased tephra retention on plant foliage with mass load was less pronounced than for the early stem extension stage.

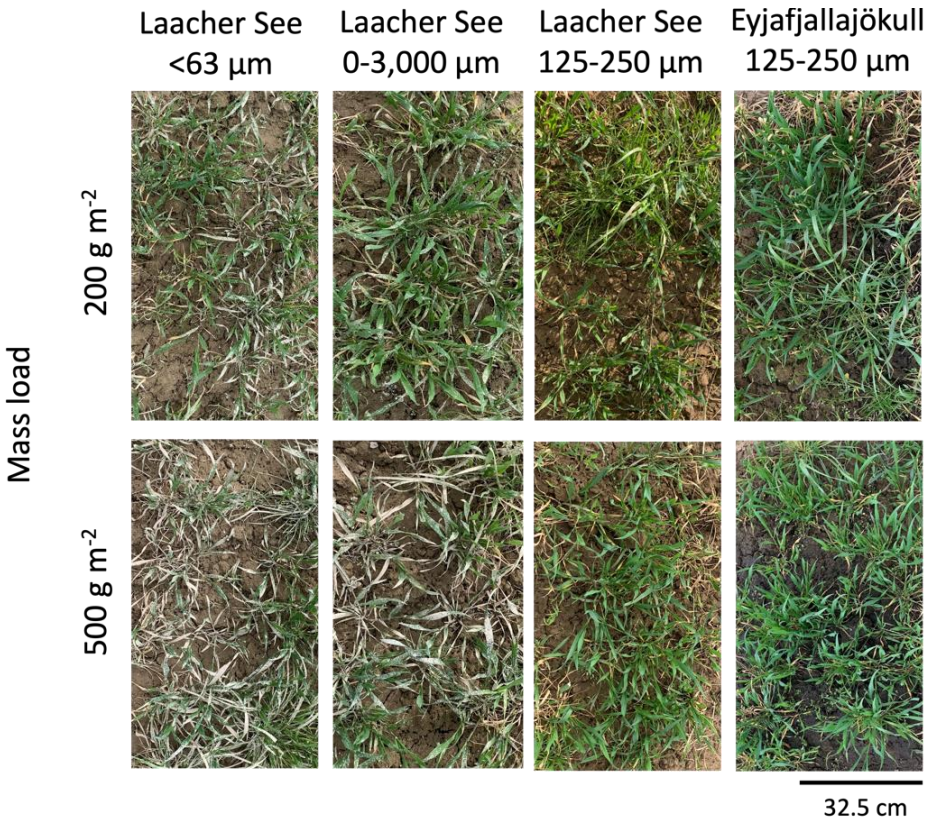

Figure 28: Photos of the different treatments applied to wheat plants right after tephra spraying (29th of April) at the early stem extension stage. The photos were taken one hour after tephra spraying.

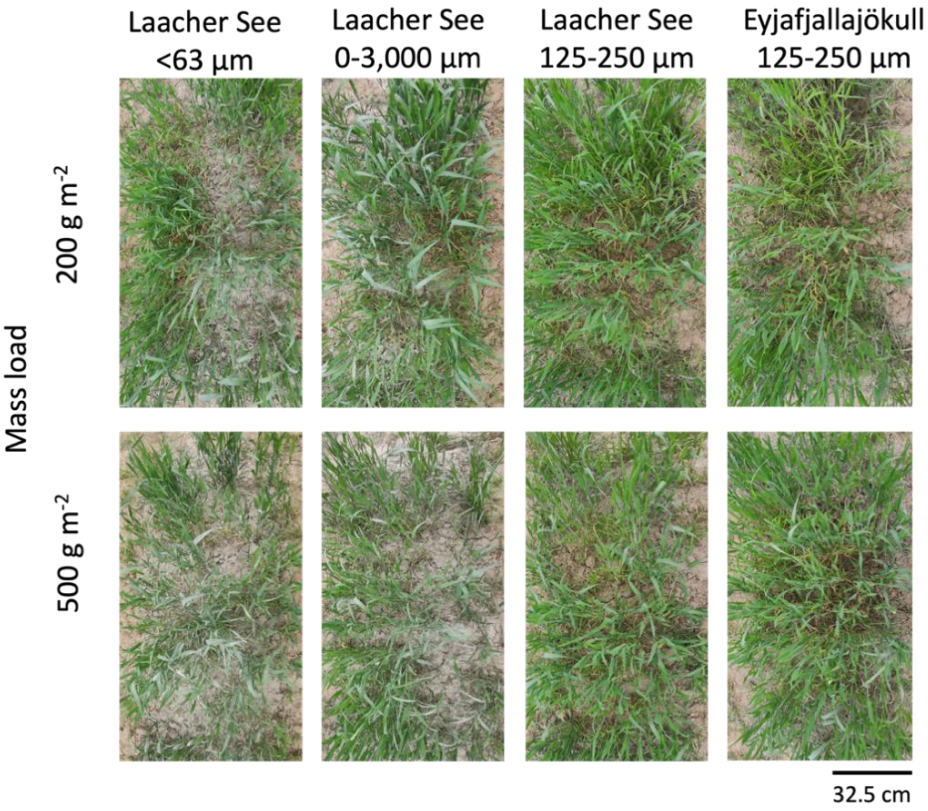

Figure 29: Photos of the different treatments applied to wheat plants immediately after tephra spraying (20th of May) at the late stem extension stage. The photos were taken one hour after the tephra spraying.

5.2.2 Temporal evolution of tephra deposit on leaves

For the early stem extension stage, the amount of tephra retained on leaves decreased with time, leaving only a thin layer on the lower leaves of the plant to which the tephra had been applied, barely perceptible 14 days after tephra spraying (Figure 30). However, these thin deposits were scarce and usually surrounded by healthy new leaves. No evolution for the treatments of Laacher See 125-250 µm and Eyjafjallajökull 125-250 µm was noticed, since little retention during spreading was observed.

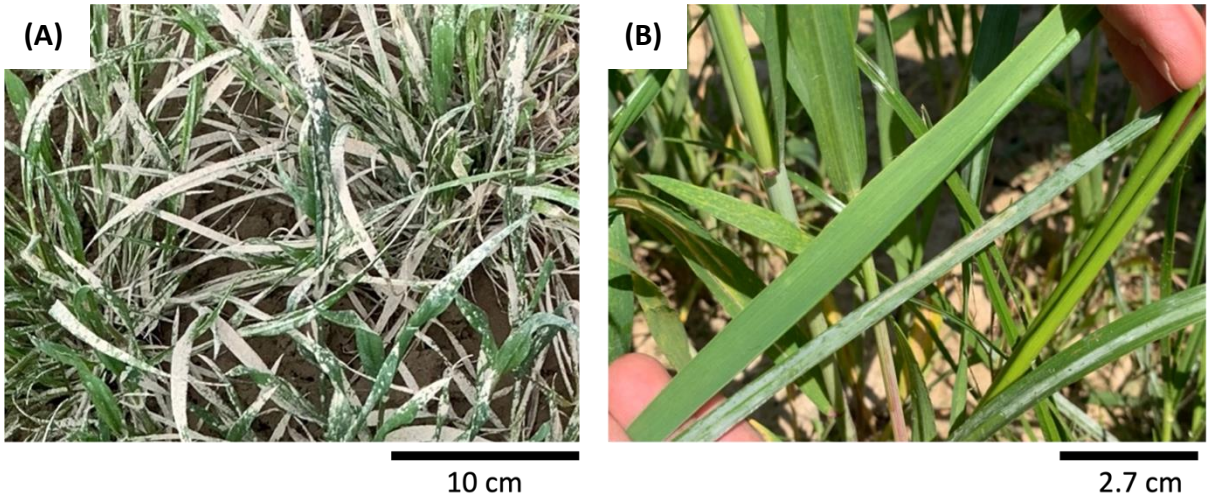

Figure 30: Comparison of tephra retention for a mass load of 500 g m^{-2} of Laacher See < 63 µm on wheat plants immediately (A) and 14 days (B) after tephra spraying at the early stem extension stage. In photo B, a clear colour difference is observed between the old leaf, showing a white deposit all over the leaf blade, and the new leaf produced after tephra spraying.

For the late stem extension stage, the retention was photographed more often to allow for a more precise evaluation of the retention than for the early stem extension stage (Figure 31). Right after tephra deposition, the leaves were mostly covered with tephra for Laacher See <63 µm and 0-3,000 µm, as mentioned in section 5.2.1. In addition, a closer observation indicated that tephra tended to land in the axil, the angular region where the leaf joins the stem and forms a sheath, as visible for the 125-250 µm grain size class (Figure 31). Four days later, a thin deposit was still present for the Laacher See <63 µm and 0-3,000 µm treatments. Most of the time the deposits were very thin. For a small proportion of these deposits, a crust was formed on the leaves, which was more or less thick depending on the initial tephra deposit. For the 125-250 µm grain size class, the tephra which had landed on the axil was still observed, but in smaller quantities. Similar observations were made seven days later.

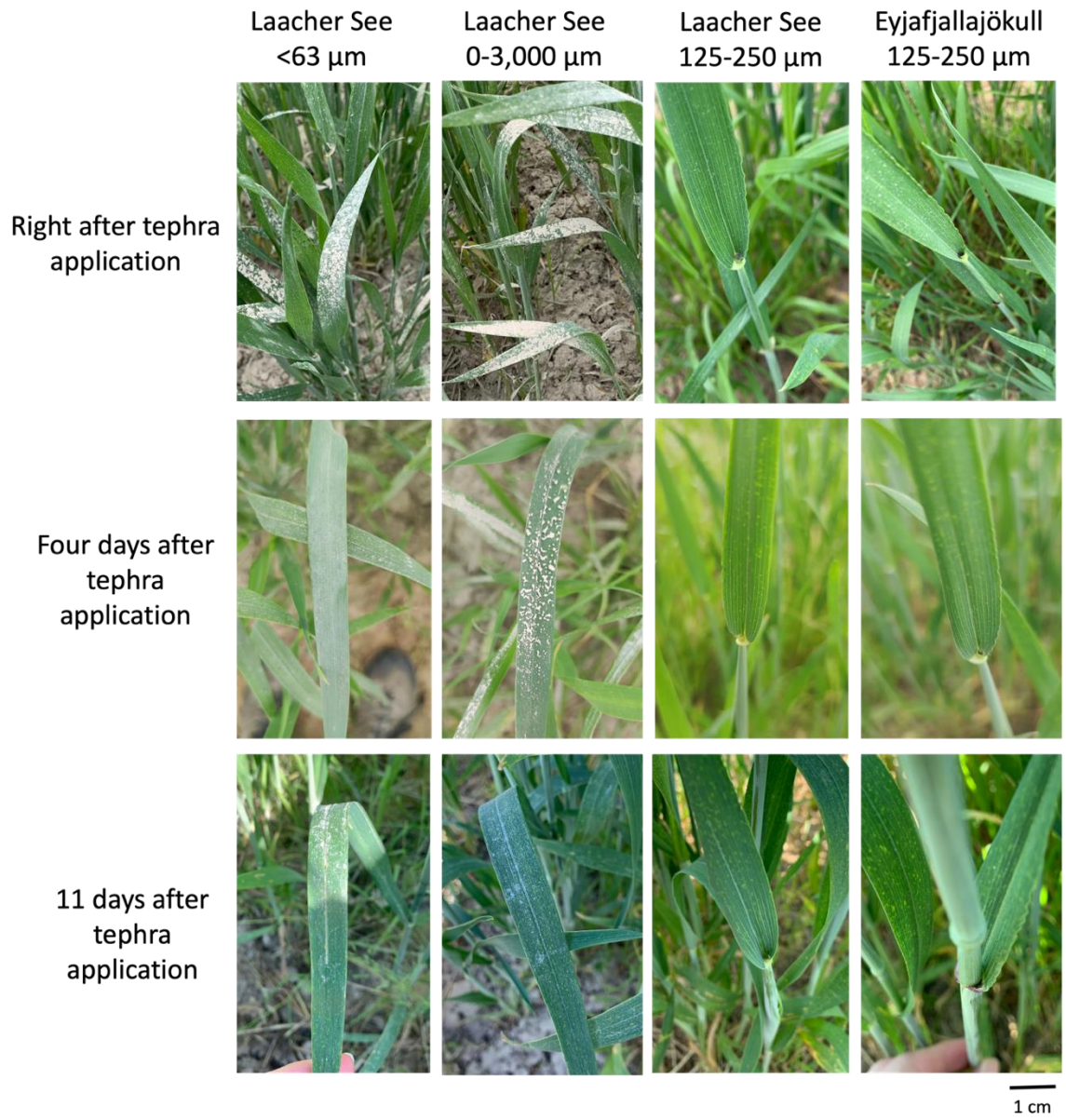

Figure 31: Comparison of tephra retention by wheat leaves after application of tephra with a mass load of 500 g m^{-2} at the late stem extension stage.

5.2.3 Weather observations

Heavy rainfall (~ 47 mm cumulated) were recorded between the 29th of April and 15th of May, corresponding to the first half of the experiment (Figure 32). The highest precipitations occurred approximately ten days after exposing wheat plants at the early stem extension stage to tephra. The second tephra application received almost no rainfall, with the exception of a very small amount (~ 0.25 mm) on the 22nd of May.

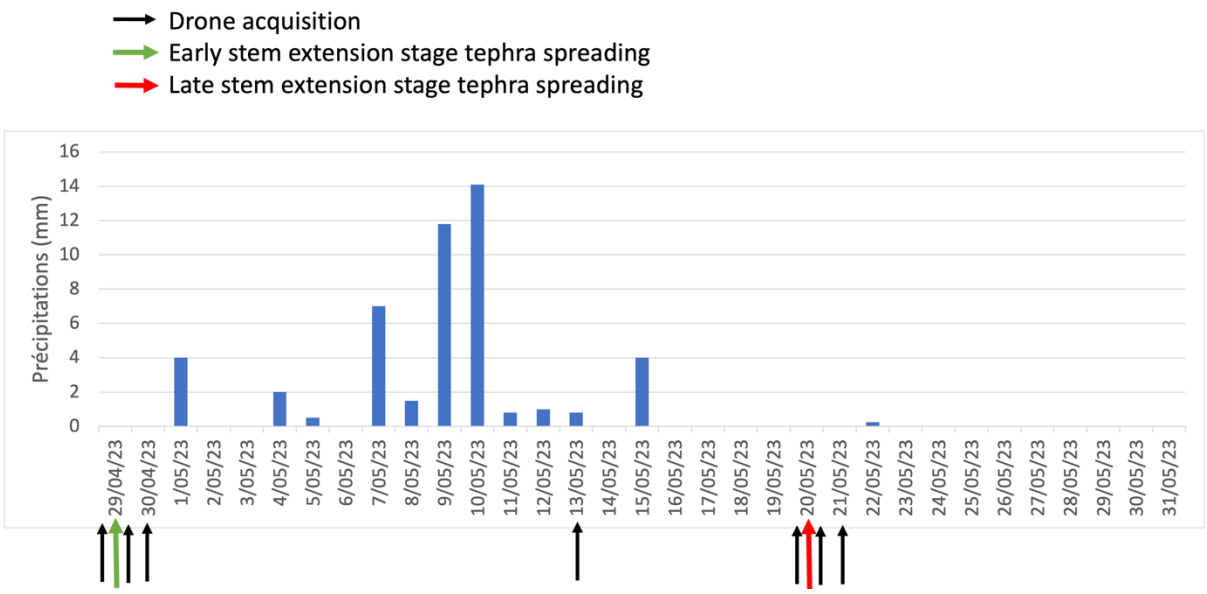

Figure 32: Precipitation (mm) recorded at Corroy-le-Grand for the experiment period. Source: meteoblue, 2023.

The wind speed recorded during the experiment shows that the wind was more regular and less strong for the first half of the period compared to the second half (Figure 33). The tephra particles present on wheat plants from the early stem extension stage were therefore only lightly exposed to wind. In contrast, during the second half of experiment, greater variations in wind speed, with steeper peaks, occurred. The maximum wind speed (4.3 m s^{-1}) was recorded on the 17th of May, three days before the application of tephra for the late stem extension stage. After that, wind speeds remained relatively high (1.6 m s^{-1} on average) until the end of the month.

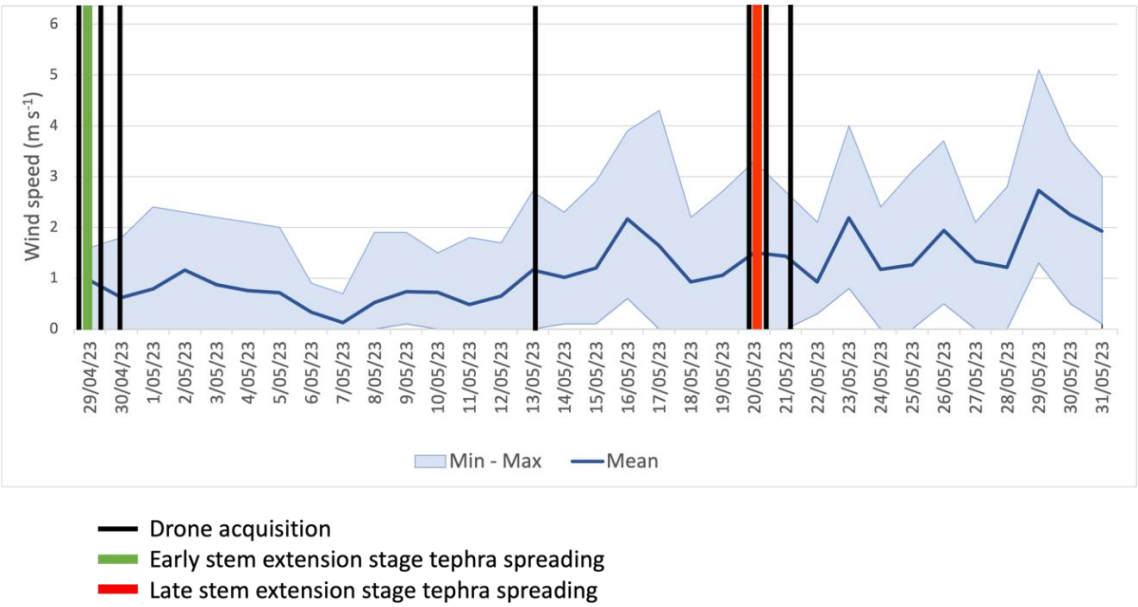

Figure 33: Wind speed (m s^{-1}) observed for the experiment period. They were recorded using a weather station (METER Em50 data logger) installed ~ 2m above the ground.

5.3 Spectral response of tephra on wheat plants

5.3.1 Comparison of the vegetation index for the different tephra treatments for the early stem extension stage

Boxplots were generated to visually represent the distribution of the mean NDVI, for each treatment (six replicates) corresponding to the early stem extension stage (Figure 34).

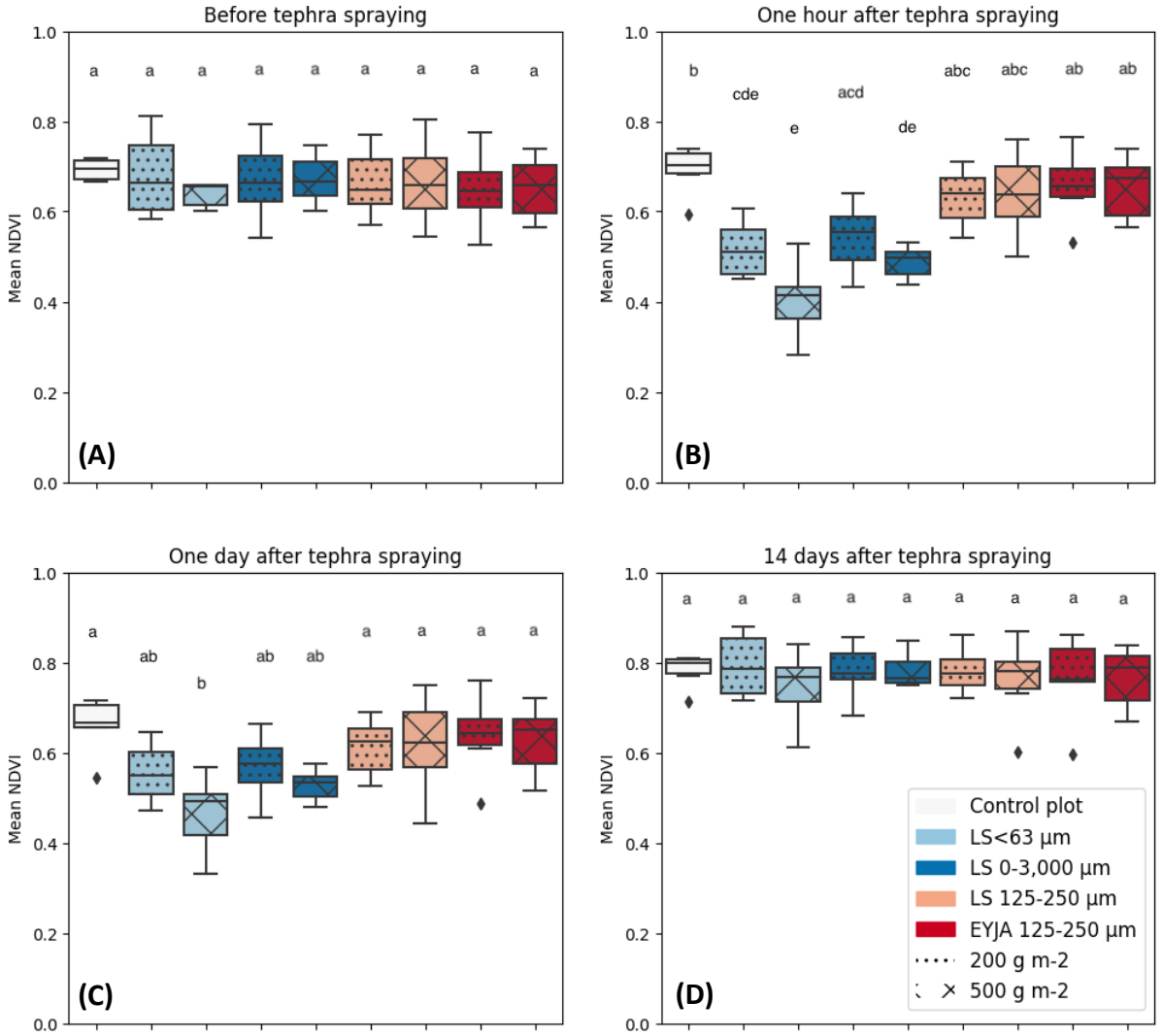

Figure 34: Boxplots of the mean NDVI for each treatment for the early stem extension stage before (A), one hour (B), one day (C), and 14 days (D) after tephra application. LS: Laacher See; EYJA: Eyjafjallajökull. The Tukey HSD (Honest Significant Difference, 95% family wise confidence level) test indicates the difference in mean NDVI as letters above each boxplot. Boxplot groups with similar letters are considered as not statistically different.

According to the Tukey's test, the wheat NDVI values, i.e. ~ 0.66, before tephra application are similar between the different treatments (Figure 34 A). The NDVI variation between the boxplot whiskers for each treatment ranges from 0.05 for the control plot, to 0.2 for LS 125-250 µm with a mass load of 500 g m^{-2}. One hour after tephra spraying (Figure 34 B), the results

of the Tukey's test indicates that the NDVI of LS < 63 µm and LS 0-3,000 µm are statistically different from the other treatments. The NDVI shows a mean reduction of ~ 0.21 compared to the NDVI value of the control plot. There is also a significant effect of the tephra mass load for LS < 63 µm and LS 0-3,000 µm, with a reduction in the mean NDVI value of ~ 0.25 for the mass load of 500 g m^{-2} compared to a reduction of ~ 0.17 for the mass load of 200 g m^{-2}. On the other hand, LS 125-250 µm and EYJA 125-250 µm are considered as similar to the control plot; thus, they will not be further described. Similar to what we observed one hour after tephra application (Figure 34 B), the mean NDVI for the LS < 63 µm and LS 0-3,000 µm treatments exhibit lower values (mean reduction of ~ 0.14) than the other treatments one day after tephra application (Figure 34 C). In contrast, to what we observed one hour after tephra application (Figure 34 B), the mass load seems to have no effect on the NDVI. Finally, 14 days after tephra application, the wheat NDVI values are similar between the different treatments, reaching a value of about 0.78 (Figure 34 D).

5.3.2 Comparison of the vegetation index for the different tephra treatments for the late stem extension stage

Figure 35 displays the NDVI results obtained for the late stem extension stage of the wheat plants. Most of the observations made for Figure 34 are applicable to Figure 35.

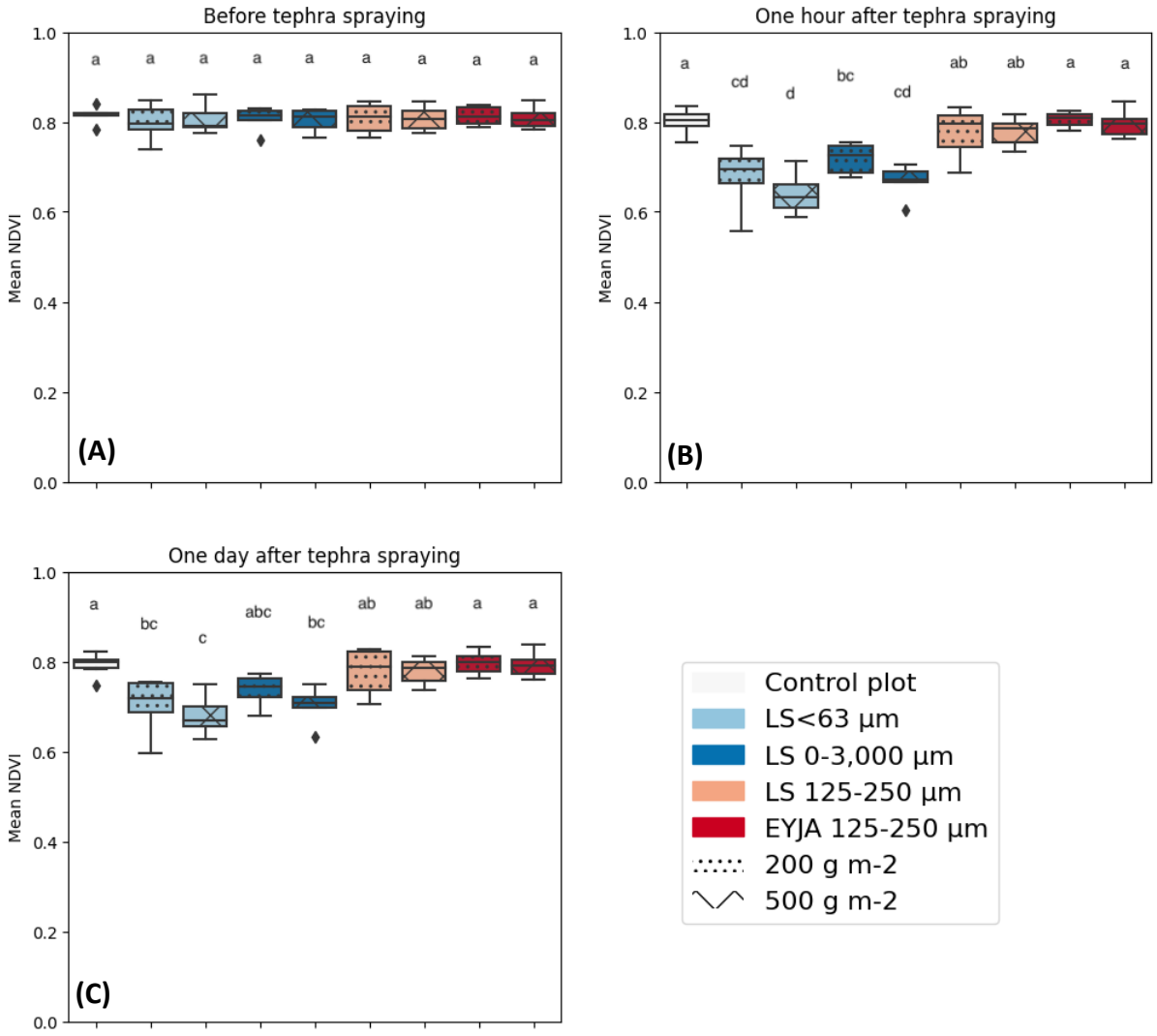

Figure 35: Boxplots of the mean NDVI for each treatment for the late stem extension stage before (A), one hour (B), and one day (C) after tephra application. LS: Laacher See; EYJA: Eyjafjallajökull. The Tukey HSD (Honest Significant Difference, 95% family wise confidence level) test indicates the difference in mean NDVI as letters above each boxplot. Boxplot groups with similar letters are considered as not statistically different.

The wheat NDVI values (~ 0.81) before tephra spraying are similar among treatments as indicated by the Tukey's test (Figure 35 A). The NDVI variations within each boxplot do not exceed 0.03. The NDVI values of LS < 63 µm and LS 0-3,000 µm measured one hour after tephra application are significantly different from the other treatments, with a mean reduction of ~ 0.12 compared to the control plot (Figure 35 B). This reduction in NDVI is statistically different than that noticed for the early stem extension stage (~ 0.21) according to Dunnett's test. Data dispersion within the boxplots varies according to treatments, from 0.03 to 0.2. We also notice a notable impact of the tephra mass load on LS < 63 µm and LS 0-3,000 µm, resulting in a decrease of ~ 0.15 in the mean NDVI value for the mass load of 500 g m^{-2} compared to a decrease of ~ 0.09 for the mass load of 200 g m^{-2}. As for the early stem extension stage, LS 125-250 µm, EYJA 125-250 µm and the control plot returned similar mean

NDVI values, thus these samples will not be further described. In line with the results one hour after the tephra application (Figure 35 B), the LS < 63 µm and LS 0-3,000 µm treatments one day after the tephra application display lower mean NDVI values (mean reduction ~ 0.09) compared to the other treatments (Figure 35 C). However, it appears that the mass load does not have any impact on the NDVI values, unlike the measurements acquired one hour after application (Figure 35 B).

5.3.3 Evolution of the vegetation index over time for the early stem extension stage

Over time, after tephra spraying, the evolution of the mean NDVI varies between treatments, depending on the tephra material used. Similar trends are observed for the early and late stem extension stage.

Regardless of the tephra mass load, the Laacher See < 63 µm and 0-3,000 µm treatments exhibit a significant decrease (ranging from 0.1 to 0.2, Figure 36 A) in wheat plant NDVI before and one hour after tephra application, according to a Dunnett's test (P-values of the T statical test <0.05; Table A-6). One day after tephra spraying, a slight increase (~ 0.029) in NDVI is observed (Figure 36 B), but it is not sufficient to be considered significant (Table A-6) compared to the NDVI values one hour after spraying. Application of the other tephra deposits, including the 125-250 µm size fraction of Laacher See and Eyjafjallajökull, did not result in any variations in NDVI over time, after one hour and one day after tephra application (Figure 36 A, Figure 36 B). Figure 36 C reveals a significant increase in NDVI (~ 0.2, P-values of the Dunnett's test < 0.05, Table A-6) for the wheat plants in all tephra treatments between one day and 14 days after tephra spraying.

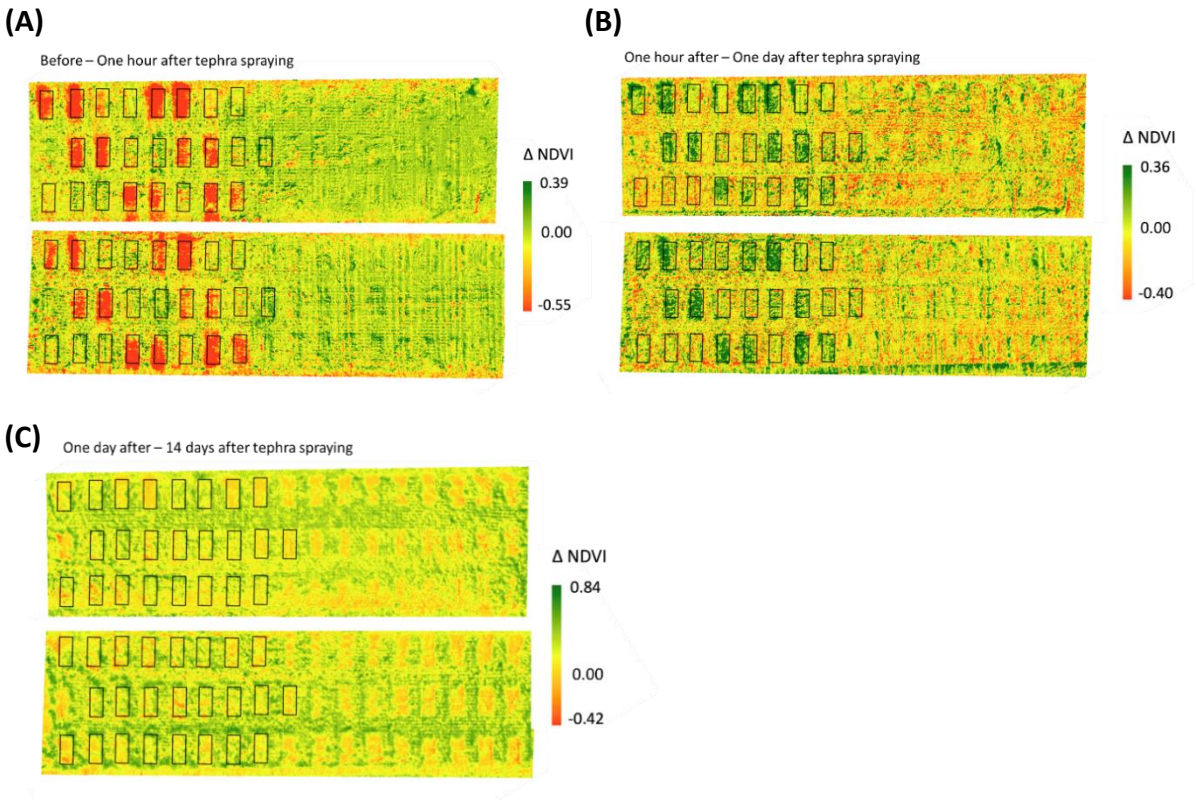

Figure 36: Difference between the NDVI maps for the early stem extension stage, before and one hour after the tephra spraying (A), one hour and one day after (B) and one day and two weeks after (C). Each subplot sprayed during the early stem extension stage is framed in black. The more the colour is red, the more the NDVI reduces. The scales of the graphs are not standardised.

5.3.4 Evolution of the vegetation index over time for the late stem extension stage

The Laacher See < 63 µm and 0-3,000 µm treatments show a decrease in NDVI ranging from 0.1 to 0.2, before and one hour after tephra application (Figure 37 A). However, only LS 0-3,000 µm with a mass load of 500 g m^{-2} exhibit a significant difference in NDVI, according to the Dunnett's test (Table A-7). Between one hour and one day after tephra spraying, a minor increase (~ 0.028) in NDVI for the Laacher See < 63 µm and 0-3,000 µm treatments is observed (Figure 36 B), which is not significant (Dunnett's test; Table A-7). As for the other treatments, Laacher See and Eyjafjallajökull 125-250 µm, no significant changes in NDVI (Table A-7) are observed one hour and one day after tephra application to the wheat plants (Figure 37 A, Figure 37 B).

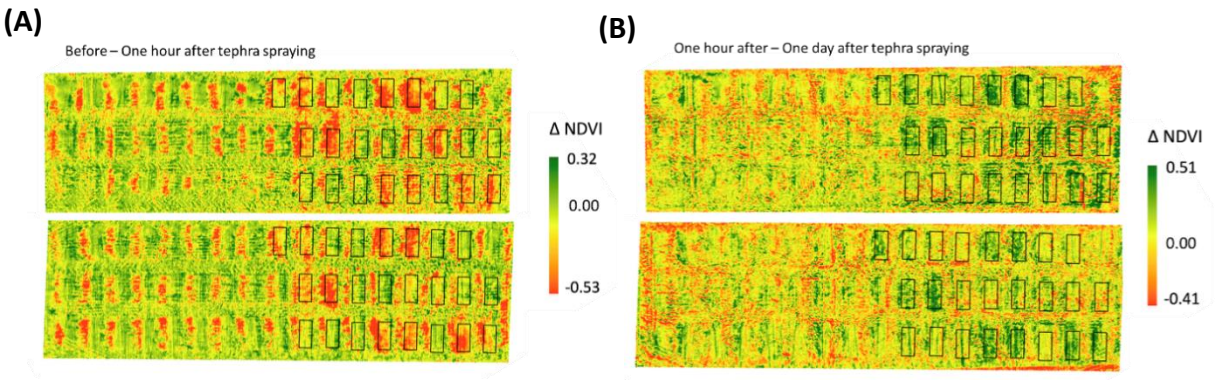

Figure 37: Difference between the NDVI maps for the late stem extension stage, before and one hour after the tephra spraying (A) and one hour and one day after (B). Each subplot sprayed during the late stem extension stage is framed in black. The more the colour is red, the more the NDVI reduces. The scales of the graphs are not standardised.

6 Discussion

6.1 Spectral properties of tephra

The reflectance curve of all the tephra samples tested follows the same pattern but the reflectance values differ between tephra (Figure 27). The Laacher See tephra shows the highest range of reflectance (0.12 to 0.73) and the Eyjafjallajökull tephra shows the smallest range of reflectance (0.025 to 0.17).

Although the two samples have roughly similar SiO_2 contents, the Eyjafjallajökull tephra contains three times more Fe and five times more Ti than the Laacher see tephra (Table 1). The presence of Fe and Ti (and implicitly Fe and Ti-containing minerals) in tephra particles is responsible for a darker colour. A dark material absorbs more light than a pale material, which has a higher albedo (Pieters, 1983). This explains the lower reflectance of the Eyjafjallajökull tephra compared to the Laacher See tephra. This result is consistent with previous studies that indicate that felsic tephra have a higher range of reflectance values than basaltic ones (Adams & Filice, 1967; Leight et al., 2022).

The overall shape of the reflectance curve is comparable for the different tephra grain size classes but with a variation in the amplitude (Figure 27). This suggests that the reflectance behaviour is consistent across the different particle sizes. The reflectance seems to increase as the particle size decreases. This trend is usually consistent across all grain size classes, indicating that smaller particles tend to exhibit higher reflectance in this wavelength range. This reflects the larger specific surface area of smaller particles, inducing more light scattering (Mustard & Glotch, 2019; Mustard & Hays, 1997). Coarser particles also display reflectance curves that are close to each other. Little or no difference in albedo is observed for particles greater than 500 µm (Adams & Filice, 1967), which explains why their reflectance are similar.

The reflectance curve for particles 0 to 3,000 µm from the Laacher See is high (~ 0.6) and close to the reflectance of Laacher See < 63 µm. The unsieved sample contains up to 74 % by volume of < 63 µm grain size particles (Figure A-6), which account for the high reflectance measured. It has been observed by Pieters (1983), that small particles (< 45 µm) dominate the interaction with light in a soil, even when present in minor quantities (< 25%).

Two main dips are present at the same wavelengths for each reflectance curve for each tephra specimens, around 1,400 and 1,900 nm (Figure 27). These dips correspond to the absorption bands of water and hydroxyl (OH^-) bonds (Clark et al., 1990). Tephra particles can adsorb water molecules (Delmelle et al., 2005), leading to the presence of molecular H_2O and OH^- group on their surface. The presence of these species explains the strong absorption measured at 1,900 and 1,400 nm. The extended dip around 2,200 nm can be associated with Si-O-H bonds in the aluminosilicate glass component of the tephra (Bartholomew et al., 1980) and/or to bonds between OH^- and Al, Fe or Mg (Bishop et al., 2013; Clark et al., 1990).

However, these dips are less important depending on the tephra specimen (Laacher See presenting the strongest one, while Eyjafjallajökull has the weakest one). This simply reflect that the molecular water and hydroxyl contents in the tephra material is not homogeneous among the tephra specimens.

The confidence intervals are relatively narrow (<0.01) for all the tephra samples measured (Figure 27). For Laacher See, the larger grain size classes (500-1,000 and 1,000-2,000) tend to have a slightly wider interval (~ 0.015). This is probably because, as the particles are coarser, a variation in the position of the particles in the sample will have a higher impact on the measured optical properties (Adams & Filice, 1967). In addition, samples with larger particles tend to have contrasted colours between the grains (Figure 14).

Both the grain size class and the chemical composition play a predominant role in the spectral response of tephra. Knowing the grain size distribution and chemical composition, including Fe, Ti and OH^-, it is possible to make a first spectral classification of tephra samples. This spectral signature is important in describing the radiative properties of tephra. High reflectance can reduce light availability under the tephra deposits (Sudhakar & Mamat, 2019), while absorption of light can cause an increase in surface temperature in addition to the decrease in light availability (Möller et al., 2016). Thus, the presence on foliage of dark tephra that absorb light efficiently may lead to an increase in leaf temperature, which can be detrimental to photosynthetic activity and plant growth.

6.2 Spectral response of tephra on wheat plants

Tephra characteristics, such as the grain size distribution, the mass load and the composition, the two phenological stages studied, and weather conditions is first discussed to evaluate their influence on tephra retention. As tephra retention directly affects the coverage of green foliage, the influence of these factors on the spectral response of wheat covered with tephra is then discussed.

6.2.1 Factors influencing tephra retention

When tephra is applied to crops, it encounters vegetation on which it can be retained before reaching the soil. The literature on the interception and retention of tephra by plants shows that various factors such as plant size and shape, leaf surface texture, developmental stage and tephra mass load influence the interception and retention phenomena. (Ayris & Delmelle, 2012; Craig, 2015; Ligot et al., 2022; Wilson et al., 2007).

Grain size effect

Figure 28 and Figure 29 indicate a strong variability in tephra retention on wheat foliage depending on tephra grain size. Laacher See <63 µm and 0-3,000 µm were the materials most retained on plants, while the grain size class of 125-250 µm almost completely fell on the

ground. The unsieved tephra of Laacher See is mostly composed of finer tephra (Figure A-6), which explains its good retention on wheat. Cook et al (1981) made a similar observation after the 1980 eruption of Mount St Helens, USA, with the tephra either being retained on the vegetation or falling to the ground or lower parts of the plant. The grain size distribution plays a predominant role in the retention of tephra on vegetation. The finer the tephra particles, the greater their retention on the leaves, as demonstrated experimentally by Ligot et al. (2022).

Even though smaller grain size classes were better retained, Figure 31 also shows that 125-250 µm grain size accumulated in the axil of the wheat. In sorghum, which belongs to the Poaceae family like wheat, 75% of the particles are retained by the axil, it is the main site of interception of particles (Witherspoon & Taylor, 1971). Large, hairy and rough leaves tend to have a better tephra retention than smooth and smaller ones (Smith & Staskawicz, 1977; Wilson et al., 2007). In the field, it was possible to observe that larger leaves had a bigger percentage of their surface covered in tephra and that the rough texture of wheat leaves induced a good particle retention.

Mass load effect

The retention of tephra depends on the mass load sprayed on plants. For finer tephra an increasing mass load usually led to a larger amount of particles being retained on wheat leaves (Figure 28 and Figure 29). The mass load applied to the crop (lettuce and cabbage plants) was observed in the study by Ligot et al. (2022), where it was estimated that the greater the mass load applied, the greater the retention on the leaves. However, the importance of the mass load for tephra retention also varies depending on the grain size applied. For coarser grain size classes, such as 125-250 µm, the retention was barely visible on the leaves surface (Figure 28 and Figure 29). As it was very little retained, it was not possible to evaluate if an important mass load induced a better retention for this coarser grain size class. Thus, the fraction of green foliage covered by tephra increases as higher tephra mass loads are applied for as long as the grain size is fine.

Phenological stage effect

Even though the leaves at the late stem extension stage were larger, they retained less tephra than the leaves at the early stage (Figure 28 and Figure 29). The inclination and rigidity of the leaf probably plays an important role in tephra retention. The more the leaf is horizontal, the more it will intercept particles (Petroff et al., 2009). It was confirmed by the comparison of the retention between the two phenological stages. The orientations of the leaves at the late stem extension stage were more vertical than the leaves at the early stem extension stage, which led to a lower retention (Figure 28 and Figure 29).

Moreover, in our experiment, wheat reached a height of 20 cm at the early stem extension stage and exhibited a higher tephra retention compared to the plants that reached 60 cm height at the late stem extension stage. According to Cutler et al. (2016), tephra retention on vegetation increases proportionally with plant heights until ~ 50 cm, beyond this height, the relationship is no longer valid. This is therefore in line with the observations made by Cutler et al. (2016).

Weather effect

For both stages, it was observed in the field that a lot of tephra particles had already been removed from the wheat leaves one day after the tephra treatment. Similarly, Witherspoon & Taylor (1971) registered a very rapid loss of particles during the first few days after particles deposition on soybean and sorghum (Figure 38). According to these authors, under similar weather conditions, the rate loss is the same for all grain size classes during the first week following the deposition.

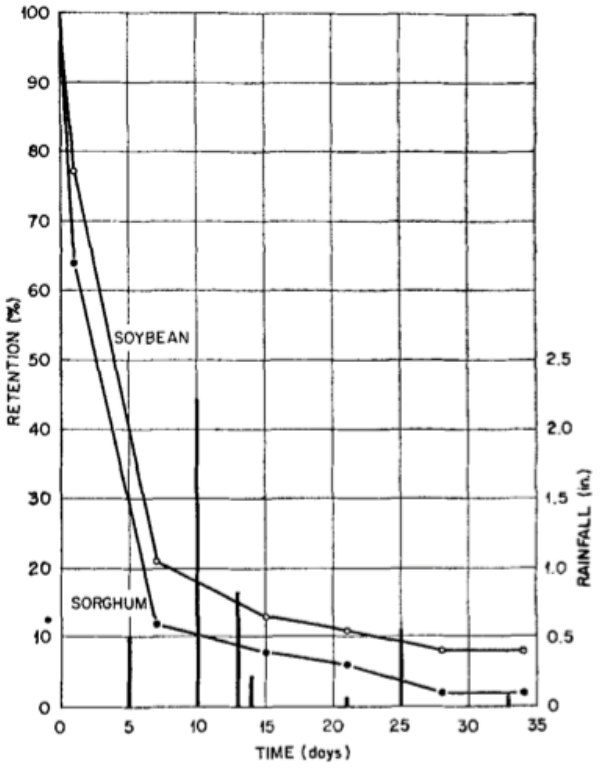

Figure 38: Percent of initial fallout interception retained on foliage and amount of rainfall up to 34 days following deposition of 1-44 µm particles. Following rapid initial loss of particles up to 7 days, loss rates are much less affected by time and amount of rainfall. Source: Witherspoon & Taylor (1971).

The weather conditions have a strong impact on tephra retention. For the early stem extension stage, between one day and 14 days after the tephra application, a large amount of rainfall was observed (Figure 32), inducing a strong loss of tephra particles from the leaves

due to water erosion. However, a very thin layer of tephra was still visible on the lower blade leaves of the plants to which the tephra had been applied (Figure 30).

The tephra particles spread during the late stem extension stage were not exposed to rain like the early stage, but they were exposed to strong winds which were recorded during the following days. Wind and water erosion are the main phenomena which remove tephra from vegetation surfaces (Ayris & Delmelle, 2012; Smith & Staskawicz, 1977). Craig et al. (2016) noted that winds can erode a tephra deposit on the leaf surface, thereby reducing the tephra mass load. However, mobilisation of tephra by wind is strongly dependent on the particle size (Dominguez et al., 2020). Smaller particles (<63 µm) have a good resistance against wind mobilisation because of their cohesive properties, which are even stronger when they are in the presence of moisture. Tephra ranging from 100 to 500 µm are the most easily remobilised by wind, unlike coarser particles (> 500 µm) that are heavier, making them difficult to transport (Cutler et al., 2021; Del Bello et al., 2021). This was observable in the field, as the small amount of 125-250 µm particles present on the leaves almost completely disappeared after a few days, whereas smaller particles < 63 µm were able to remain for a longer period of time (Figure 31).

Even though the tephra particles sprayed during the late stem extension stage were not exposed to heavy rainfalls compared to those applied during the early stem extension stage, ambient humidity also had an important impact on the retention of tephra on the plant surface. As observed in Figure 31, for the deposit of LS 0-3,000, a layer of tephra cemented itself to the leaf surface. This phenomenon is most likely due to the morning dew of the day after the tephra application. Antos & Zobel (1982) observed that cementing and crusting of a tephra deposit often occurs after humidification by rain or morning dew inducing a more severe burial of vegetation by a thin layer of tephra. In our experiment, this consolidated crust remained in place on the leaf surface for the 11 rain-free days that followed, despite the strong winds recorded (Figure 33).

According to these observations, the stability of tephra layers over time depends on many factors. Although, some processes might help the tephra to stay in place (e.g., by forming a crust over crops at an early stage), there are still other processes which might reduce the tephra layer. It appears that the half-life of particles, present on foliage, regardless of their size, is approximately 15 to 30 days, when subjected to wind and water erosion (Witherspoon & Taylor, 1971). This is coherent with field observations, as a large part of the tephra had disappeared from wheat leaves two weeks after tephra deposition.

6.2.2 Vegetation index analysis

During the experimental campaign, the growth of wheat covered with tephra was subjected to various external factors, including rain and wind. To assess the state of crop health and make comparisons between different subplots, a vegetation index was employed for continuous monitoring. Throughout the experiment, three distinct phases of NDVI evolution were observed. The initial phase encompassed the growth of wheat before tephra spraying, specifically during the early and late stem extension stages according to Zadok's growth scale (Figure 18). The second stage emerged one hour after tephra spraying. Finally, the third stage involved the recovery of the NDVI of wheat plants, observed one day and 14 days after the tephra application.

Crop monitoring before tephra application

Figure 34 A and Figure 35 A indicate that the mean NDVI values are close to 0.66 for each treatment before tephra spraying. Variations of NDVI within each treatment range from 0.5 to 0.8 for the early stem extension stage, and from 0.7 to 0.85 for the late stem extension stage. These variations might be due to the heterogeneity in wheat growth between the rows of the plots, resulting from the passage of the tractor (Figure 20). A one-way ANOVA and a Tukey's test were performed for each growth stage in order to assess if the different rows of both plots were responsible for the NDVI variability observed within each tephra treatment. The results of the ANOVA confirmed that the variance in NDVI is explained by the heterogeneity between the rows (with a p-value of the F statistic of 8.92e-13 for the early stem extension, and 1.99e-07 for the late stem extension). The Tukey's test (Table A-4; Table A-5) confirmed that the heterogeneity was stronger for the early stem extension stage than for the late one, which can be also seen by comparing the Figure 34 A and Figure 35 A. Vegetation indices may be more variable in the early stages, when ground cover by foliage is at its maximal extent. The higher variability of ground cover by wheat at the tillering stage compared to the visible flag leaf stage is also documented by Jimenez-Berni et al. (2018).

The NDVI values of ~ 0.66 at the early stem extension stage and ~ 0. 81 at the late stem extension stage (Figure 34 A and Figure 35 A) are close to the winter wheat NDVI values (~ 0.69 at the early stem extension stage, ~ 0.85 at the late stem extension stage) reported in a previous study (Vannoppen et al., 2020). Thus, our NDVI data indicate normal wheat growth. The canopy structure of crops has influences the reflectance inferred from remote sensing measurements (Maas, 1997). According to the NDVI values obtained by Tan et al., (2020), the canopy structure of our wheat is considered as erectophile/middle-type (i.e. leaf orientation value between 49° and 79°). This observation supports the hypothesis that the wheat was more vertical during the late stem extension stage, which led to smaller particle retention compared to the early stem extension stage (section 6.2.1 – phenological stage effect).

Crop monitoring immediately after tephra application

The data collected one hour after tephra application reveal a decrease in NDVI for the Laacher See <63 µm and 0-3,000 µm treatments (Figure 34 B and Figure 35 B). Most of the factors (grain size classes, mass load, plant's phenological stage, weather conditions) mentioned in the previous section (6.2.1) are relevant to explain the NDVI decrease due to the deposit of tephra. The more effective the retention, the more the wheat is covered, the more the changes in the spectral signal of the leaf surface. Tephra presents various reflectance values (Jones et al., 2007) depending on its colour, grain size and surface composition (section 5.1). Given the strong difference in red and infrared reflectance in a plant, the NDVI values are close to one. However, as observed in the spectral response of tephra (Figure 27), the red and infrared reflectance values are very similar, the NDVI tends to approach zero. As a result, the NDVI of a plant covered with tephra will decrease towards values tending to zero, depending on the tephra coverage on the plant.

The grain size class of tephra applied to wheat plants is an important parameter to explain tephra retention on leaves, covering more or less green foliage (section 6.2.1). Thus, grain size classes are significant to explain the variations induced in the NDVI of wheat covered with tephra. Our field measurements indicate that, for an equivalent mass load, finer tephra causes a greater reduction in NDVI immediately after tephra application compared to coarser grain size classes (Figure 34 B and Figure 35 B). Indeed, smaller grain size classes cover more efficiently the vegetation due to their higher adherence (Ligot et al., 2022; Wilson et al., 2009). The NDVI reduction is thus more pronounced for wheat plants covered with smaller grain size classes, such as Laacher See < 63 µm or Laacher See 0-3,000 µm which is mainly dominated by small particles (Figure A-6). The better retention rates of these smaller particles, resulting from their superior adherence to vegetation, allow them to cover larger areas of the plant leaves (Ligot et al., 2022). Consequently, the covered wheat is unable to produce a high spectral response because the smaller tephra blocks the reflectance properties of the underlying leaves (Ackerman & Finlay, 2019).

In the field, the mass load effect on NDVI values is only significant (P-value of the F statistic <0.05) when the tephra is well retained on the leaves. This is why Laacher-See < 63 µm and 0-3,000 µm, observed one hour after tephra application, are the only treatments presenting different NDVI values according to the tephra mass load applied (Figure 34 B and Figure 35 B). This means that the effect of the mass load on the NDVI depends on the grain size classes applied and on the phenomena responsible of the removal of tephra. To date, no study has established a direct link between the retention of the mass load applied to vegetation with the variation in NDVI. However, multiple authors established that, for fine dust particles sprayed on vegetation, an increasing mass load induce a decrease in NDVI (Figure 13; Kayet et al., 2019; Lin et al., 2021; Ma et al., 2017; Zhu et al., 2020). This corroborate the fact that

the applied tephra mass load is considered one of the main parameters influencing the impact on crops (Jenkins et al., 2015). Wilson et al. (2007) showed that the greater the mass load, the stronger the impact. Crop yield loss can still occur at low tephra mass loads (yield loss of 50 ± 36% for tephra mass loads <0.5 kg m^{-2}; Ligot et al., 2022). For tephra mass loads inferior to 10 kg m^{-2} the yield loss observed is highly variable. It might be due to other external factors (wind, rain, fertilisers, pesticides, tephra grain size, crops phenological stage) which induce a mixed effect (Ligot et al., 2023). The results obtained in this thesis nuance all these previous findings, by demonstrating that bigger mass loads induce bigger NDVI reduction only when tephra particles are well retained.

When comparing the spectral response at the early and the late stem extension stage, immediately after tephra deposit (Figure 34 B; Figure 35 B), the reduction in NDVI is less important at the late stage, for the same grain size and mass load applied. As described in the previous section, the NDVI observed indicated that the wheat plants presented an erectophile/middle-type canopy (Tan et al., 2020). The more the plants grew, the more vertical they became, resulting in a smaller amount of tephra retained on the leaves (section 6.2.1 – phenological stage effect), the less covered leaves from the late stage presented thus higher NDVI values than the early stage leaves (Figure 34 B; Figure 35 B).

Crop monitoring over time

Over time, the spectral influence of the two low mass loads studied on wheat covered with tephra (200 and 500 g m^{-2}, equivalent to approximately 0.2 and 0.5 mm i.e. considering a bulk deposit density of 1 g cm^{-3}) was only perceptible one hour after the deposit, but started to fade as the tephra was naturally removed from the wheat plants (Figure 36 B and Figure 37 B). De Schutter et al. (2015) concluded that, following the eruption of Oldoinyo Lengai in northern Tanzania, the NDVI of areas affected by low tephra mass load (deposit thickness < 3 cm) recovered over time and the size of the affected vegetation zone decreased. Furthermore, a recovery index (logarithmic regression model) was used in the periphery of the tephra-affected region and exhibits high values of recovery, three years after the eruption. This observation implies that the vegetation that recovers after being affected by a thin layer of tephra is in a healthier state than before the eruption (De Schutter et al., 2015), probably due to soil fertilisation by tephra. This suggest that the recovery of the NDVI over time is partially related to the tephra mass load applied on vegetation.

One day after tephra deposit, the NDVI already started to increase slightly compared to the NDVI captured one hour after the application. In Figure 36 B and Figure 37 B, it is possible to observe a slight recovery in the NDVI between one hour and one day after tephra application, even though no precipitations or strong winds were recorded during this period. As mentioned earlier, this recovery is primarily attributed to the rapid loss of tephra particles from the leaves (Witherspoon & Taylor, 1971; section 6.2.1 – weather effect).

The same trend is visible for longer periods of time. At the early stem extension, 14 days after the deposit of tephra, the mean NDVI reached a value around ~ 0.78 for all treatments (Figure 34 D). At this stage, the wheat plants had developed numerous new leaves. The spectral signal from the old leaves still partially covered with a slight tephra deposit (Figure 30) was therefore overshadowed by the signal coming from the new leaves (Figure 34 D). Consequently, if tephra deposition occurs during early phenological stages, regardless of the tephra properties, it will have no effect on the NDVI measured during the later phenological stages due to the development of the plant cover. A rapid revegetation lead to a NDVI recovery (De Rose et al., 2011) by the production of new leaves increasing the Leaf Area Index (Asrar et al., 1984). Before any tephra spraying, the NDVI measured correspond to ~ 0.66 (Figure 34 A), which is equivalent to a LAI of ~ 5, while 14 days later the NDVI increased to ~ 0.78 (Figure 34 D), equivalent to a LAI of ~ 7 (Figure 39; Tan et al., 2020). According to that measure, the number of leaves increased significantly, and reached its maximum value 14 days after the tephra deposits. These findings align with the observation that the NDVI will no longer be influenced by the tephra layer, due to the important emergence of new wheat leaves.

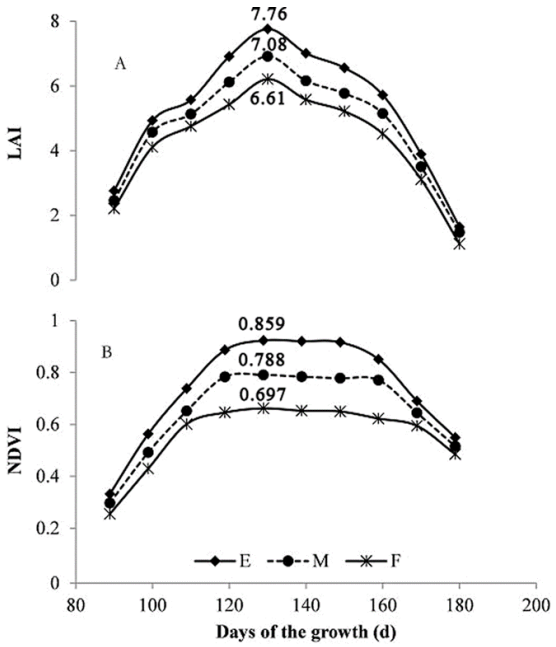

Figure 39: Dynamic curve of NDVI and LAI. E: Erectophile-type, M: Middle-type, F: Planophile-type. Source: Tan et al., 2020.

For the late stem extension stage, the initial spectral response of crops before tephra spraying showed a mean NDVI value of ~ 0.81 (Figure 35 A). Although the spectral signal 14 days after tephra deposition was not recorded, it is reasonable to assume that the NDVI did not increase significantly due to the maturity of the wheat plants. Tan et al. (2020) found that the NDVI of wheat reached a value around ~ 0.85 at maturity and remained stable until senescence started. Therefore, the presence of old leaves still covered with a thin layer of tephra, might be visible on the spectral response even after 14 days.

Over time, we suspected that the NDVI was significantly influenced by weather conditions. During the early stem extension stage, the removal of tephra a few days after the spraying, led to an increase in the NDVI, until it was no longer distinguishable from the value of the control plot (Figure 34 D). This removal is most likely due to the heavy rains reported during the following days (Figure 32), which washed away the tephra, as mentioned in section 6.2.1. Rain is known to bias the NDVI values of vegetation covered with dust, as it removes particles from the leaves (Kayet et al., 2019; Ma et al., 2017). De Schutter et al. (2015) identified an increase in NDVI of crops covered with tephra after rainy events. They incorporated a polynomial relationship between NDVI and rain into models to isolate the effect of tephra on the NDVI. This allowed them to predict the spectral evolution of vegetation following a tephra deposit (De Schutter et al., 2015). Considering washing the wheat plants after a tephra deposit of a similar mass load could be an option to mitigate the impact of tephra on crops.

6.3 Limitations and prospects

There are limitations to our experimental protocol. First, the tephra spreader may not reproduce a homogeneous dispersion comparable to that observed after a volcanic eruption, especially when thin tephra layers of 0.2 and 0.5 mm are applied. Another point to consider is that the tephra spraying period lasted at least four hours. This means that the first plots sprayed had to wait for five hours after tephra spraying before the drone flight recorded their NDVI, while the last ones only had to wait for one hour. This might have been problematic for the second tephra spraying as the wind was quite strong (2.7 m s^{-1}) and might have removed small amount of tephra from the leaves. A revision of the application protocol and/or the recording schedule may be necessary to avoid excessively long waiting times between subplots after tephra deposition.

The experiment was located in an area where drone flights cannot be operated every day as the air space is under the regulations of the military base of Beauvechain. As a result, the possibility of acquiring multispectral measurements through time was limited. Being able to do more regular flights would allow a better evaluation of the temporal spectral response of the tephra-affected-crops.

We did not have sufficient quantities of the fine fraction (< 63 µm) of the Eyjafjallajökull for comparing with the Laacher See tephra < 63 µm. Given the different spectral properties of these samples, it would be interesting to repeat the experiment in the future. The grain size class chosen for the experimentation (125-250 µm) was too coarse to observe significant differences in NDVI due to composition. Therefore, it was not possible to evaluate the effect of the composition on the spectral response of wheat covered with tephra. Redoing the experiment with a deposit made of a smaller grain size class (< 63 µm) for both compositions would most likely provide a better understanding of the tephra composition and its effect on the NDVI of crops.

This type of experiment has never been done before, this allows for various prospects, and future research.

First, conducting a thorough examination of the proportions of grain size classes retained on the leaf surface would contribute to our understanding of the various factors that influence the retention rate of the different grain size classes. Moreover, it would enhance our comprehension of the radiative interaction between a tephra particle and the leaf surface. This study could be conducted over a period of time to quantitatively assess the retention of tephra on crops after a few days. Consequently, it would be feasible to determine the half-life of a particle on leaves as a function of its grain size.

Exploring other vegetation indices would provide valuable insights into their sensitivity to specific factors such as soil albedo, leaf angle distribution, canopy optical and geometrical properties. While the NDVI was chosen as the vegetation index due to its effectiveness in detecting dust deposits on vegetation, evaluating alternative indices would help confirm its suitability or identify another index better suited to the experimental conditions. In the same way, the acquisition and the study of other wavelengths would be interesting to retrieve valuable information. Thermal images were acquired as well as the spectral images, during the data collection, but they could not be analysed due to time constraints.

The use of remote sensing to measure the NDVI or other vegetation indices could also be used in order to assess the presence of a certain thickness of tephra on vegetation. That is what has been done in other studies to measure the dust volume present on vegetation near a mining area (Kayet et al., 2019; Ma et al., 2017). This way, it would be possible to identify a tephra volume just by looking at the NDVI collected by UAVs before and immediately after the eruption, without having to go on the site.

Furthermore, satellite images can serve as an alternative to UAVs. Online availability and open-source access to satellite images, such as those from Sentinel-2, offer a cost-effective data collection method. However, there are challenges associated with satellite imagery, including limited frequency of satellite passes, typically occurring every few days, which restricts image acquisition availability. Additionally, optical satellites are weather-dependent, meaning data is only accessible when there is no cloud cover. Furthermore, satellite resolution may be inadequate in areas where crops are situated in narrow plots, making satellite imagery more suitable for open field crops.

The final purpose of this thesis was to explore the use of remote sensing to assess the impact of tephra on crops after an eruption. The data obtained enabled us to retrieve a NDVI, which could be used in further studies to calculate other biophysical variables. These variables, such

as the leaf area index, are then useful to predict the biomass of the crops and thus, the yield loss (Dong et al., 2003; Wessels et al., 2006). From there, it would be possible to describe the vulnerability of the crop studied through the yield loss measured, for a specific tephra mass load applied. The fragility function could be turned into a decision tool for the local farmers. For example, flying the drone at critical times, such as before and after heavy rains, could help the farmer make the right decision about whether to continue with the existing crop, possibly use mitigation techniques, or start a new crop.

7 Conclusion

This research was conducted on the premise that accurate and reliable risk assessments are essential for effective disaster risk management to evaluate crop yield losses due to tephra deposits. However, these assessments are based on limited data over crop vulnerability and therefore need to be improved. The objective of the master thesis was first to characterise the spectral information of different tephra samples, followed by the use of remote sensing to collect the NDVI of wheat covered with tephra. The NDVI measured are a first step for describing crop vulnerability. The use of remote sensing technologies such as UAVs is proving to be efficient in the approach to temporal monitoring of crop vegetation indices.

The study carried out on the spectral response of tephra enabled us to gain a better understanding of the properties of tephra and their interactions with light. Several parameters of tephra control their reflectance properties, such as the SiO_2 content, the grain size or the presence of specific chemical elements (H_2O, OH^-, etc).

The spectral response of a tephra-covered crop is influenced by a variety of parameters, including volcanic factors such as grain size and the mass load applied. Other non-volcanic factors, such as the phenological stage of the plant and weather conditions, particularly wind and rain, influence the retention of tephra on the leaf surfaces. The spectral response of tephra-covered crops directly relates to the efficiency of tephra retention on leaves. The presence of tephra on leaves hides the reflectance properties of the leaf. For a tephra deposit, the finer the grain size, the greater the mass load retained and the more the leaves retained the tephra, the more the vegetation index decreases. Over time, the retention of tephra on leaves tends to decrease, and the vegetation index tends to recover when the crop is exposed to meteorological hazards such as rain or wind. However, moisture can have the opposite effect, cementing tephra deposits to the leaf surface and maintaining a permanent layer of tephra. We also observed that the impact of thin tephra deposits (0.2 to 0.5 mm) on plants has little effect on NDVI when the plant is in the juvenile phenological stage. The renewal of plant material through the apparition of new leaves above the wheat cover minimises the effect of tephra deposition on the vegetation index of a plant. However, other the role of factors, such as the composition of the tephra, could not be clearly elucidated. Future work could help to assess its importance.

Thus, the NDVI is a good tool to evaluate the spectral response of wheat plants covered with tephra. The results obtained were coherent with the field observations, with an overall reduction in NDVI for the tephra deposit that were retained by the plants. The collection of NDVI using a drone could be a useful decision tool support for local farmers, to help them to decide which plan to put in place when their crops get covered with tephra after a volcanic eruption.

8 Bibliography

Ackerman, D. E., & Finlay, J. C. (2019). Road dust biases NDVI and alters edaphic properties in Alaskan arctic tundra. *Scientific Reports*, *9*(1), Article 1. https://doi.org/10.1038/s41598-018-36804-3

Adams, C. M., & Hutchinson, T. C. (1987). Comparative Abilities of Leaf Surfaces to Neutralize Acidic Raindrops. *New Phytologist*, *106*(3), 437–456. https://doi.org/10.1111/j.1469-8137.1987.tb00151.x

Adams, J. (1974). Visible and near-infrared diffuse reflectance spectra of pyroxenes as applied to remote sensing of solid objects in the solar system. *Journal of Geophysical Research*, *79*(32), 4829–4836. https://doi.org/10.1029/JB079i032p04829

Adams, J., & Filice, A. (1967). Spectral reflectance 0.4 to 2.0 microns of silicate rock powders. *J. Geophys. Res.*, *72*(22), 5705–5715. Scopus.

Adams, J., & Mccord, T. (1971). *Optical properties of mineral separates, glass, and anorthositic fragments from Apollo mare samples*. LUNAR SCIENCE CONFERENCE, HOUSTON, TX. https://ntrs.nasa.gov/citations/19710063073

Antos, J. A., & Zobel, D. B. (1982). Snowpack Modification of Volcanic Tephra Effects on Forest Understory Plants Near Mount St. Helens. *Ecology*, *63*(6), 1969. https://doi.org/10.2307/1940135

Antos, J. A., & Zobel, D. B. (2005). Plant Responses in Forests of the Tephra-Fall Zone. In V. H. Dale, F. J. Swanson, & C. M. Crisafulli (Eds.), *Ecological Responses to the 1980 Eruption of Mount St. Helens* (pp. 47–58). Springer. https://doi.org/10.1007/0-387-28150-9_4

Aranguren, M., Castellón, A., & Aizpurua, A. (2020). Wheat Yield Estimation with NDVI Values Using a Proximal Sensing Tool. *Remote Sensing*, *12*(17), Article 17. https://doi.org/10.3390/rs12172749

ASD Inc. (2010). *ASD Full Range, Portable Spectrometers & Spectroradiometers*. https://www.malvernpanalytical.com/en/products/product-range/asd-range

Asrar, G., Fuchs, M., Kanemasu, E. T., & Hatfield, J. L. (1984). Estimating Absorbed Photosynthetic Radiation and Leaf Area Index from Spectral Reflectance in Wheat [1]. *Agronomy Journal*, *76*(2), 300–306. https://doi.org/10.2134/agronj1984.00021962007600020029x

Ayris, P. M., & Delmelle, P. (2012). The immediate environmental effects of tephra emission. *Bulletin of Volcanology*, *74*(9), 1905–1936. https://doi.org/10.1007/s00445-012-0654-5

Baret, F., & Guyot, G. (1991). Potentials and limits of vegetation indices for LAI and APAR

assessment. *Remote Sensing of Environment*, *35*(2), 161–173. https://doi.org/10.1016/0034-4257(91)90009-U

Bartholomew, R. F., Butler, B. L., Hoover, H. L., & Wu, C. K. (1980). Infrared Spectra of a Water-Containing Glass. *Journal of the American Ceramic Society*, *63*(9–10), 481–485. https://doi.org/10.1111/j.1151-2916.1980.tb10748.x

Bas, M. J. L., Maitre, R. W. L., Streckeisen, A., Zanettin, B., & IUGS Subcommission on the Systematics of Igneous Rocks. (1986). A Chemical Classification of Volcanic Rocks Based on the Total Alkali-Silica Diagram. *Journal of Petrology*, *27*(3), 745–750. https://doi.org/10.1093/petrology/27.3.745

Basden, T., Abaye, A., & Taylor, R. (2023). *Chapter 5. Crop Production*.

Battude, M., Al Bitar, A., Morin, D., Cros, J., Huc, M., Marais Sicre, C., Le Dantec, V., & Demarez, V. (2016). Estimating maize biomass and yield over large areas using high spatial and temporal resolution Sentinel-2 like remote sensing data. *Remote Sensing of Environment*, *184*, 668–681. https://doi.org/10.1016/j.rse.2016.07.030

Biass, S., & Bonadonna, C. (2013). A fast GIS-based risk assessment for tephra fallout: The example of Cotopaxi volcano, Ecuador: Part I: Probabilistic hazard assessment. *Nat Hazards*, *65*, 477–495. https://doi.org/10.1007/s11069-012-0378-z

Biass, S., Bonadonna, C., Connor, L., & Connor, C. (2016). TephraProb: A Matlab package for probabilistic hazard assessments of tephra fallout. *Journal of Applied Volcanology*, *5*, 10. https://doi.org/10.1186/s13617-016-0050-5

Bishop, J. L., Rampe, E. B., Bish, D. L., Abidin, Z., Baker, L. L., Matsue, N., & Henmi, T. (2013). Spectral and Hydration Properties of Allophane and Imogolite. *Clays and Clay Minerals*, *61*(1), 57–74. https://doi.org/10.1346/CCMN.2013.0610105

Black, R. A., & Mack, R. N. (1984). Aseasonal leaf abscission in Populus induced by volcanic ash. *Oecologia*, *64*(3), 295–299. https://doi.org/10.1007/BF00379124

Blong, R. J. (1984). *Volcanic Hazards* (R. Scarpa & R. I. Tilling, Eds.). Springer. https://doi.org/10.1007/978-3-642-80087-0_20

Bonadonna, C., Connor, C. B., Houghton, B. F., Connor, L., Byrne, M., Laing, A., & Hincks, T. K. (2005). Probabilistic modeling of tephra dispersal: Hazard assessment of a multiphase rhyolitic eruption at Tarawera, New Zealand. *Journal of Geophysical Research: Solid Earth*, *110*(B3). https://doi.org/10.1029/2003JB002896

Bonadonna, C., & Costa, A. (2012). Estimating the volume of tephra deposits: A new simple strategy. *Geology*, *40*(5), 415–418. https://doi.org/10.1130/G32769.1

Bonadonna, C., Ernst, G. G. J., & Sparks, R. S. J. (1998). Thickness variations and volume estimates of tephra fall deposits: The importance of particle Reynolds number. *Journal of Volcanology and Geothermal Research*, *81*(3), 173–187. https://doi.org/10.1016/S0377-0273(98)00007-9

Brisson, N., Gary, C., Justes, E., Roche, R., Mary, B., Ripoche, D., Zimmer, D., Sierra, J., Bertuzzi, P., Burger, P., Bussière, F., Cabidoche, Y. M., Cellier, P., Debaeke, P., Gaudillère, J. P., Hénault, C., Maraux, F., Seguin, B., & Sinoquet, H. (2003). An overview of the crop model stics. *European Journal of Agronomy*, *18*(3), 309–332. https://doi.org/10.1016/S1161-0301(02)00110-7

Brown, S. K., Jenkins, S. F., Sparks, R. S. J., Odbert, H., & Auker, M. R. (2017). Volcanic fatalities database: Analysis of volcanic threat with distance and victim classification. *Journal of Applied Volcanology*, *6*(1), 15. https://doi.org/10.1186/s13617-017-0067-4

Burns, R. G. (1993). *Mineralogical Applications of Crystal Field Theory* (2nd ed.). Cambridge University Press. https://doi.org/10.1017/CBO9780511524899

Carey, S., & Sparks, R. S. J. (1986). Quantitative models of the fallout and dispersal of tephra from volcanic eruption columns. *Bulletin of Volcanology*, *48*(2), 109–125. https://doi.org/10.1007/BF01046546

Cashman, K. V., & Sparks, R. S. J. (2013). How volcanoes work: A 25 year perspective. *GSA Bulletin*, *125*(5–6), 664–690. https://doi.org/10.1130/B30720.1

Chang, C. Y., Zhou, R., Kira, O., Marri, S., Skovira, J., Gu, L., & Sun, Y. (2020). An Unmanned Aerial System (UAS) for concurrent measurements of solar-induced chlorophyll fluorescence and hyperspectral reflectance toward improving crop monitoring. *Agricultural and Forest Meteorology*, *294*, 108145. https://doi.org/10.1016/j.agrformet.2020.108145

Chlingaryan, A., Sukkarieh, S., & Whelan, B. (2018). Machine learning approaches for crop yield prediction and nitrogen status estimation in precision agriculture: A review. *Computers and Electronics in Agriculture*, *151*, 61–69. https://doi.org/10.1016/j.compag.2018.05.012

Clark, R. N., King, T. V. V., Klejwa, M., Swayze, G. A., & Vergo, N. (1990). High spectral resolution reflectance spectroscopy of minerals. *Journal of Geophysical Research: Solid Earth*, *95*(B8), 12653–12680. https://doi.org/10.1029/JB095iB08p12653

Climate-data.org. (2021). *Climat Corroy-le-Grand: Pluviométrie et Température moyenne Corroy-le-Grand, diagramme ombrothermique pour Corroy-le-Grand—Climate-Data.org*. https://fr.climate-data.org/europe/belgique/wallonie/corroy-le-grand-214487/

Cook, R. J., Barron, J. C., Papendick, R. I., & Williams, G. J. (1981). Impact on agriculture of the mount st. Helens eruptions. *Science (New York, N.Y.)*, *211*(4477), 16–22. https://doi.org/10.1126/science.211.4477.16

Cottrell, E. (2015). Global Distribution of Active Volcanoes. In *Volcanic Hazards, Risks and Disasters* (pp. 1–16). Elsevier. https://doi.org/10.1016/B978-0-12-396453-3.00001-0

Craig, H. (2015). *Agricultural vulnerability to tephra fall impacts.* [University of Canterbury]. https://ir.canterbury.ac.nz/handle/10092/13276

Craig, H., Wilson, T., Magill, C., Stewart, C., & Wild, A. (2021). Agriculture and forestry impact assessment for tephra fall hazard: Fragility function development and New Zealand scenario application. *Volcanica*, *4*, 345–367. https://doi.org/10.30909/vol.04.02.345367

Craig, H., Wilson, T., Stewart, C., Villarosa, G., Outes, V., Cronin, S., & Jenkins, S. Agricultural impact assessment and management after three widespread tephra falls in Patagonia, South America. *Natural Hazards*, *82*(2), 1167–1229. https://doi.org/10.1007/s11069-016-2240-1

Cronin, S. J., Neall, V. E., Lecointre, J. A., Hedley, M. J., & Loganathan, P. (2003). Environmental hazards of fluoride in volcanic ash: A case study from Ruapehu volcano, New Zealand. *Journal of Volcanology and Geothermal Research*, *121*(3), 271–291. https://doi.org/10.1016/S0377-0273(02)00465-1

Crown, D. A., & Pieters, C. M. (1987). Spectral properties of plagioclase and pyroxene mixtures and the interpretation of lunar soil spectra. *Icarus*, *72*(3), 492–506. https://doi.org/10.1016/0019-1035(87)90047-9

Cutler, N. A., Shears, O. M., Streeter, R. T., & Dugmore, A. J. (2016). Impact of small-scale vegetation structure on tephra layer preservation. *Scientific Reports*, *6*(1), 37260. https://doi.org/10.1038/srep37260

Cutler, N. A., Streeter, R. T., Dugmore, A. J., & Sear, E. R. (2021). How do the grain size characteristics of a tephra deposit change over time? *Bulletin of Volcanology*, *83*(7), 45. https://doi.org/10.1007/s00445-021-01469-w

Dahlgren, R. A., Saigusa, M., & Ugolini, F. C. (2004). The Nature, Properties and Management of Volcanic Soils. *Advances in Agronomy*, *82*, 113–182. https://doi.org/10.1016/S0065-2113(03)82003-5

De Rose, R. C., Oguchi, T., Morishima, W., & Collado, M. (2011). Land cover change on Mt. Pinatubo, the Philippines, monitored using ASTER VNIR. *International Journal of Remote Sensing*, *32*(24), 9279–9305. https://doi.org/10.1080/01431161.2011.554452

De Schutter, A., Kervyn, M., Canters, F., Bosshard-Stadlin, S. A., Songo, M. A. M., & Mattsson, H. B. Ash fall impact on vegetation: A remote sensing approach of the Oldoinyo Lengai 2007–08 eruption. *Journal of Applied Volcanology*, *4*(1), 15. https://doi.org/10.1186/s13617-015-0032-z

Decker, R. W., & Decker, B. B. (2023, January 8). *Volcano | Definition, Types, & Facts | Britannica*. https://www.britannica.com/science/volcano

Del Bello, E., Taddeucci, J., Merrison, J. P., Rasmussen, K. R., Andronico, D., Ricci, T., Scarlato, P., & Iversen, J. J. (2021). Field-based measurements of volcanic ash resuspension by wind. *Earth and Planetary Science Letters*, *554*, 116684. https://doi.org/10.1016/j.epsl.2020.116684

DELIVAGRI. (n.d.). *Semence de blé de force d'hiver Bio Alessio: Prix en ligne*. Retrieved 24 February 2023, from https://www.delivagri.com/semences_8/semence-de-ble-de-force-d-hiver-bio-alessio_513

Delmelle, P., Lambert, M., Dufrêne, Y., Gerin, P., & Óskarsson, N. (2007). Gas/aerosol–ash interaction in volcanic plumes: New insights from surface analyses of fine ash particles. *Earth and Planetary Science Letters*, *259*(1), 159–170. https://doi.org/10.1016/j.epsl.2007.04.052

Delmelle, P., Villiéras, F., & Pelletier, M. (2005). Surface area, porosity and water adsorption properties of fine volcanic ash particles. *Bulletin of Volcanology*, *67*(2), 160–169. https://doi.org/10.1007/s00445-004-0370-x

DJI. (2023). *MATRICE 300 RTK - Specifications—DJI*. DJI Official. https://www.dji.com/be/matrice-300/specs

Dominguez, L., Rossi, E., Mingari, L., Bonadonna, C., Forte, P., Panebianco, J. E., & Bran, D. (2020). Mass flux decay timescales of volcanic particles due to aeolian processes in the Argentinian Patagonia steppe. *Scientific Reports*, *10*(1), Article 1. https://doi.org/10.1038/s41598-020-71022-w

Dong, J., Kaufmann, R. K., Myneni, R. B., Tucker, C. J., Kauppi, P. E., Liski, J., Buermann, W., Alexeyev, V., & Hughes, M. K. (2003). Remote sensing estimates of boreal and temperate forest woody biomass: Carbon pools, sources, and sinks. *Remote Sensing of Environment*, *84*(3), 393–410. https://doi.org/10.1016/S0034-4257(02)00130-X

Dumont, B., & Sinnaeve, G. (Eds.). (2021). *Livre Blanc Céréales – Livre Blanc Céréales*. https://www.livre-blanc-cereales.be/category/livreblanc/

Eggler, W. A. (1948). Plant Communities in the Vicinity of the Volcano El Paricutin, Mexico, After Two and A Half Years of Eruption. *Ecology*, *29*(4), 415–436. https://doi.org/10.2307/1932635

Eychenne, J., Le Pennec, J.-L., Troncoso, L., Gouhier, M., & Nedelec, J.-M. (2012). Causes and consequences of bimodal grain-size distribution of tephra fall deposited during the August 2006 Tungurahua eruption (Ecuador). *Bulletin of Volcanology*, *74*(1), 187–205. https://doi.org/10.1007/s00445-011-0517-5

FAO. (2002). *BREAD WHEAT : Improvement and Production* (B. C. Curtis, S. Rajaram, & H. Gomez Macpherson, Eds.). https://www.fao.org/3/Y4011E/y4011e04.htm#bm04

FAO. (2021). *The impact of disasters and crises on agriculture and food security: 2021*. FAO. https://doi.org/10.4060/cb3673en

FAO. (2022). *Food Outlook – Biannual Report on Global Food Markets*. FAO. https://doi.org/10.4060/cc2864en

FAO. (2023). *USDA soil taxonomy | FAO SOILS PORTAL*. https://www.fao.org/soils-portal/data-hub/soil-classification/usda-soil-taxonomy/en/#c178254

Fernández, V., & Eichert, T. (2009). Uptake of Hydrophilic Solutes Through Plant Leaves: Current State of Knowledge and Perspectives of Foliar Fertilization. *Critical Reviews in Plant Sciences*, *28*, 36–68. https://doi.org/10.1080/07352680902743069

Fiantis, D., Ginting, F. I., Gusnidar, Nelson, M., & Minasny, B. (2019). Volcanic Ash, Insecurity for the People but Securing Fertile Soil for the Future. *Sustainability*, *11*(11), Article 11. https://doi.org/10.3390/su11113072

Fournier d'Albe, E. M. (1979). Objectives of volcanic monitoring and prediction. *Journal of the Geological Society*, *136*(3), 321–326. https://doi.org/10.1144/gsjgs.136.3.0321

Fowler, D. (2018). Winter Wheat Production Manual Ch 10: Growth Stages of Wheat. In *A practical guide to successful winter wheat production*.

Ghiorso, M. S., & Gualda, G. A. R. (2015). *Chemical Thermodynamics and the Study of Magmas*. 143–161. https://doi.org/10.1016/B978-0-12-385938-9.00006-7

Godfray, C., Beddington, J. R., Crute, I. R., Haddad, L., Muir, J. F., Pretty, J., Robinson, S., Thomas, S. M., & Toulmin, C. (2010). Food Security: The Challenge of Feeding 9 Billion People | Science. *Science*, *327*, 812–818. https://doi.org/DOI: 10.1126/science.1185383

Haines, B. L., Jernstedt, J. A., & Neufeld, H. S. (1985). Direct Foliar Effects of Simulated Acid Rain. *New Phytologist*, *99*(3), 407–416. https://doi.org/10.1111/j.1469-8137.1985.tb03668.x

Heiken, G. (1972). Morphology and Petrography of Volcanic Ashes. *GSA Bulletin*, *83*(7), 1961–1988. https://doi.org/10.1130/0016-7606(1972)83[1961:MAPOVA]2.0.CO;2

Henderson, M., Horgan, B., Rowe, M., Wall, K., & Scudder, N. (2021). Determining the Volcanic Eruption Style of Tephra Deposits From Infrared Spectroscopy. *Earth and Space Science*, *8*. https://doi.org/10.1029/2019EA001013

Hinckley, T., Imoto, H., Lee, K., Lacker, S., Morikawa, Y., Vogt, K., Grier, C., Keyes, M., Teskey, R., & Seymour, V. (1984). Impact of tephra deposition on growth in conifers: The year

of the eruption. *Canadian Journal of Forest Research*, *14*, 731–739. https://doi.org/10.1139/x84-130

Hinckley, T., Lachenbruch, B., Meinzer, F., & Dawson, T. (2011). A Lifespan Perspective on Integrating Structure and Function in Trees. In F. Meinzer, B. Lachenbruch, & T. Dawson (Eds.), *Size- and Age-Related Changes in Tree Structure and Function* (pp. 3–30). Springer Netherlands. https://doi.org/10.1007/978-94-007-1242-3_1

Hirano, T., Kiyota, M., & Aiga, I. (1995). Physical effects of dust on leaf physiology of cucumber and kidney bean plants. *Environmental Pollution*, *89*(3), 255–261. https://doi.org/10.1016/0269-7491(94)00075-O

Hirano, T., Kiyota, M., Seki, K., & Aiga, I. (1992). Effects of Volcanic Ashes from Mt. Unzen-Fugendake and Mt. Sakurajima on Leaf Temperature and Stomatal Conductance of Cucumber. *Journal of Agricultural Meteorology*, *48*, 139–145. https://doi.org/10.2480/agrmet.48.139

Ho, P.-G. (2009). *Geoscience and Remote Sensing*. BoD – Books on Demand.

Huang, S., Tang, L., Hupy, J. P., Wang, Y., & Shao, G. (2021). A commentary review on the use of normalized difference vegetation index (NDVI) in the era of popular remote sensing. *Journal of Forestry Research*, *32*(1), 1–6. https://doi.org/10.1007/s11676-020-01155-1

Hyll, K. (2016). *Image-based quantitative infrared analysis and microparticle characterisation for pulp and paper applications*. https://doi.org/10.13140/RG.2.1.2595.6884

Imam, E. (2019). *Remote Sensing Platforms and Sensors* (p. 27).

Irvine, T. N., & Baragar, W. R. A. (1971). A Guide to the Chemical Classification of the Common Volcanic Rocks. *Canadian Journal of Earth Sciences*, *8*(5), 523–548. https://doi.org/10.1139/e71-055

James, M. R., Carr, B., D'Arcy, F., Diefenbach, A., Dietterich, H., Fornaciai, A., Lev, E., Liu, E., Pieri, D., Rodgers, M., Smets, B., Terada, A., Aulock, F. von, Walter, T., Wood, K., & Zorn, E. (2020). Volcanological applications of unoccupied aircraft systems (UAS): Developments, strategies, and future challenges. *Volcanica*, *3*(1), Article 1. https://doi.org/10.30909/vol.03.01.67114

Jenkins, S., Biass, S., Williams, G., Hayes, J. L., Tennant, E., Yang, Q., Burgos, V., Meredith, E., Lerner, G., Syarifuddin, M., & Verolino, A. (2022). Evaluating and ranking Southeast Asia's exposure to explosive volcanic hazards. *Natural Hazards and Earth System Sciences*, *22*(4), 1233–1265. https://doi.org/10.5194/nhess-22-1233-2022

Jenkins, S., Magill, C., McAneney, J., & Blong, R. (2012). Regional ash fall hazard I: A probabilistic assessment methodology. *Bulletin of Volcanology*, *74*(7), 1699–1712. https://doi.org/10.1007/s00445-012-0627-8

Jenkins, S., Spence, R. J. S., Fonseca, J. F. B. D., Solidum, R. U., & Wilson, T. M. (2014). Volcanic risk assessment: Quantifying physical vulnerability in the built environment. *Journal of Volcanology and Geothermal Research*, *276*, 105–120. https://doi.org/10.1016/j.jvolgeores.2014.03.002

Jenkins, S., Wilson, T. M., Magill, C., Miller, V., Stewart, C., Blong, R., Marzocchi, W., Boulton, M., Bonadonna, C., & Costa, A. (2015). Volcanic ash fall hazard and risk. In C. Vye-Brown, S. Brown, S. Sparks, S. Loughlin, & S. Jenkins (Eds.), *Global Volcanic Hazards and Risk* (pp. 173–222). Cambridge University Press. https://doi.org/10.1017/CBO9781316276273.005

Jimenez-Berni, J. A., Deery, D. M., Rozas-Larraondo, P., Condon, A. (Tony) G., Rebetzke, G. J., James, R. A., Bovill, W. D., Furbank, R. T., & Sirault, X. R. R. (2018). High Throughput Determination of Plant Height, Ground Cover, and Above-Ground Biomass in Wheat with LiDAR. *Frontiers in Plant Science*, *9*. https://www.frontiersin.org/articles/10.3389/fpls.2018.00237

Jones, C. A., Kiniry, J. R. (James R., & Dyke, P. T. (1986). *CERES-Maize: A simulation model of maize growth and development*. Texas A&M University Press. https://espace.library.uq.edu.au/view/UQ:388362

Jones, M. T., Sparks, R. S. J., & Valdes, P. J. (2007). The climatic impact of supervolcanic ash blankets. *Climate Dynamics*, *29*(6), 553–564. https://doi.org/10.1007/s00382-007-0248-7

Kaufmann, R., Zhou, L., Myneni, R., Tucker, C., Slayback, D., N., S., & Pinzon, J. (2003). The effect of vegetation on surface temperature: A statistical analysis of NDVI and climate data. *Geophysical Research Letters*, *30*, 2147. https://doi.org/10.1029/2003GL018251

Kayet, N., Pathak, K., Chakrabarty, A., Kumar, S., Chowdary, V. M., Singh, C. P., Sahoo, S., & Basumatary, S. (2019). Assessment of foliar dust using Hyperion and Landsat satellite imagery for mine environmental monitoring in an open cast iron ore mining areas. *Journal of Cleaner Production*, *218*, 993–1006. https://doi.org/10.1016/j.jclepro.2019.01.305

Kennedy, R. A. (1980). Ash from Mt St Helens. *Nature*, *287*(5783), Article 5783. https://doi.org/10.1038/287581a0

Kerle, N., Janssen, L. L. F., Huurneman, G. C., Bakker, W., Grabmaier, K. A., Meer, F. D., Prakash, A., Tempfli, K., Gieske, A., Hecker, C., Parodi, G., Reeves, C. V., Weir, M., Gorte, B., Horn, J., Pohl, C., Ruitenbeek, F. J. A., & Woldai, T. (2004). *Principles of remote sensing: An introductory textbook.*

Kumar, S., Röder, M. S., Singh, R. P., Kumar, S., Chand, R., Joshi, A. K., & Kumar, U. (2016). Mapping of spot blotch disease resistance using NDVI as a substitute to visual observation in wheat (Triticum aestivum L.). *Molecular Breeding*, *36*(7), 95. https://doi.org/10.1007/s11032-

016-0515-6

Leight, C. J., McCanta, M. C., Glotch, T. D., Thomson, B. J., Ye, C., & Dyar, M. D. (2022). Characterization of tephra deposits using VNIR and MIR spectroscopy: A comprehensive terrestrial tephra spectral library. *Remote Sensing of Environment*, *273*, 112965. https://doi.org/10.1016/j.rse.2022.112965

Ligot, N. (2022). *Better quantifying crop vulnerability to tephra fall in volcanic regions: A multidisciplinary study combining field, experimental and modelling approaches*. UCLouvain.

Ligot, N., Bogaert, P., Biass, S., Lobet, G., & Delmelle, P. (2022). *Grain size modulates volcanic ash retention on crop foliage and potential yield loss*. https://doi.org/10.5194/egusphere-2022-687

Ligot, N., Guevara, A., & Delmelle, P. (2022). Drivers of crop impacts from tephra fallout: Insights from interviews with farming communities around Tungurahua volcano, Ecuador. *Volcanica*, *5*(1), Article 1. https://doi.org/10.30909/vol.05.01.163181

Ligot, N., Viera, W., Peñaherrera, D., Bernard, B., Bogaert, P., & Delmelle, P. (2023). *A quantitative assessment of crop vulnerability to tephra hazard at Tungurahua volcano, Ecuador: Understanding the effect of volcanic and biological factors*. https://doi.org/10.21203/rs.3.rs-2915673/v1

Lin, W., Yu, X., Xu, D., Sun, T., & Sun, Y. (2021). Effect of Dust Deposition on Chlorophyll Concentration Estimation in Urban Plants from Reflectance and Vegetation Indexes. *Remote Sensing*, *13*(18), Article 18. https://doi.org/10.3390/rs13183570

Liu, E. J., Cashman, K. V., & Rust, A. C. (2015). Optimising shape analysis to quantify volcanic ash morphology. *GeoResJ*, *8*, 14–30. https://doi.org/10.1016/j.grj.2015.09.001

Loughlin, S. C., Sparks, S., Brown, S. K., Jenkins, S. F., & Vye-Brown, C. (Eds.). (2015). *Global Volcanic Hazards and Risk* (1st ed.). Cambridge University Press. https://doi.org/10.1017/CBO9781316276273

Lowell, S., Shields, J. E., Thomas, M. A., & Thommes, M. (2004). *Characterization of Porous Solids and Powders: Surface Area, Pore Size and Density* (Vol. 16). Springer Netherlands. https://doi.org/10.1007/978-1-4020-2303-3

Luhr, J. F. (1992). Slab-derived fluids and partial melting in subduction zones: Insights from two contrasting Mexican volcanoes (Colima and Ceboruco). *Journal of Volcanology and Geothermal Research*, *54*(1), 1–18. https://doi.org/10.1016/0377-0273(92)90111-P

Ma, B., Pu, R., Wu, L., & Zhang, S. (2017). Vegetation Index Differencing for Estimating Foliar Dust in an Ultra-Low-Grade Magnetite Mining Area Using Landsat Imagery. *IEEE Access*, *5*, 8825–8834. https://doi.org/10.1109/ACCESS.2017.2700474

Maas, S. J. (1997). Structure and Reflectance of Irrigated Cotton Leaf Canopies. *Agronomy Journal*, *89*(1), 54–59. https://doi.org/10.2134/agronj1997.00021962008900010008x

Macedonio, G., & Costa, A. (2012). Brief Communication 'Rain effect on the load of tephra deposits'. *Natural Hazards and Earth System Sciences*, *12*(4), 1229–1233. https://doi.org/10.5194/nhess-12-1229-2012

Macedonio, G., Dobran, F., & Neri, A. (1994). Erosion processes in volcanic conduits and application to the AD 79 eruption of Vesuvius. *Earth and Planetary Science Letters*, *121*(1), 137–152. https://doi.org/10.1016/0012-821X(94)90037-X

Mack, R. N. (1981). Initial Effects of Ashfall from Mount St. Helens on Vegetation in Eastern Washington and Adjacent Idaho. *Science*, *213*(4507), 537–539. https://doi.org/10.1126/science.213.4507.537

Manville, V., Hodgson, K., Houghton, B., Keys, H., & White, J. (2000). Tephra, snow and water: Complex sedimentary responses at an active snow-capped stratovolcano, Ruapehu, New Zealand. *Bulletin of Volcanology*, *62*, 278–293. https://doi.org/10.1007/s004450000096

Maselli, F., Chiesi, M., Angeli, L., Fibbi, L., Rapi, B., Romani, M., Sabatini, F., & Battista, P. (2020). An improved NDVI-based method to predict actual evapotranspiration of irrigated grasses and crops. *Agricultural Water Management*, *233*, 106077. https://doi.org/10.1016/j.agwat.2020.106077

Mcdaniel, P., Lowe, D., Arnalds, O., & Ping, C.-L. (2012). *Andisols* (p. 33.29-33.48).

Mcguire, B. (2003). Volcano instability and lateral collapse. *Revista*, *1*, 33–45.

Medeiros, S., Fernandes, I., Fournier, B., Nunes, J. C., & Ramos, V. (2021). Hawaiian and Azorean volcanic aggregates: A preliminary study of the potential alkali-silica reaction. *Bulletin of Engineering Geology and the Environment*, *80*(12), 8949–8960. https://doi.org/10.1007/s10064-019-01702-z

meteoblue. (2023). *Archive météo Corroy-le-Grand*. meteoblue. https://www.meteoblue.com/fr/meteo/historyclimate/weatherarchive/corroy-le-grand_belgique_2800100

MicaSense. (2017). *RedEdge-M User Manual (PDF)—Legacy*. MicaSense Knowledge Base. https://support.micasense.com/hc/en-us/articles/115003537673-RedEdge-M-User-Manual-PDF-Legacy

Miller, C. F. (1967). *Operation ceniza-arena: The retention of fallout particles from volcan irazu (costa rica) by plants and people. part two*. https://apps.dtic.mil/sti/citations/AD0659384

Möller, R., Möller, M., Kukla, P. A., & Schneider, C. (2016). Impact of supraglacial deposits

of tephra from Grímsvötn volcano, Iceland, on glacier ablation. *Journal of Glaciology*, *62*(235), 933–943. https://doi.org/10.1017/jog.2016.82

Murata, K. J., Dondoli, C., & Saenz, R. (1966). The 1963–65 eruption of Irazú volcano, Costa Rica (the period of March 1963 to October 1964). *Bulletin Volcanologique*, *29*(1), 763–793. https://doi.org/10.1007/BF02597194

Mustard, J. F., & Glotch, T. D. (2019). Theory of Reflectance and Emittance Spectroscopy of Geologic Materials in the Visible and Infrared Regions. In J. L. Bishop, J. F. Bell Iii, & J. E. Moersch (Eds.), *Remote Compositional Analysis* (1st ed., pp. 21–41). Cambridge University Press. https://doi.org/10.1017/9781316888872.004

Mustard, J. F., & Hays, J. E. (1997). Effects of Hyperfine Particles on Reflectance Spectra from 0.3 to 25 μm. *Icarus*, *125*(1), 145–163. https://doi.org/10.1006/icar.1996.5583

Myneni, R. B., Hall, F. G., Sellers, P. J., & Marshak, A. L. (1995). The interpretation of spectral vegetation indexes. *IEEE Transactions on Geoscience and Remote Sensing*, *33*(2), 481–486. https://doi.org/10.1109/TGRS.1995.8746029

Nagasubramanian, K., Jones, S., Singh, A. K., Sarkar, S., Singh, A., & Ganapathysubramanian, B. (2019). Plant disease identification using explainable 3D deep learning on hyperspectral images. *Plant Methods*, *15*(1), 98. https://doi.org/10.1186/s13007-019-0479-8

Neild, J., O'Flaherty, P., Hedley, P., Underwood, R., Johnston, D., & Christenson, B. (1998). *Impact of a Volcanic Eruption on Agriculture and Forestry in New Zealand*. https://www.semanticscholar.org/paper/Impact-of-a-Volcanic-Eruption-on-Agriculture-and-in-Neild-O'Flaherty/7020fd92da6dd24c0efeb5b65a636f83f922a652

Newhall, C. G., & Punongbayan, R. S. (Eds.). (1996). *Fire and Mud: Eruptions and Lahars of Mount Pinatubo, Philippines* (Philippine Institute of Volcanology and Seismology, Vol. 18). UK: University of Washington Press. https://www.jstor.org/stable/3673980?origin=crossref

Percy, K. E., & Baker, E. A. (1988). Effects of simulated acid rain on leaf wettability, rain retention and uptake of some inorganic ions. *New Phytologist*, *108*(1), 75–82. https://doi.org/10.1111/j.1469-8137.1988.tb00206.x

Petroff, Zhang, L., Pryor, S. C., & Belot, Y. (2009). *An extended dry deposition model for aerosols onto broadleaf canopies—ScienceDirect*. *40*, 218–240. https://doi.org/10.1016/j.jaerosci.2008.11.006

Pettorelli, N., Vik, J. O., Mysterud, A., Gaillard, J.-M., Tucker, C. J., & Stenseth, N. Chr. (2005). Using the satellite-derived NDVI to assess ecological responses to environmental change. *Trends in Ecology & Evolution*, *20*(9), 503–510. https://doi.org/10.1016/j.tree.2005.05.011

Photo volcanica. (2023). *Impact of Eruption on Civilisation*. http://photovolcanica.com/VolcanoInfo/Sinabung/Sinabung.html

Pieters, C. (1983). Strength of mineral absorption features in the transmitted component of near-infrared reflected light: First results from RELAB. *Journal of Geophysical Research: Solid Earth*, *88*(B11), 9534–9544. https://doi.org/10.1029/JB088iB11p09534

Ping, C.-L. (2000). Volcanic soils. In *Encyclopedia of volcanoes* (pp. 1259–1270). H. Sigurdsson.

Porter, J. R. (1993). AFRCWHEAT2: A model of the growth and development of wheat incorporating responses to water and nitrogen. *European Journal of Agronomy*, *2*(2), 69–82. https://doi.org/10.1016/S1161-0301(14)80136-6

Rhea, M. (2022, March 18). *Igneous Rocks: Pictures, Descriptions & Identification*. Rockhound Resource. https://rockhoundresource.com/igneous-rocks-pictures-descriptions-identification/

Riley, C. M., Rose, W. I., & Bluth, G. J. S. (2003). Quantitative shape measurements of distal volcanic ash. *Journal of Geophysical Research: Solid Earth*, *108*(B10). https://doi.org/10.1029/2001JB000818

Rose, W. I., & Durant, A. J. (2009). Fine ash content of explosive eruptions. *Journal of Volcanology and Geothermal Research*, *186*(1–2), 32–39. https://doi.org/10.1016/j.jvolgeores.2009.01.010

Rosi, M., Principe, C., & Vecci, R. (1993). The 1631 Vesuvius eruption. A reconstruction based on historical and stratigraphical data. *Journal of Volcanology and Geothermal Research*, *58*, 151–182. https://doi.org/10.1016/0377-0273(93)90106-2

Samaniego, P., Le Pennec, J.-L., Robin, C., & Hidalgo, S. (2011). Petrological analysis of the pre-eruptive magmatic process prior to the 2006 explosive eruptions at Tungurahua volcano (Ecuador). *Journal of Volcanology and Geothermal Research*, *199*(1), 69–84. https://doi.org/10.1016/j.jvolgeores.2010.10.010

Schmincke, H.-U. (2004). Volcanic Hazards, Volcanic Catastrophes, and Disaster Mitigation. In H.-U. Schmincke, *Volcanism* (pp. 229–258). Springer Berlin Heidelberg. https://doi.org/10.1007/978-3-642-18952-4_13

Scholze, H. (1991). *Nature and Structure of Glass*. Springer. https://doi.org/10.1007/978-1-4613-9069-5_2

Seidel, M., Vohland, M., Greenberg, I., Ludwig, B., Ortner, M., Thiele-Bruhn, S., & Hutengs, C. (2022). Soil moisture effects on predictive VNIR and MIR modeling of soil organic carbon and clay content. *Geoderma*, *427*, 116103. https://doi.org/10.1016/j.geoderma.2022.116103

Shoji, S., Nanzyo, M., & Dahlgren, R. A. (1993). Volcanic ash soils: Genesis, properties and utilization. *Dev Soil Sci., 21,* 1–288.

Sishodia, R. P., Ray, R. L., & Singh, S. K. (2020). Applications of Remote Sensing in Precision Agriculture: A Review. *Remote Sensing*, *12*(19), Article 19. https://doi.org/10.3390/rs12193136

Small, C., & Naumann, T. (2001). The global distribution of human population and recent volcanism. *Global Environmental Change Part B: Environmental Hazards*, *3*(3), 93–109. https://doi.org/10.1016/S1464-2867(02)00002-5

Smith, W. H., & Staskawicz, B. J. (1977). Removal of atmospheric particles by leaves and twigs of urban trees: Some preliminary observations and assessment of research needs. *Environmental Management*, *1*(4), 317–330. https://doi.org/10.1007/BF01865859

Sudhakar, K., & Mamat, R. (2019). Artificial Leaves: Towards Bio-Inspired Solar Energy Converters. In *Reference Module in Earth Systems and Environmental Sciences*. Elsevier. https://doi.org/10.1016/B978-0-12-409548-9.11799-3

Tan, C.-W., Zhang, P.-P., Zhou, X.-X., Wang, Z.-X., Xu, Z.-Q., Mao, W., Li, W.-X., Huo, Z.-Y., Guo, W.-S., & Yun, F. (2020). Quantitative monitoring of leaf area index in wheat of different plant types by integrating NDVI and Beer-Lambert law. *Scientific Reports*, *10*(1), Article 1. https://doi.org/10.1038/s41598-020-57750-z

Tempfli, K., Huurneman, G. C., Bakker, W., Janssen, L. L. F., Feringa, W. F., Gieske, A., Grabmaier, K. A., Hecker, C., Horn, J., Kerle, N., Meer, F. D., Parodi, G., Pohl, C., Reeves, C. V., Ruitenbeek, F. J. A., Schetselaar, E., Weir, M., Westinga, E., & Woldai, T. (2009). *Principles of remote sensing: An introductory textbook.* (pp. 56–85).

Tian, J., & Philpot, W. D. (2015). Relationship between surface soil water content, evaporation rate, and water absorption band depths in SWIR reflectance spectra. *Remote Sensing of Environment*, *169*, 280–289. https://doi.org/10.1016/j.rse.2015.08.007

USDA. (1999). Soil taxonomy: A basic system of soil classification for making and interpreting soil surveys. *Natural Resources Conservation Service, 2nd edition*. http://www.nrcs.usda.gov/resources/guides-and-instructions/soil-taxonomy

Van den Bogaard, P., & Schmincke, H. (1984). The eruptive center of the late Quaternary Laacher See tephra. *Geologische Rundschau*, *73*(3), 933–980. https://doi.org/10.1007/BF01820883

van der Meer, F. (1999). *Imaging spectrometry for geological remote sensing | SpringerLink*. https://link.springer.com/article/10.1023/A:1003538401892

Vannoppen, A., Gobin, A., Kotova, L., Top, S., De Cruz, L., Vīksna, A., Aniskevich, S.,

Bobylev, L., Buntemeyer, L., Caluwaerts, S., De Troch, R., Gnatiuk, N., Hamdi, R., Reca Remedio, A., Sakalli, A., Van De Vyver, H., Van Schaeybroeck, B., & Termonia, P. (2020). Wheat Yield Estimation from NDVI and Regional Climate Models in Latvia. *Remote Sensing*, *12*(14), Article 14. https://doi.org/10.3390/rs12142206

Wentworth (1922) grain size classification. (n.d.). The Planetary Society. Retrieved 20 February 2023, from https://www.planetary.org/space-images/wentworth-1922-grain-size

Wessels, K. J., Prince, S. D., Zambatis, N., MacFadyen, S., Frost, P. E., & Van Zyl, D. (2006). Relationship between herbaceous biomass and 1-km2 Advanced Very High Resolution Radiometer (AVHRR) NDVI in Kruger National Park, South Africa. *International Journal of Remote Sensing*, *27*(5), 951–973. https://doi.org/10.1080/01431160500169098

Wilson, T., Cole, J., Cronin, S., Stewart, C., & Johnston, D. (2011). Impacts on agriculture following the 1991 eruption of Vulcan Hudson, Patagonia: Lessons for recovery. *Natural Hazards*, *57*(2), 185–212. https://doi.org/10.1007/s11069-010-9604-8

Wilson, T., Daly, M., & Johnston, D. M. (2009). *Review of Impacts of Volcanic Ash on Electricity Distribution Systems, Broadcasting and Communication Networks*. Auckland Regional Council.

Wilson, T., Kaye, G., Stewart, C., & Cole, J. (2007). *Impacts of the 2006 eruption of Merapi volcano, Indonesia, on agriculture and infrastructure*.

Wilson, T. M., Stewart, C., Sword-Daniels, V., Leonard, G. S., Johnston, D. M., Cole, J. W., Wardman, J., Wilson, G., & Barnard, S. T. (2012). Volcanic ash impacts on critical infrastructure. *Physics and Chemistry of the Earth, Parts A/B/C*, *45–46*, 5–23. https://doi.org/10.1016/j.pce.2011.06.006

Witherspoon, J. P., & Taylor, F. G. (1971). Retention of 1-44 μ Simulated Fallout Particles by Soybean and Sorghum Plants: *Health Physics*, *21*(5), 673–677. https://doi.org/10.1097/00004032-197111000-00008

Xue, J., & Su, B. (2017). Significant Remote Sensing Vegetation Indices: A Review of Developments and Applications. *Journal of Sensors*, *2017*, e1353691. https://doi.org/10.1155/2017/1353691

Zech, M. (2006). Evidence for Late Pleistocene climate changes from buried soils on the southern slopes of Mt. Kilimanjaro, Tanzania. *Palaeogeography, Palaeoclimatology, Palaeoecology*, *242*(3), 303–312. https://doi.org/10.1016/j.palaeo.2006.06.008

Zhu, J., Zhang, X., He, W., Yan, X., Yu, Q., Xu, C., Jiang, Q., Huang, H., & Wang, R. (2020). Response of plant reflectance spectrum to simulated dust deposition and its estimation model. *Scientific Reports*, *10*(1), Article 1. https://doi.org/10.1038/s41598-020-73006-2

Zimanowski, B., Wohletz, K., Dellino, P., & Büttner, R. (2003). The volcanic ash problem. *Journal of Volcanology and Geothermal Research*, *122*(1), 1–5. https://doi.org/10.1016/S0377-0273(02)00471-7

9 Appendices

Figure A-1: The tephra was dry sieved during 10 minutes using an AS 200 Control Retsh vibrating sieve shaker with six sieves (63; 125; 250; 500; 1,000; 2,000 µm). The amplitude was set at 1.23, the interval time at 2 seconds and the duration at 10 minutes.

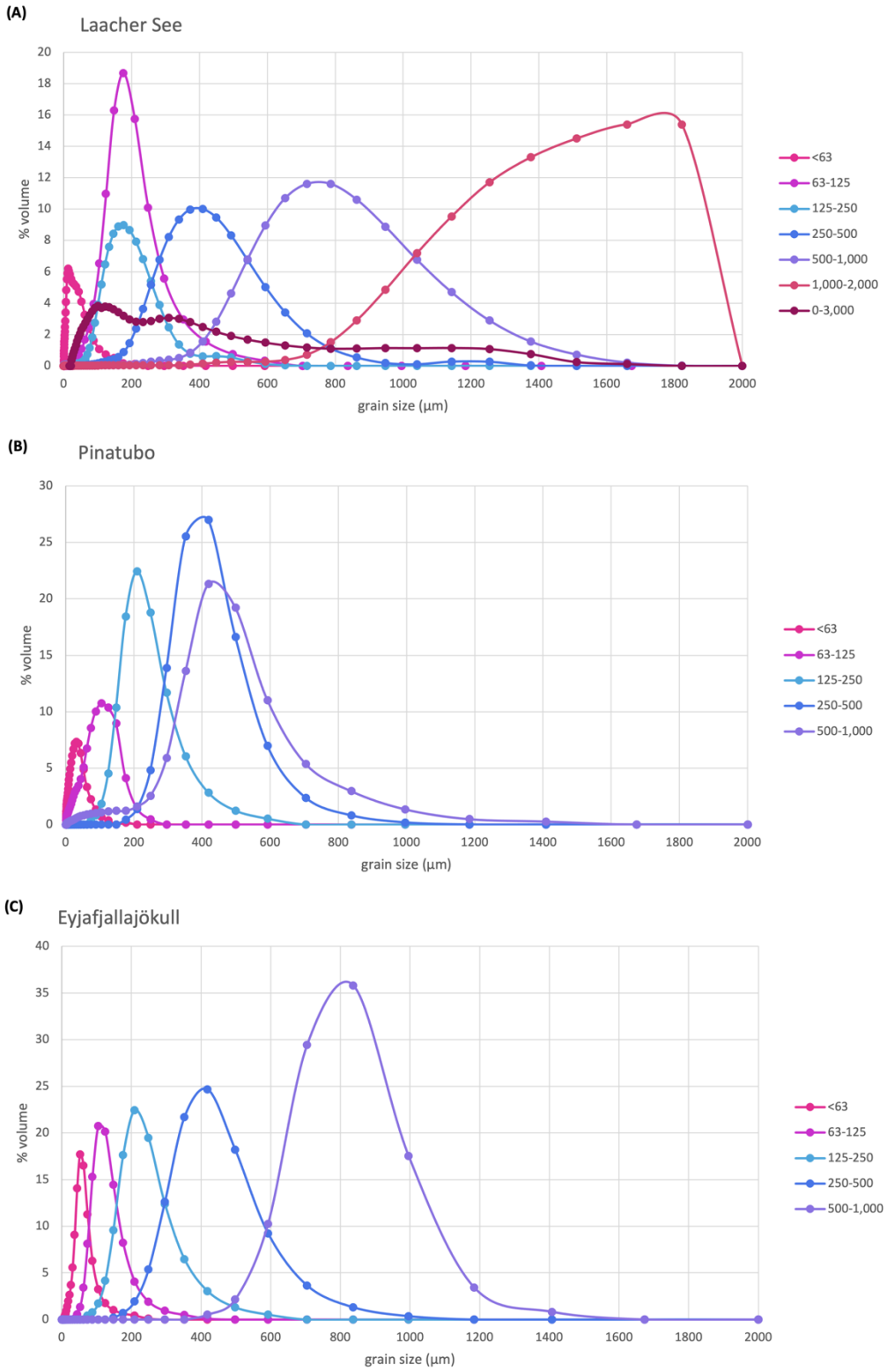

Figure A-2: Distributions of the grain size characteristics of the grain size classes (<63; 63–125; 125–250; 250–500; 500–1,000; 1,000–2,000 µm) for each tephra specimen: Laacher See (A), Pinatubo (B), Eyjafjallajökull (C).

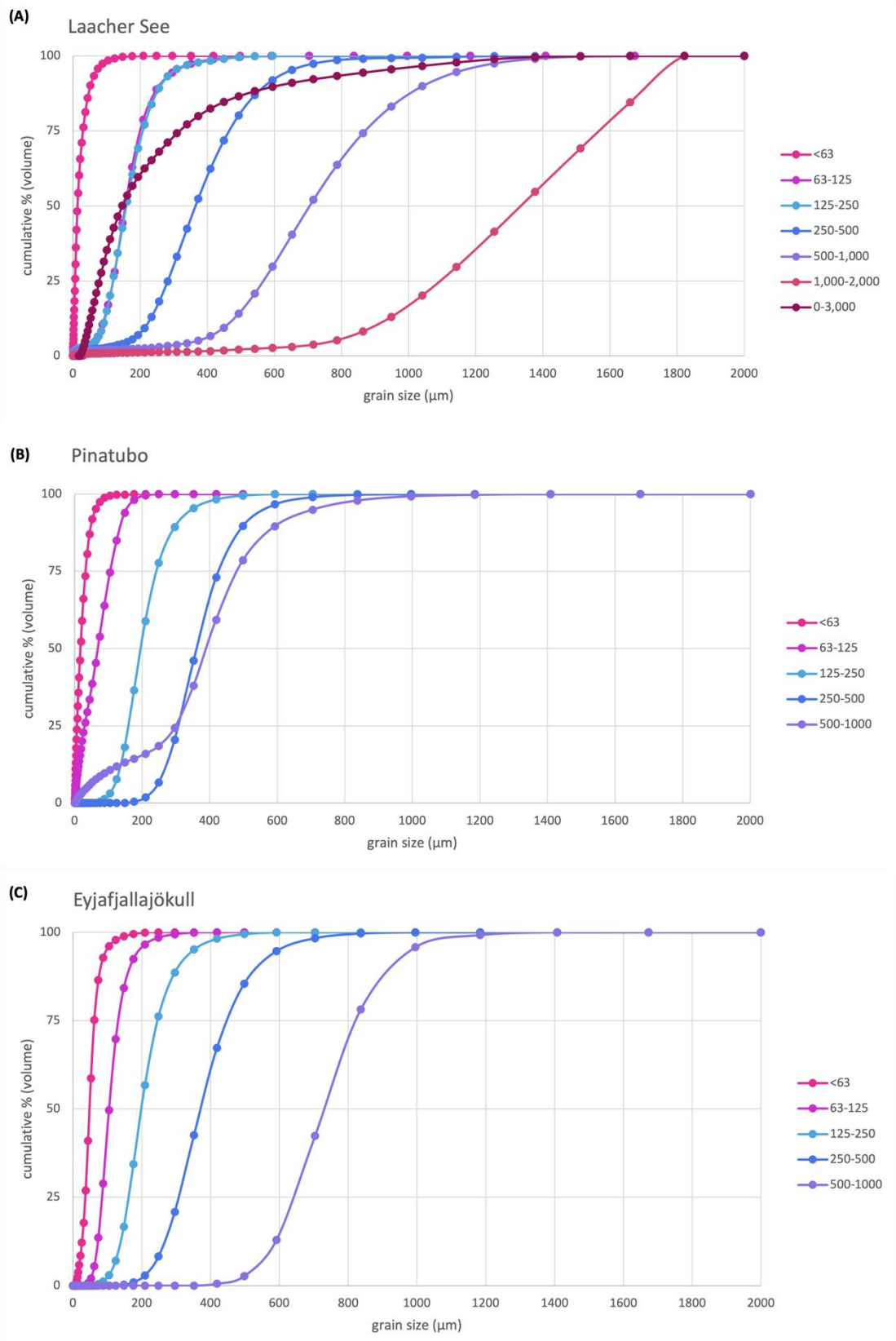

Figure A-3: Cumulative distributions of the grain size characteristics of the grain size classes (<63; 63–125; 125–250; 250–500; 500–1,000; 1,000–2,000 µm) for each tephra specimen: Laacher See (A), Pinatubo (B), Eyjafjallajökull (C).

Table A-1: Grain size analysis for the three different tephra specimens.

	Grain size classes	Mean diameter (µm)	Standard deviation (µm)	Median (µm)
Laacher See	<63	19.48	16.19	12.25
	63-125	192.033	75.21	179.83
	125-250	151.31	86.37	174
	250-500	341.51	175.16	401
	500-1,000	647.55	283.87	774
	1,000-2,000	1,168.30	399.82	1,465
	0-3,000	80.095	112.01	15.78
Pinatubo	<63	22.56	18.14	17.42
	63-125	71.24	52.96	68.72
	125-250	208.00	62.94	195.37
	250-500	374.60	89.89	360.57
	500-1,000	386.10	166.00	360.57
Eyjafjallajökull	<63	51.85	20.50	48.15
	63-125	113.23	35.52	105.033
	125-250	211.20	63.89	198.73
	250-500	386.23	104.63	370.73
	500-1,000	740.03	133.30	729.53

Table A-2: Bulk density and humidity rate of the different specimens of tephra for each grain size classes. The density was calculated by reporting the weight of the tephra in small box of 9.57 cm^3 on the volume of the box. The result was then divided by the density of water at 19°C (considered as: 0,99 g cm^3). The humidity rate was measured by weighting three samples of the same grain size class of tephra, then placing them in an oven at 80°C for 48 hours, and weight the samples a second time. The difference of weight before and after the placement in the oven enable to calculate the humidity rate.

	Grain size classes	Density (-)	Humidity rate (%)
Laacher See	<63	0.94	0.36
	63-125	1.23	0.32
	125-250	1.18	0.01
	250-500	1.17	0.23
	500-1,000	1.31	0.16
	1,000-2,000	1.32	0.25
	0-3,000	1.08	0.13
Mean	-	1.17	0.21
Sd	-	0.13	0.12
Pinatubo	<63	0.96	0.29
	63-125	1.27	0.05
	125-250	1.29	0.03
	250-500	1.31	0.00
	500-1,000	0.96	0.19
Mean	-	1.16	0.11
Sd	-	0.18	0.12
Eyjafjallajökull	<63	1.14	1.24
	63-125	1.22	0.48
	125-250	1.20	0.27
	250-500	1.12	0.19
	500-1,000	1.09	0.38
Mean	-	1.15	0.51
Sd	-	0.05	0.42

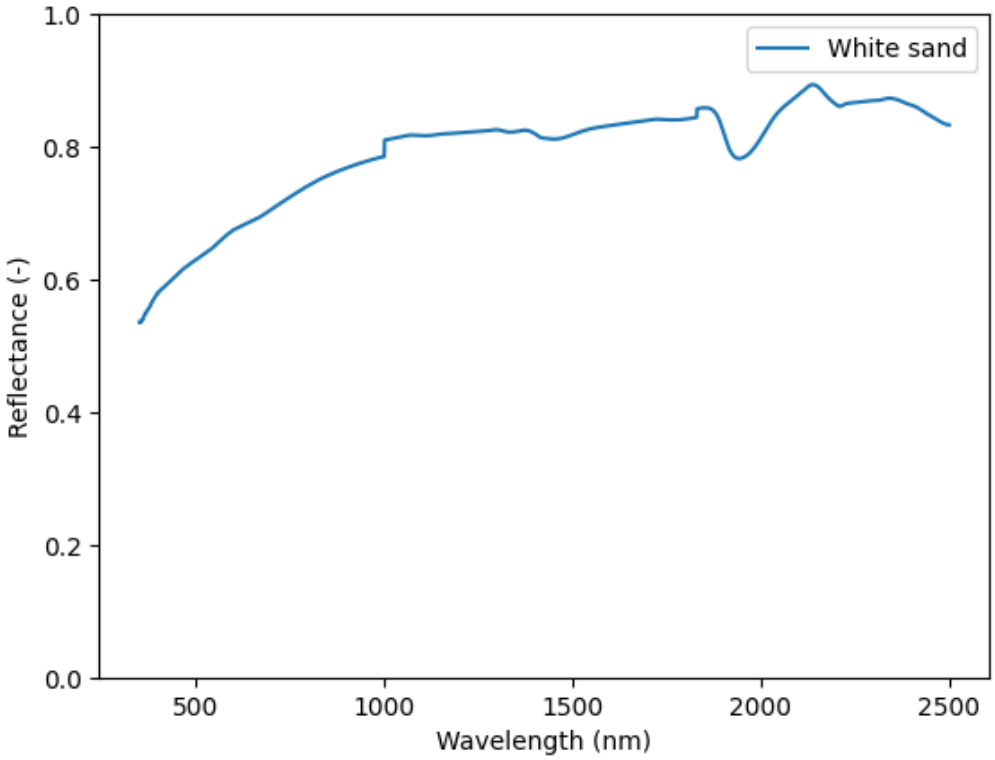

Figure A-4: Reflectance as a function of the wavelength for the average of the white sand spectrometric measurements.

First plot

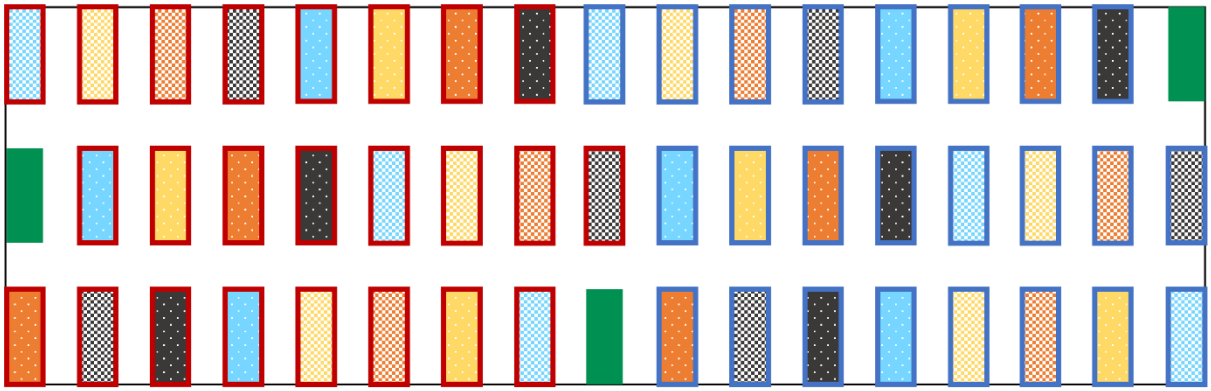

Second plot

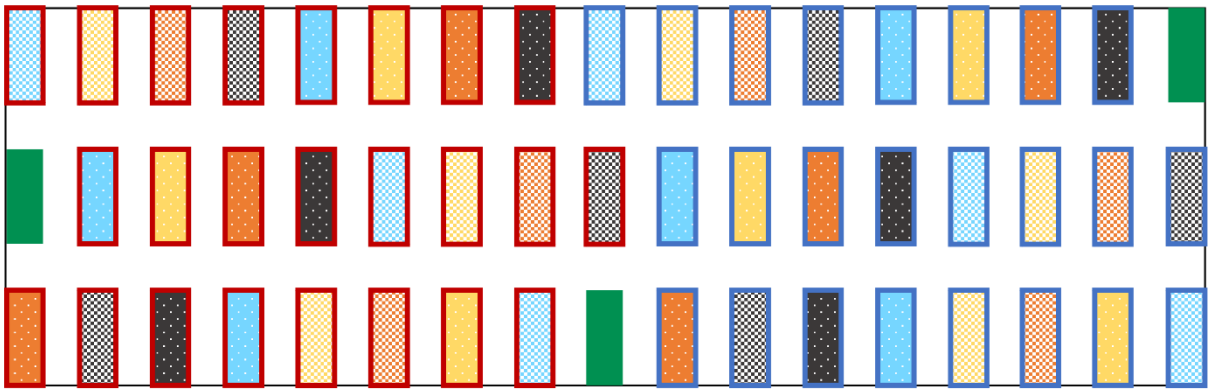

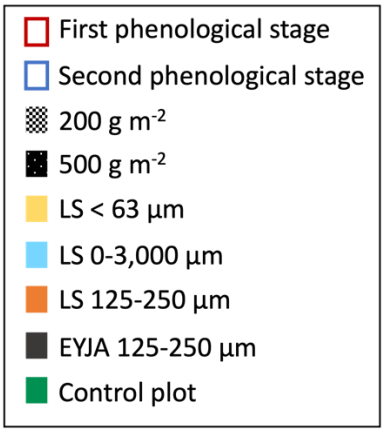

Figure A-5: Distribution of the different treatments into the subplot delineation. LS represents the tephra from de Laacher See, and EYJA from the Eyjafjallajökull.

Table A-3: Results of the test performed to assess the spatial homogeneity of the artificial tephra deposit produced with the use of the tephra spreader. Eleven plastic pots with an opening of 8.04 cm2 were placed randomly on the ground.

Pot	Tephra mass loas ($g\ m^{-2}$)
1	*30.25*
2	*21.80*
3	*25.49*
4	*21.019*
5	*23.52*
6	*32.66*
7	*9.394*
8	*16.15*
mean	*22.54*
Standard deviation	*6.57*

Table A-4: P-values of the F statistic, corresponding to the significative differences between the rows of the plots studied for the early stem extension stage. The red cells are under the 0.05 threshold confidence.

	1	2	3	4	5	6
1						
2	0,00E+00					
3	0,00E+00	4,13E-02				
4	2,53E-04	6,57E-02	6,70E-06			
5	0,00E+00	9,95E-01	1,34E-01	1,80E-02		
6	1,14E-02	2,11E-03	1,00E-07	8,01E-01	4,30E-04	

Table A-5: P-values of the F statistic, corresponding to the significative differences between the rows of the plots studied for the late stem extension stage. The red cells are under the 0.05 threshold confidence.

	1	2	3	4	5	6
1						
2	1,10E-03					
3	2,53E-05	8,45E-01				
4	1,68E-01	4,08E-01	3,82E-02			
5	4,93E-02	7,50E-01	1,36E-01	9,93E-01		
6	1,00E+00	6,34E-04	1,41E-05	1,16E-01	3,17E-02	

Table A-6: P-value of the t statistic representing the significant differences for a treatment before any tephra application and after multiple days following tephra spraying, for the early stem extension stage. The cases in blue are the treatments showing a significative difference x time after tephra spraying compared to before any tephra spraying.

	Pr(>|t|)								
Gain size (µm)	<63 (LS)		0-3,000 (LS)		125-250 (LS)		125-250 (EYJA)		Control plot
Mass load (g m^{-2})	200	500	200	500	200	500	200	500	
before - 1 hour	0.0056	0.00056	0.026	<0.0001	0.43	0.63	0.86	0.97	0.702
1 hour - 1 day	0.35	0.241	0.56	0.088	0.62	0.72	0.701	0.57	0.367
1 day - 14 days	0.00017	0.00016	0.00027	<0.0001	0.00047	0.031	0.0379	0.0091	0.0022

Table A-7: P-value of the t statistic representing the significant differences for a treatment before any tephra application and after multiple days following tephra spraying, for the late stem extension stage. The cases in blue are the treatments showing a significative difference x time after tephra spraying compared to before any tephra spraying.

	Pr(>|t|)								
Gain size (µm)	<63 (LS)		0-3,000 (LS)		125-250 (LS)		125-250 (EYJA)		Control plot
Mass load (g m^{-2})	200	500	200	500	200	500	200	500	
before - 1 hour	0.53	0.44	0.62	<0.0001	0.52	0.52	0.37	0.61	0.32
1 hour - 1 day	0.99	0.87	0.86	0.14	0.78	0.95	0.97	0.82	0.60

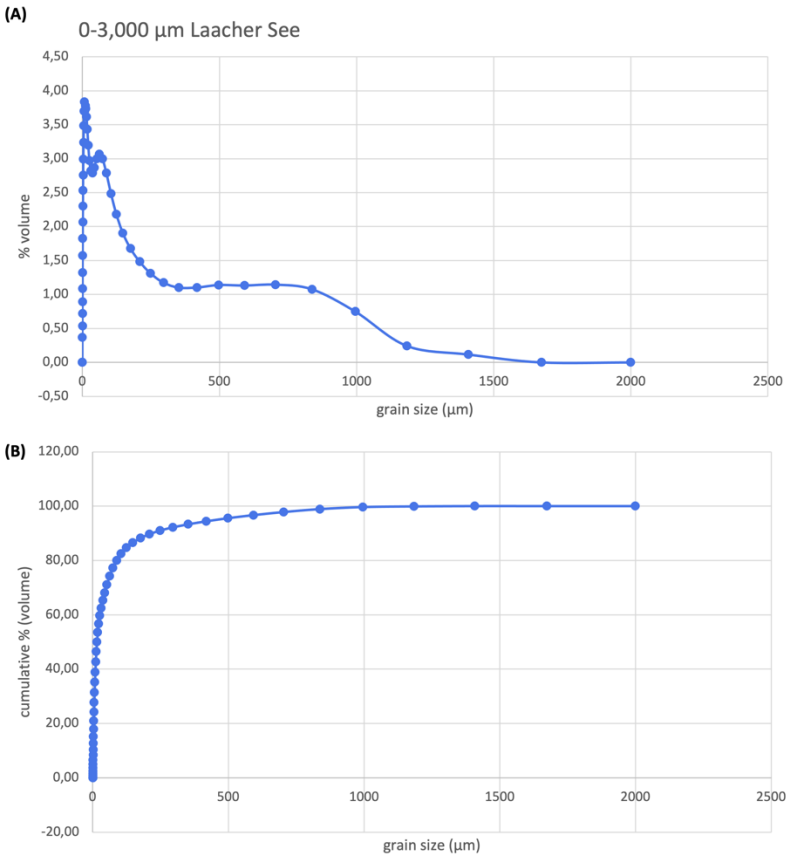

Figure A-6: Distribution of the grain size characteristics of the grain size classes 0-3,000 for Laacher See tephra (A), and cumulative distribution (B).

Characterisation of the radiative response of crops covered with tephra

by Ombeline de Potter d'Indoye
Sébastien van Wassenhove

Tephra emissions associated with volcanic eruptions impact human activities, and notably the agricultural sector. To assess the risk of tephra to crops, data on crop vulnerability are needed. However, these are difficult to acquire in the field and as a result they remain limited. Information on crop vulnerability may be retrieved through remote sensing, which provides regular, cost effective and rapid data across time and space data. The collection of the normalized difference vegetation index (NDVI) is a first step into the characterization of crop vulnerability to tephra.

In this thesis, the spectral properties of tephra were first assessed. These are dictated by the silica content, the grain size, and the chemical composition of the tephra. Finer grain size of tephra with low contents of Fe and Ti usually led to higher reflectance, whereas the presence of water absorption bands typically produced low reflectance values.

Secondly, we conducted an experiment where tephra was applied to wheat plants and the reflectance of the canopy was measured using a multispectral camera attached to a drone. Tephra spraying on the foliage led to a temporary decrease in NDVI when specific tephra deposits were applied. The reduction of NDVI was always more important for finer tephra, with the greater mass load (500 g m^{-2} compared to 200 g m^{-2}). The effect of tephra on canopy reflectance was also influenced by the phenological stage of the wheat, with a greater NDVI decrease for the early stem extension stage due to the more horizontal orientation of leaves. However, over time the NDVI of the wheat plants re-increased as soon as the tephra deposit was eroded from the leaves. Also, the signal of the leaves which had received tephra at early phenological stage was overshadowed by the appearance of new leaves.

The NDVI is a good tool to evaluate the spectral response of wheat plants covered with tephra. Future studies would be needed to further explore the relationship between vegetation index, yield loss and crop vulnerability.

UNIVERSITÉ CATHOLIQUE DE LOUVAIN
Faculty of Bioscience Engineering
Croix du Sud, 2 bte L7.05.01, 1348 Louvain-la-Neuve, Belgique | www.uclouvain.be/agro